DEVELOPMENT OF NOVEL THERAPEUTIC AND DIAGNOSTIC APPROACHES UTILIZING TOOLS FROM THE PHYSICAL SCIENCES

by

ARUNI PEIRIS MALALASEKERA

B.Sc. (Hons), University of Colombo, Sri Lanka 2009

AN ABSTRACT OF A DISSERTATION

Submitted in partial fulfillment of the requirements for the degree

DOCTOR OF PHILOSOPHY

Department of Chemistry
College of Arts and Sciences

KANSAS STATE UNIVERSITY
Manhattan, Kansas

2016

Abstract

Numerous Proteases are implicated in cancer initiation, survival, and progression. Therefore, it is important to diagnose the levels of protease expression by tumors and surrounding tissues, which are reflected in blood and tissue samples. Nanoplatforms for Cathepsin(CTS) B and L, matrix metalloproteinases(MMP) 1, 2, 3, 7, 9, 13 and urokinase plasminogen activator(uPA) detection have been synthesized. Nanoplatforms feature a central dopamine-coated core/shell Fe/Fe_3O_4 nanoparticle. Cyanine 5.5 is permanently tethered to the dopamine ligands via amide bonds. Tetrakis(4-carboxy-phenyl)porphyrin (TCPP) is co-tethered to Fe/Fe_3O_4/dopamine by means of protease consensus sequences. In the presence of a relevant protease sequence, it is cleaved, releasing TCPP from the nanoplatform. In contrast, Cy 5.5 will remain permanently tethered to the nanoparticle. Therefore, an extensive increase of emission intensity of the fluorescence signal from TCPP is observed. This permits the detection of the activity of proteases at femtomolar levels in biospecimens by fluorescence spectroscopy. 46 breast cancer and 20 healthy human blood serum samples were analyzed. Based on the expression pattern of analyzed enzymes, human breast cancer can be detected at stage I. By monitoring CTS B and L stage 0 detection may be achieved. This study demonstrates the feasibility of minimally invasive successful early cancer diagnosis.

Immunosuppression is one of the hallmarks of aggressive cancers. Arginase is overexpressed in cancer patients, resulting in systemic immunosuppression. Two nanoplatforms for arginase detection have been synthesized. Both feature a central dopamine-coated core/shell Fe/Fe_3O_4 nanoparticle to which cyanine 7.0 or cyanine 7.5 is tethered via amide bonds. In both nanoplatforms, cyanine 5.5 is linked to the N-terminal of the peptide sequence GRRRRRRRG. Arginine (R) reacts to ornithine (O) in the presence of arginase. According to our results

obtained from fluorescence spectroscopy, the oligopeptides GRRRRRRRG and GOOOOOOOG differ in their chain dynamics. In the presence of arginase, and dependent on arginase activity, fluorescence increase of both nanoplatforms is observed, which is an indication that proton-transfer quenching decreases when arginine gets converted to ornithine. The novel assays permit the detection of active arginase within an hour. Additionally, Förster Resonance Energy Transfer (FRET) is observed in nanoplatforms featuring cy 5.5/7.0 pairs, resulting in picomolar detection limits. This is the first example of a "post-translational" enzyme sensor, in which the tether is subjected to chemical transformations of the aminoacid side chains and not cleaved by an enzyme, resulting in the modified mobility of the tether. The nanoplatforms do not show a fluorescence increase when incubated with NO-reductase, an enzyme indicative of immunoactivation, which also uses arginase as substrate.

Copper dependent inhibitory activity of 10000 compound library has been studied against of *Staphylococcus aureus.* 53 copper- dependent hit molecules were recognized featuring extended thiourea core structure with NNSN motif. NMR titrations, UV/Vis studies have been performed for characterization of metal complexation and structure modeling. Chemoinformatic meta-analysis of the ChEMBL chemical database confirmed the NNSNs as an unrecognized staphylococcal inhibitor, in spite of other compound groups in chemical screening libraries. This will lead to the development of novel class of antibacterial agents against *Staphylococcus aureus.*

DEVELOPMENT OF NOVEL THERAPEUTIC AND DIAGNOSTIC APPROACHES UTILIZING TOOLS FROM THE PHYSICAL SCIENCES

by

ARUNI PEIRIS MALALASEKERA

B.Sc. (Hons), University of Colombo, Sri Lanka 2009

A DISSERTATION

submitted in partial fulfillment of the requirements for the degree

DOCTOR OF PHILOSOPHY

Department of Chemistry
College of Arts and Sciences

KANSAS STATE UNIVERSITY
Manhattan, Kansas

2016

Approved by:

Major Professor
Stefan H. Bossmann

Abstract

Numerous Proteases are implicated in cancer initiation, survival, and progression. Therefore, it is important to diagnose the levels of protease expression by tumors and surrounding tissues, which are reflected in blood and tissue samples. Nanoplatforms for Cathepsin(CTS) B and L, matrix metalloproteinases(MMP) 1, 2, 3, 7, 9, 13 and urokinase plasminogen activator(uPA) detection have been synthesized. Nanoplatforms feature a central dopamine-coated core/shell Fe/Fe_3O_4 nanoparticle. Cyanine 5.5 is permanently tethered to the dopamine ligands via amide bonds. Tetrakis(4-carboxy-phenyl)porphyrin (TCPP) is co-tethered to Fe/Fe_3O_4/dopamine by means of protease consensus sequences. In the presence of a relevant protease sequence, it is cleaved, releasing TCPP from the nanoplatform. In contrast, Cy 5.5 will remain permanently tethered to the nanoparticle. Therefore, an extensive increase of emission intensity of the fluorescence signal from TCPP is observed. This permits the detection of the activity of proteases at femtomolar levels in biospecimens by fluorescence spectroscopy. 46 breast cancer and 20 healthy human blood serum samples were analyzed. Based on the expression pattern of analyzed enzymes, human breast cancer can be detected at stage I. By monitoring CTS B and L stage 0 detection may be achieved. This study demonstrates the feasibility of minimally invasive successful early cancer diagnosis.

Immunosuppression is one of the hallmarks of aggressive cancers. Arginase is overexpressed in cancer patients, resulting in systemic immunosuppression. Two nanoplatforms for arginase detection have been synthesized. Both feature a central dopamine-coated core/shell Fe/Fe_3O_4 nanoparticle to which cyanine 7.0 or cyanine 7.5 is tethered via amide bonds. In both nanoplatforms, cyanine 5.5 is linked to the N-terminal of the peptide sequence GRRRRRRRG. Arginine (R) reacts to ornithine (O) in the presence of arginase. According to our results

obtained from fluorescence spectroscopy, the oligopeptides GRRRRRRRG and GOOOOOOOG differ in their chain dynamics. In the presence of arginase, and dependent on arginase activity, fluorescence increase of both nanoplatforms is observed, which is an indication that proton-transfer quenching decreases when arginine gets converted to ornithine. The novel assays permit the detection of active arginase within an hour. Additionally, Förster Resonance Energy Transfer (FRET) is observed in nanoplatforms featuring cy 5.5/7.0 pairs, resulting in picomolar detection limits. This is the first example of a "post-translational" enzyme sensor, in which the tether is subjected to chemical transformations of the aminoacid side chains and not cleaved by an enzyme, resulting in the modified mobility of the tether. The nanoplatforms do not show a fluorescence increase when incubated with NO-reductase, an enzyme indicative of immunoactivation, which also uses arginase as substrate.

Copper dependent inhibitory activity of 10000 compound library has been studied against of *Staphylococcus aureus.* 53 copper- dependent hit molecules were recognized featuring extended thiourea core structure with NNSN motif. NMR titrations, UV/Vis studies have been performed for characterization of metal complexation and structure modeling. Chemoinformatic meta-analysis of the ChEMBL chemical database confirmed the NNSNs as an unrecognized staphylococcal inhibitor, in spite of other compound groups in chemical screening libraries. This will lead to the development of novel class of antibacterial agents against *Staphylococcus aureus.*

Table of Contents

List of Figures

.

List of Tables

List of Abbreviations

MMP	Matrix Metalloproteinase
CTS	Cathepsins
TCPP	Tetrakis-CarboxyPhenyl Porphyrin
LOD	Limits Of Detection
RNA	RiboNucleic Acid
FRET	Förster Resonane Energy Transfer
SET	Surface Energy Transfer
uPA	Urokinase Plasminogen Activator
TEM	Transmission Electron Microscopy
HRTEM	High-Resolution Transmission Electron Microscopy
HER2	Human Epidermal growth factor Receptor 2
SNCC	Southeastern Nebraska Cancer Center
FS	Fluorescence Signal
CG	Control Group
TIMPs	Tissue Inhibitors of MetalloProteinases
ODE	1-Octadecene
HADxHCl	HexaDecylAmmonium chloride
DCM	Dichloromethane
DMF	N,N-DiMethylFormamide
HBTU	O-Benzotriazole-N,N,N',N'tetramethyl-uronium-hexafluoro-phosphate
TFA	TriFluoro Acetic
TIPS	TriIsoPropylSilyl

EDC	N-(3-Dimethylaminopropyl)-N′-ethylcarbodiimide hydrochloride
PBS	Phosphate Buffered Saline
DMAP	4-DiMethylAminoPyridine
MRSA	Methicillin-Resistant *Staphylococcus aureus* strains
HTS	High Throughput Screening
MH	Mueller Hinton
OD	Optical Density
SAR	Structure Activity Relationship
MIC	Minimal Inhibitory Concentration
NMR	Nuclear Magnetic Resonance
SA3	*S. aureus* strain
Ro5	Rule of Five
Tpsa	Topological Polar Surface Area
Cu Dep	Copper-Dependent hits
Cu Ind	Copper-Independent hits
Inv	Inverse hits
APTs	Adamantyl-bearing Pyrazolyl-Thioureas
MICs	Minimum Inhibitory Concentrations
CHARMM	Chemistry at Harvard Macromolecular Mechanics

Acknowledgements

I would first like to express my sincere gratitude to my major research advisor and mentor, Dr. Stefan H. Bossmann, for his incredible support, guidance, and encouragement throughout my PhD. I am very grateful to him for his contributions of time to answer numerous questions, sharing his immense knowledge, experience, patience and suggestions with positive deposition. Your advice on research, on my carrier as well as on life have been priceless in every hard time. I could not have imagined having a better advisor and mentor for my Ph.D study.

Besides my advisor, I would also like to thank my committee members, Dr. Duy Hua, Dr. Paul Smith, Dr. Deryl Troyer and outside chairperson Dr. Michael Veeman their valuable time to serve as my committee members and for their insightful comments and suggestions.

I must thank Mrs. Katharine Bossmann for her great support, kindness given to me and strengthening and being next to me in every good and bad times.

Also a special that goes to both present and past Bossmann group members for their help and support, especially to Dr. Hongwang Wang and Dr. Sebastian Wendel.

I would like to acknowledge Dr. Duy Hua, Dr. Daniel Higgins, Dr. Christer Aakeroy, Dr. Emily McLaurin and Dr. Ganga Hettiarachchi for allowing me to use their resources.

I also thank Dr. Leila Maurmann, Mr. Ron Jackson and Mr. James Hodgson for their technical support and guidance.

I also extend my thank to Dr. Emily McLaurin for helping me to get TEM images, Dr. Buddhika Galkaduwa for helping me with ICP measurements, Dr. Allan Prior, Ms. Man zang, Mr. Bo Hao, for helping me with Mass spectrums.

I also would like to acknowledge my collaborators: Dr. Deryl L. Troyer, Department of Anatomy and Physiology, Kansas State University; Dr. Olaf Kutsch, Dr. Frank Wolschendorf, University

of Alabama, Birmingham; Prof. Gaohong Zhu, MD, The First Affiliated Hospital of Kunming Medical University, Department of Nuclear Medicine, Kunming, China who have contributed their valuable time and knowledge towards the success of my research.

Also I wanted to thank my friends for their friendship, kindness and support.

Lastly, but certainly not least, I would like to thank very much my wonderful family. It is hard to express my sincere gratitude in words for my ever loving parents and brother for their unconditional love, support and encouragement in every time in my life. I am forever indebted to you for giving me life, your love and for molding me the person who I am today. I am so grateful to my ever loving husband and my best friend Kasun for his constant love, patience, sacrifices and faithful support throughout last seven years. He has given me the confidence, made me much stronger and motivated and being by my side every good and bad time. I have been extremely fortunate to have you in my life for this journey. Finally I would like to thank our little bundle of joy, Savin who brought us all the happiness in the world and completing our life. It is so precious to have you.

Dedication

Dedicated to Amma, Thaththa, Malli, my husband Kasun and our newborn son Savin

Chapter 1 - Introduction

My research during my thesis from April 2012 to December 2015 in the Chemistry Department at Kansas State University under the guidance of Dr. Stefan Bossmann was concerned with applying various methods from the field of Physical Sciences to a variety of mechanistic and medicinal problems. My research has resulted in co-authorship of six publications in refereed journals, as well as co-inventorship of one patent. A seventh publication is in the process of being submitted.

Publications:

1. Wang, H.; Udukala, D. N.; Samarakoon, T. N.; Basel, M. T.; Kalita, M.; Abayaweera, G.; Manawadu, H.; **Malalasekera, A**.; Robinson, C.; Villanueva, D.; Maynez, P.; Bossmann, L.; Riedy, E.; Barriga, J.; Wang, N.; Li, P.; Higgins, D. A.; Zhu, G.; Troyer, D. L.; Bossmann, S. H., Nanoplatforms for highly sensitive fluorescence detection of cancer-related proteases. *Photochem. Photobiol. Sci.* **2014,** *13* (2), 231-240.

2. Fernando, A.; **Malalasekera, A**. P.; Yu, J.; Shrestha, T. B.; McLaurin, E. J.; Bossmann, S. H.; Aikens, C. M., Refined Insights in the Photochromic spiro-Dihydroindolizine/Betaine System. *J. Phys. Chem. A* **2015,***119* (37), 9621-9629.

3. Fernando, A.; Shrestha, T. B.; Liu, Y.; **Malalasekera, A. P.**; Yu, J.; McLaurin, E. J.; Turro, C.; Bossmann, S. H.; Aikens, C. M., Insights from Theory and Experiment on the Photochromic spiro-Dihydropyrrolo-Pyridazine/Betaine System. *J. Phys. Chem. A* **2016,***120* (6), 875-883.

5. Dalecki, A. G.; **Malalasekera, A. P**.; Schaaf, K.; Kutsch, O.; Bossmann, S. H.; Wolschendorf, F. Combinatorial phenotypic screen uncovers unrecognized family of extended

thiourea inhibitors with copper-dependent anti-staphylococcal activity. *Metallomics.* **2016**.

6. Udukala, D. N.; Wang, H.; Wendel, S. O.; **Malalasekera, A. P.**; Samarakoon, T. N.; Yapa, A. S.; Abayaweera, G.; Basel, M. T.; Maynez, P.; Ortega, R.; Toledo, Y.; Bossmann, L.; Robinson, C.; Janik, K. E.; Koper, O. B.; Li, P.; Motamedi, M.; Higgins, D. A.; Gadbury, G.; Zhu, G.; Troyer, D. L.; Bossmann, S. H., Early Breast Cancer Screening Using Iron/Iron Oxide-Based Nanoplatforms with Sub-Femtomolar Limits of Detection. *Beilstein J. Nanotechnol* **2016,** *accepted*.

7. **Malalasekera, A. P.**; Wang, H.; Samarakoon, T. N.; Udukala, D. N.; Ortega, R.; Shrestha, T. B.; Troyer, D. L.; Bossmann, S. H., Nanoplatforms for the Detection of Arginase Activities. *Nanomedicine NBM* **2016,** *in preparation*.

Patent:

Malalasekera, A.P.; Wang, H.; Wendel, S. O.; Zhu, G.; Troyer, D. L.; Bossmann S. H. Nanoplatforms for Arginase, Indoleamine 2,3-Dioxygenase and Tryptophan 2,3-Dioxygenase Detection by Posttranslational Modification. 2015(WO201521821669):20pp.

My thesis document is focused on my medicinal research, which I consider more valuable to society than my mechanistic research on photochromic compounds. I have been working on the evolution of the nanoplatforms for protease detection since I have joined the Bossmann group in 2012. In 2013, I have begun developing the group of posttranslational sensors, which were patented in 2015. I will give a rationale why the chapter is a part of the thesis at the beginning of chapters 2, 3, and 4.

Chapter 2 - Early Breast Cancer Screening Using Iron/ Iron Oxide Nanoplatforms with Sub-Femtomolar Limits of Detection

Acknowledgement

I would like to acknowledge all the collaborators, who contributed their knowledge and expertise towards the success of this project. This material described in **chapter 2** has led to the following publication:

Early Breast Cancer Screening Using Iron/Iron Oxide-Based Nanoplatforms with Sub-Femtomolar Limits of Detection

Dinusha N. Udukala[1‡], Hongwang Wang[1‡], Sebastian O. Wendel[1‡], **Aruni P. Malalasekera**[1‡], Thilani N. Samarakoon[1], Asanka S. Yapa[1], Gayani Abayaweera[1], Matthew T. Basel[2], Pamela Maynez[1], Raquel Ortega[1], Yubisela Toledo[1], Leonie Bossmann[1], Colette Robinson[1], Katharine E. Janik[1], Olga B. Koper[1], Ping Li[1], Massoud Motamedi[3], Daniel A. Higgins[1], Gary Gadbury[4], Gaohong Zhu*[5], Deryl L. Troyer*[2], Stefan H. Bossmann*[1]

[1]Kansas State University, Department of Chemistry, 213 CBC Building, Manhattan, KS, USA

[2]Kansas State University, Department of Anatomy & Physiology, 228 Coles Hall, Manhattan, KS, USA

[3]The University of Texas Medical Branch, 301 University Boulevard, Galveston, TX , USA

[4]Kansas State University, Department of Statistics, 101 Dickens Hall, Manhattan, KS, USA

[5]The First Affiliated Hospital of Kunming Medical University, Department of Nuclear Medicine, 295 Xichang Road, Kunming, Yunnan, PR China

‡**These authors have contributed equally**

My research was concerned with determining the influence of the biological matrix (serum) on the performance of the nanoplatforms, as well as for the cross-sensitivity of all utilized nanoplatforms with respect to each other. Furthermore, in collaboration with Dr. Hongwang Wang and Ms. Asanka S. Yapa, I have improved the synthetic procedures of all nanoplatforms utilized here.

2.1. Abstract

Proteases, including Matrix Metalloproteinases (MMPs), Tissue Serine Proteases, and Cathepsins (CTS) exhibit numerous functions in tumor biology. Solid tumors are characterized by changes in protease expression levels by tumor and surrounding tissue. Therefore, monitoring protease levels in tissue samples and liquid biopsies is a vital strategy for early cancer detection. Water-dispersible Fe/Fe_3O_4-core/shell based nanoplatforms for protease detection are capable of detecting protease activity down to sub-femtomolar limits of detection. They feature one dye (tetrakis-carboxyphenyl porphyrin (TCPP)) that is tethered to the central nanoparticle by means of a protease-cleavable consensus sequence and a second dye (Cy 5.5) that is directly linked. Based on the protease activities of urokinase plasminogen activator (uPA), MMPs 1, 2, 3, 7, 9, and 13, as well as CTS B and L, human breast cancer can be detected at stage I by means of a simple serum test. By monitoring CTS B and L stage 0 detection may be achieved. This initial study, comprised of 46 breast cancer patients and 20 apparently healthy human subjects, demonstrates the feasibility of protease-activity-based liquid biopsies for early cancer diagnosis.

2.2. Introduction

We have detected stage I breast cancer in human patients with statistical significance by means of a simple serum test using highly sensitive Fe/Fe_3O_4-nanoparticle based nanoplatforms for protease detection. Numerous proteases are required for early mutations, tumor survival, progression, angiogenesis, and invasion [1-3]. Following the pioneering research of Weissleder et al. [4], molecular [5], macromolecular [6] and nanoparticle-based [7] protease sensors have been developed for *in-vivo* imaging and *in-vitro* diagnostics of proteases that rely on fluorescence and magnetic principles [8]. This technology is characterized by high versatility and specificity, because consensus sequences feature high selectivities for the proteases for which they were designed [9]. However, the limits of protease detection (LOD's) of the state-of-the-art technology are sub-picomolar (sub-ng/mg) [4-8], which is sufficient for *in-vivo* imaging of tumors [4,8], atherosclerotic plaques [10] and cardiovascular inflammation [11] in humans and *in-vivo* and *in-vitro* detection in rodent models for cancers [12,13], but not for the *in-vitro* detection of human cancers [14] in their earliest stages. Competing technologies for quantitative protease detection, such as immunosorbent assays [15], quantum dot barcode technology [16], and immunobeads [17] have similar LOD's. Recently Sardar, Korc et al. have reported the sensing of short noncoding RNA following a nanoplasmonic approach, which is of similar sensitivity and range than the approach reported here [18].

We have developed nanoplatforms for protease detection [19, 20] that are capable of detecting protease activities over a wide activity range down to sub-femtomolar LOD's. These nanoplatforms consist of dopamine-covered, water-dispersable iron/iron oxide core/shell nanoparticles, to which one fluorescent dye (TCPP, tetrakis-carboxyphenyl porphyrin) is tethered via a consensus sequence. A second dye (Cyanine 5.5) is permanently linked to the dopamine

coating (Figure 2.1). This design enables both, plasmon-resonance quenching (SET) [20, 21] and Förster Resonane Energy Transfer (FRET) quenching [20, 22] of the tethered TCPP units. Once TCPP is released via proteolytic cleavage of the consensus sequence, its fluorescence will increase (for most of the nanoplatforms).

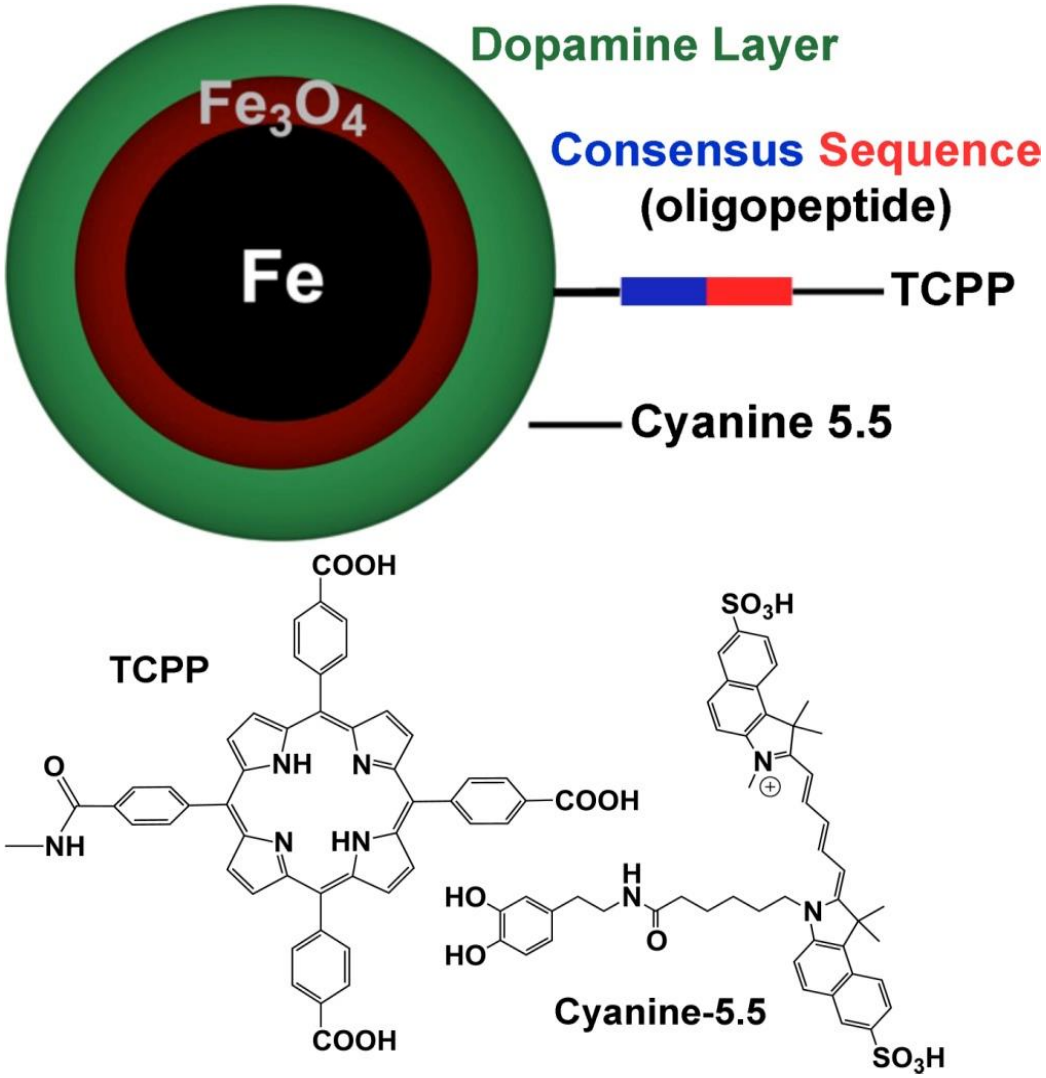

Figure 2.1: Nanosensors for *in-vitro* protease detection. For each protease, a highly selective oligopeptide is used to tether Tetrakis-carboxy-phenyl-porphyrin (TCPP) to the nanoparticle. Cyanine 5.5 is linked permanently to the Fe/Fe_3O_4 nanoparticles. Figure 2.1 is reproduced from reference 23 with permission.

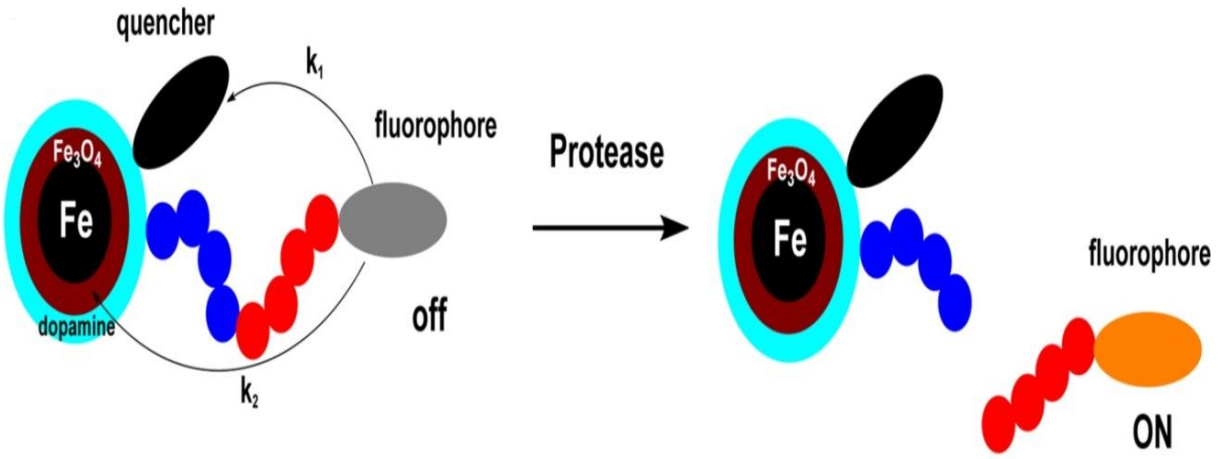

Figure 2.2: Mechanistic scheme of the "light switch effect" upon proteolytic cleavage: the fluorophore is switched on due to the increase in distance between the Fe/Fe_3O_4 core/shell nanoparticle, leading to decreased Förster Energy Transfer (FRET)[21, 24], k_1, and dipole-surface energy transfer (SET)[20,22], k_2. Further explanations are provided in the text.

The nanoplatforms for cancer detection are based on proteolytic cleavage of TCPP from the Fe/Fe_3O_4-core (Figure 2.2). Increasing the distance between the TCPP fluorophore and the nanoparticle decreases plasmon-resonance quenching (dipole-surface energy transfer (SET)[20,21]) from TCPP to Fe/Fe_3O_4 and Förster Energy Transfer (FRET[20,22]) from TCPP to cyanine 5.5. The latter is permanently tethered to the inorganic nanoparticle. For all of the employed consensus sequences, with the exceptions of GAGSGR-SAG for uPA and GAGVPLS-LYSGAG for MMP 9, an increase in TCPP fluorescence is observed upon enzymatic cleavage. This "light switch effect" [20] enables highly sensitive detection of protease activity by quantitative fluorescence measurements. In an earlier paper, we have discussed in detail why the nanoplatforms for uPA and MMP 9 detection defy the general paradigm: shorter consensus sequences and sequences permitting higher dynamics of the attached TCPP lead to fluorescence enhancement of the attached fluorophore due to enhanced plasmonic light scattering [24] of the

Fe(0) core of the central core/shell nanoparticle. For these specific consensus sequences, this effect exceeds the quenching effects (SET and FRET). Therefore, these two nanoplatforms show decreases of TCPP fluorescence upon cleavage. However, this decrease can still be utilized to measure the activities of uPA and MMP 9 in serum.

In the US, breast cancer is staged according to the TNM classification system, which is based on the extent of the spread of cancer within the body [25]. The overall 5-year survival rates for breast cancer are virtually 100% at stages 0 and I, 93% at stage II, 72% at stage III and 22% at stage IV [26]. 61% of all breast cancers in the US are diagnosed at combined stages 0 and I, 32% at stage II and 7% at combined stages III and IV [27]. Since the majority of breast cancer mortalities occurs from cases that are detected at stages II and above, detecting breast cancer by means of a routine blood test at stage I or earlier would have the potential of significantly reducing breast cancer mortality (521,900 globally in 2012)[28].

Bhatia et al. proposed nanoscale agents for *in-vivo* use that are comprised of reporter molecules bound via consensus sequences to iron oxide nanoworms. The reporter molecules are released in rodent models once the nanoworms have reached the cancer site and then excreted in urine. The quantitative detection of the reporter molecules' concentrations has been achieved by paper chromatography [29]. Although this was a major step forward in developing point-of-care diagnostics, it is still more than minimally invasive, because the nanoworms have to be given intravenously. An ideal "liquid biopsy" [30] will require only the drawing of a simple blood sample to detect cancer, without introducing a reagent to the patient's body first. In this report, we would like to discuss this approach.

In 2014, we published the synthesis and calibration of Fe/Fe_3O_4-based nanoplatforms for accurate and highly sensitive detection of 12 proteases (Figure 2.1) [20]. The calibration and validation experiments were performed with commercially available proteases in PBS (phosphate buffered saline, pH=7.4). The average Fe(0) core diameter is 13 ± 0.5nm, the Fe_3O_4 shell thickness is 2.0 ± 0.5nm (Figure 2.3). Using statistical modeling, the optimal number of TCPP units per nanoparticle was determined to be 35 ± 3, and the number of cyanine 5.5 units to be 50 ± 4 [31].

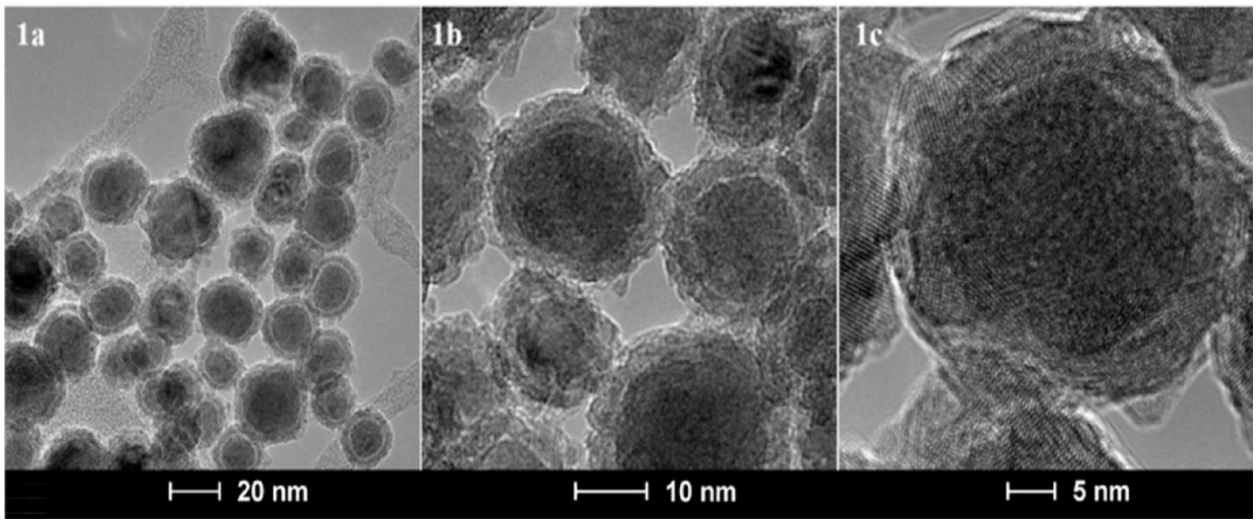

Figure 2.3: TEM (1a, 1b) and HRTEM (1c) images of Fe/Fe_3O_4-core/shell nanoparticles that are forming the inorganic core of the nanoplatforms for protease detection, with permission of the Royal Society of Chemistry [20]. HRTEM images revealed that the Fe(0) centers are mostly crystalline (BCC).

We have obtained serum samples (-80^{o}C) from 46 female breast cancer patients (4 stage 0, 9 stage I, 9 stage II, 12 stage III and 12 stage IV, as well as 20 healthy human subjects (10 males and 10 females)) from the Southeastern Nebraska Cancer Center. We have selected serum as biospecimen, because at -80^{o}C protease activity is retained for years according to our preliminary results. 20 breast cancers were luminal A [32], 12 were luminal B [33], 8 were basal-

like [32] and 6 were HER2 enriched [32]. All patients (ages 36 to 80) and healthy human subjects (ages 26 to 68) were Caucasian. No significant statistical differences in the protease expression pattern between the females and males of the control group were found.

Approximately two percent of the human genome encodes for proteases [34]. Therefore, each selection of proteases for a cancer diagnostic panel is somewhat arbitrary. For detecting early breast cancer, we have chosen the following proteases: MMPs 1,2,3,7,9,13, uPA and CTS B and L. MMP 1 has been associated with telomerase activity and promotion of tumor invasiveness and metastatic dissemination [35]. MMPs 2, 7, and 9, as well as other MMPs, release growth factors from stromal and epithelial cells at the cancer boundary, cleave off pro-angiogenic factors and start pro-angiogenic protease cascades [36, 37]. MMP 13 is involved in the epithelial-mesenchymal transition [38]. uPA and CTS B facilitate angiogenesis, ECM degradation and invasiveness. They also activate growth factors [39, 40]. MMP3 and CTS L are responsible for early mutations in carcinogenesis [2, 3].

2.3. Results and Discussion

In step 1, the influence of the serum matrix on the performance of the nanoplatforms was evaluated. For this purpose, we have used combined serum from our control group, which was inactivated using established procedures by heating to 56°C for > 30 min [41].

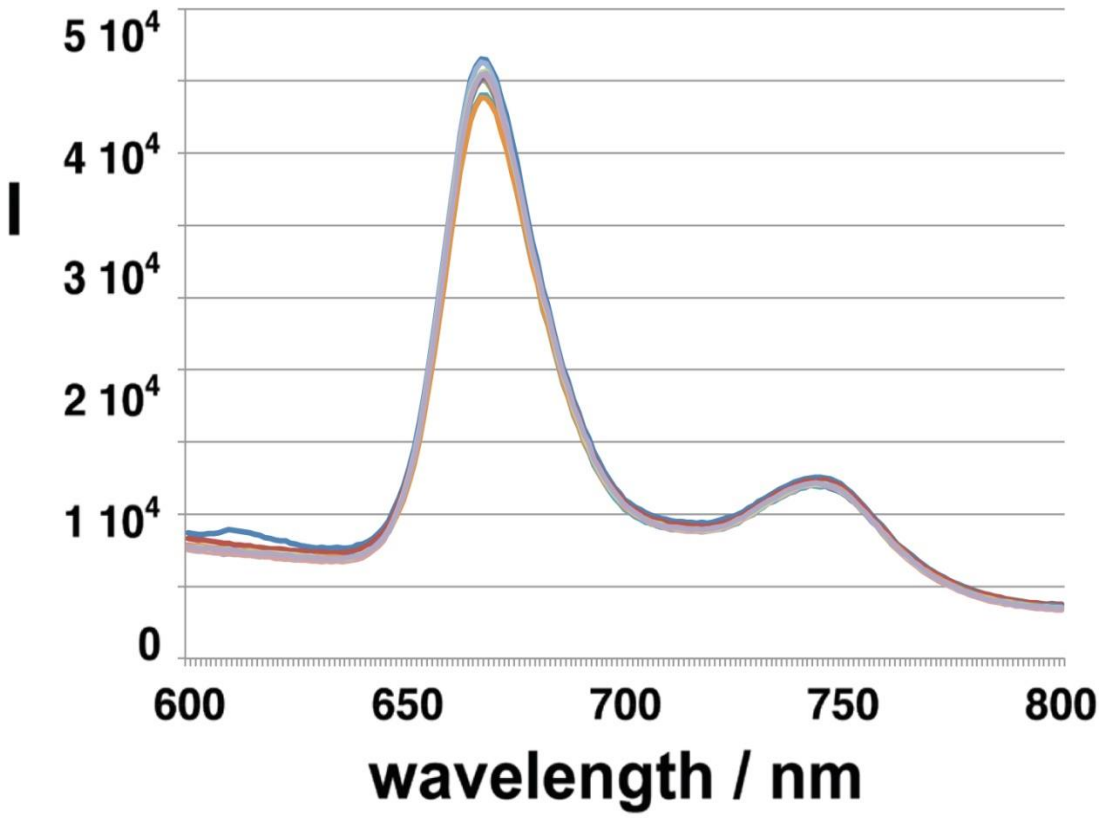

Figure 2.4: Relative Error from 10 Independently Performed Protease Measurements.

10 independent repetitions of measuring the activity of the Fe/Fe_3O_4-nanoplatform for detecting MMP13 under standard conditions at 25°C after addition of 1.0 x 10^{-13}mol l^{-1} of MMP13. The relative error was determined to be 3 percent.

In short, 3.0 ml of dextran (10 mg dextran in 1.0 ml of PBS) were mixed with 75 µl of the nanoplatform dispersion (1.0 mg in 1.0 ml of PBS) and 30 µl of the protease stock solutions at each concentration level in a total volume of 3.0 ml of PBS. 30 µl of inactivated serum was added before filling up to 3.0 ml when studying matrix effects. The solution was incubated at 25°C for 60 min. Then the fluorescence was analyzed in 4.0 ml quartz-cuvettes (Helma) using a spectrofluorometer (Fluoromax2) with dual monochromators (λ_{ex} = 421 nm, λ_{em} = 620-680 nm). The complete procedure is described in the Methods Section. From 10 independently performed repetitions, we have calculated the experimental error to ± 3% (Figure 2.4).

The results obtained in the presence and absence of inactivated serum are shown in Figures 2.5 and 2.6, as well as in Figure 2.7 (Triangles: fluorescence readings in PBS; Squares: fluorescence readings in PBS containing inactivated serum.)

Most proteases only exhibit moderate matrix effects, because of the very low concentration of serum that is required and due to the use of dextran as anti-coagulant [42]. The requirement of only a very low volume of serum for performing meaningful enzyme activity measurements is a definite advantage of the very high sensitivity of the nanoplatforms for protease detection, which originates from the concurrent utilization of SEM and FRET quenching.

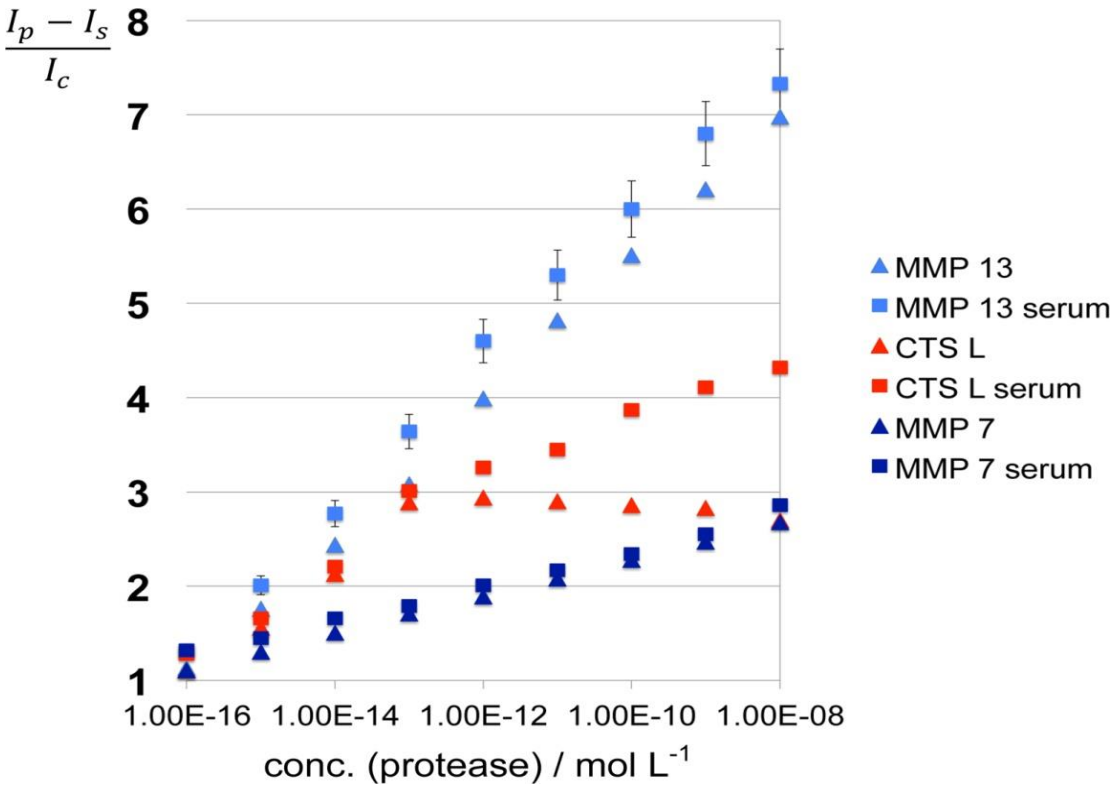

Figure 2.5: Matrix effects for MMP7, MMP13, and cathepsin L after 60 min of incubation at 25°C under standard conditions. I_p: fluorescence signal after 60 min. of incubation; I_c: fluorescence signal in the absence of protease after 60 min. incubation; I_s: fluorescence signal of serum/PBS-dextran alone. Experimental errors are indicated.

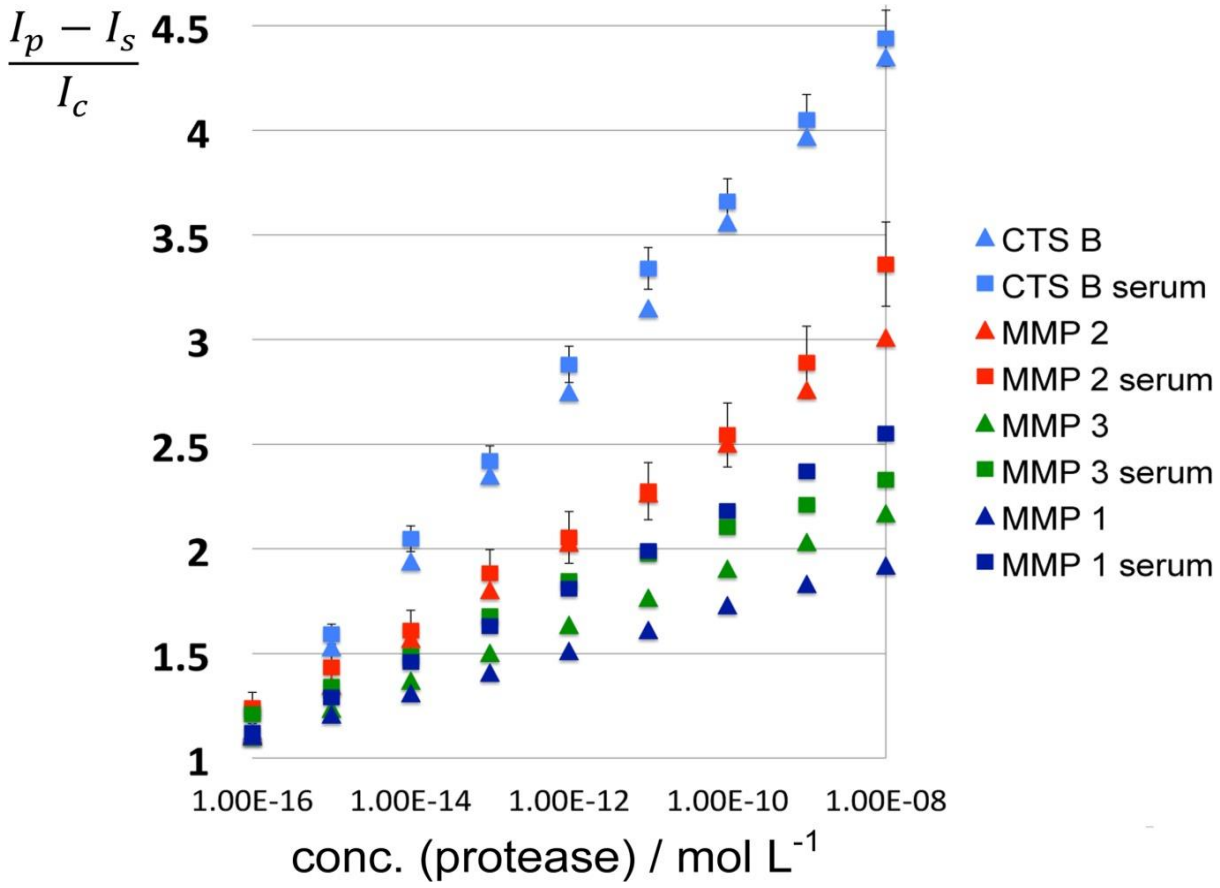

Figure 2.6: Matrix effects for MMP1, MMP 2, MMP 3, and cathepsin B after 60 min of incubation at 25ºC under standard conditions. Triangles: fluorescence readings in PBS; Squares: fluorescence readings in PBS containing inactivated serum. I_p: fluorescence signal after 60 min. of incubation; I_c: fluorescence signal in the absence of protease after 60 min. incubation; I_s: fluorescence signal of serum/PBS- dextran alone. Experimental errors are indicated.

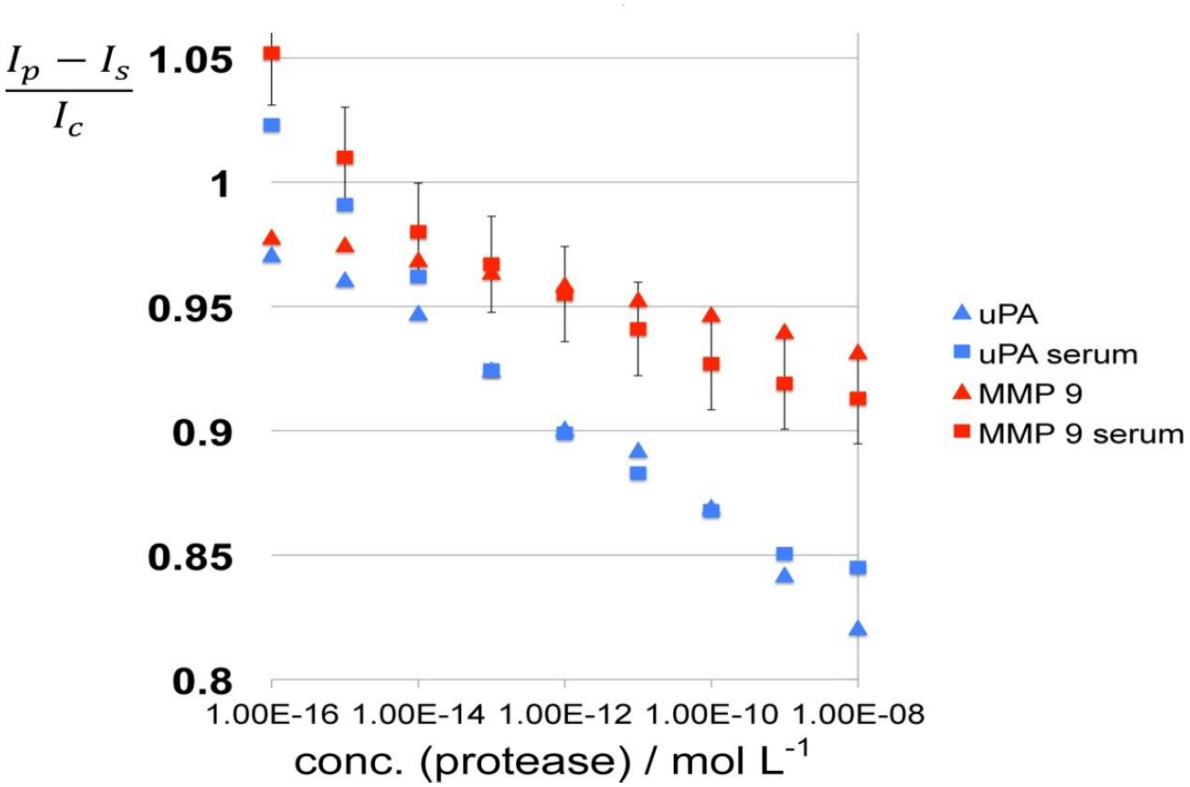

Figure 2.7: Determination of Matrix Effects on the Observed Fluorescence Intensities of the Nanoplatforms, Matrix effects for MMP9 and uPA after 60 min of incubation at 25°C under standard conditions. Triangles: fluorescence readings in PBS; Squares: fluorescence readings in PBS containing inactivated serum. I_p: fluorescence signal after 60 min. of incubation; I_c: fluorescence signal in the absence of protease after 60 min. incubation; I_s: fluorescence signal of serum/PBS-dextran alone. Experimental errors are indicated. A detailed mechanistic discussion of the reasons why uPA and MMP9 are defying the "light switch paradigm" is provided in reference 2.7.

Notable exceptions are MMPs 1 (Figure 2.6) and 7 (Figure 2.5), where significant matrix effects were detected. As noted in Table 2.1, the physical properties (isoelectric point and hydrophobicity index) of the consensus sequences plus peptide linkers designed for detecting MMP 1 and MMP 7 are within the ranges defined by all employed peptide sequences. Pieper et al. have analyzed human serum by fractionating serum proteins, followed by two-dimensional electrophoresis, and sequential anion-exchange and size-exclusion chromatography. They have resolved 3700 posttranslationally modified proteins [43]. Based on their findings, we cannot exclude that binding of the peptide sequences designed for MMP 1 and MMP 7 detection to one or several serum protein occurs, which is ultimately responsible for the observed photophysical behavior of these nanoplatforms.

Stages	Means	Standard Deviation	Average Protease Activity in Serum (mol L^{-1})
H	1.360853	0.07226045	2.4×10^{-16}
0	1.264777	0.04452960	1.4×10^{-16}
1	1.418908	0.04501105	3.3×10^{-16}
2	2.198153	0.12710588	2.6×10^{-14}
3	2.469330	0.20346940	1.1×10^{-13}
4	3.002602	0.33220471	1.8×10^{-12}

Table 2.1: Means, Standard Deviations, and Average Protease Activities in Serum for Cathepsin B (CTS B).

In Figure 2.7 the results for uPA and MMP9, two proteases that defy the "light switch paradigm" are shown. An explanation for this behavior is briefly discussed in the introduction section and more thoroughly in reference 20.

2.3.1. Cross-Sensitivities of the Nanoplatforms

In order to determine the cross-sensitivities of the nanoplatforms, the following control experiments were conducted: The nanoplatforms for MMP1,2,3,7,9,13, uPA, and CTS B,L were (separately) incubated with 1.0 x 10^{-10} mol l^{-1} of MMP1 under standard conditions (see Methods). After 60 min. of incubation at 25^{o}C, the fluorescence spectra of all nanoplatforms were recorded. The next set of experiments consisted of incubating the nanoplatforms for MMP1,2,3,7,9,13, uPA, and CTS B,L with 1.0 x 10^{-10} mol l^{-1} of MMP2 under standard conditions. This is followed by MMP3, 7, 9, 19, uPA and CTS B, and L. In Figure 2.8, the normalized results for this set of experiments are summarized. The normalization procedure consists of dividing each set of integrated fluorescence data for each enzyme by the fluorescence recording for the correct match in the entire set of nine nanoplatforms.

Set 1: integrated fluorescence recordings for all nine nanoplatforms incubated with MMP 1 (1.0 x 10^{-10} mol l^{-1}), divided by the integrated fluorescence signal obtained with the nanoplatform for MMP 1 in the presence of MMP 1;

Set 2: integrated fluorescence recordings for all nine nanoplatforms incubated with MMP 2 (1.0 x 10^{-10} mol l^{-1}), divided by the integrated fluorescence signal obtained with the nanoplatform for MMP 2 in the presence of MMP 2;

Sets 3 to 8 have been recorded accordingly for MMP 3, 7, 9, 13, uPA and CTS B.

Set 9: integrated fluorescence recordings for all nine nanoplatforms incubated with CTS L (1.0 x 10^{-10} mol l^{-1}), divided by the integrated fluorescence signal obtained with the nanoplatform for CTS L in the presence of CTS L.

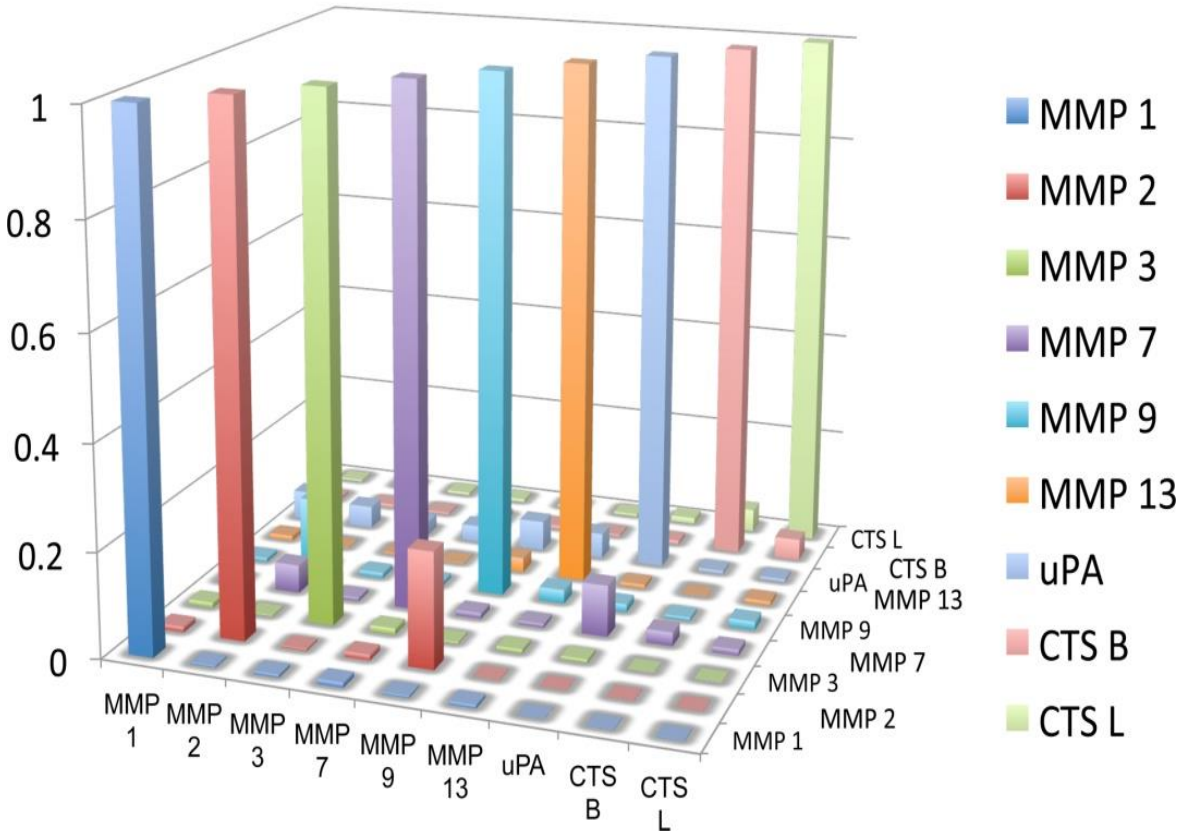

Figure 2.8: Cross-sensitivities of the nanoplatforms used in this study.

2.3.2. Diagnosis of Early Breast Cancer

The activities of the nine selected proteases in the serum of 46 breast cancer patients and 20 healthy human subjects were measured following the same procedure as for determining the matrix influence, with the exception that active serum was used, and the results statistically analyzed. A series of boxplots and bar graphs (Figure 2.9 and Figures 2.10 - 2.18) show the data range that correlates to each cancer stage, as well as the protease expression range of healthy patients [44].

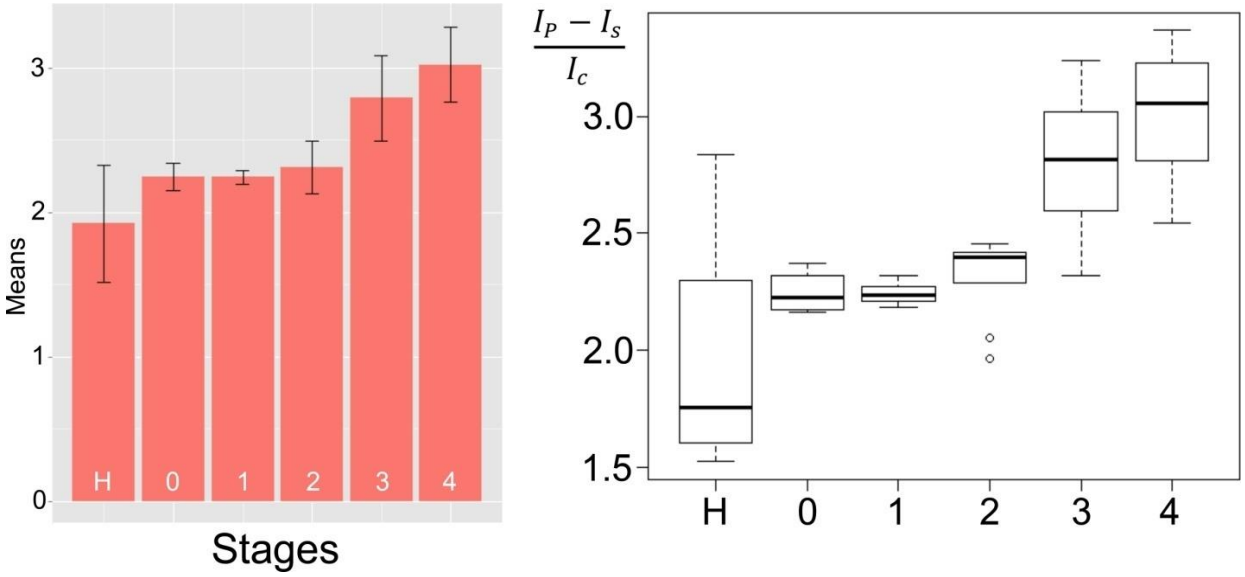

Figure 2.9: Bar-graph (left, showing means and standard deviations) and boxplot (right, indicating the observed data range) for cathepsin L. The group sizes are H (apparently healthy control group, n=20), 0: breast cancer stage 0 (+

n=4), 1: breast cancer stage 1 (n=9), 2: breast cancer stage 2 (n=9), 3: breast cancer stage 3 (n=12); 4: breast cancer stage 4 (n=12). All biospecimens were obtained from the South Eastern Nebraska Cancer Center (SNCC). Breast cancer has been staged according to the TNM staging system [25].

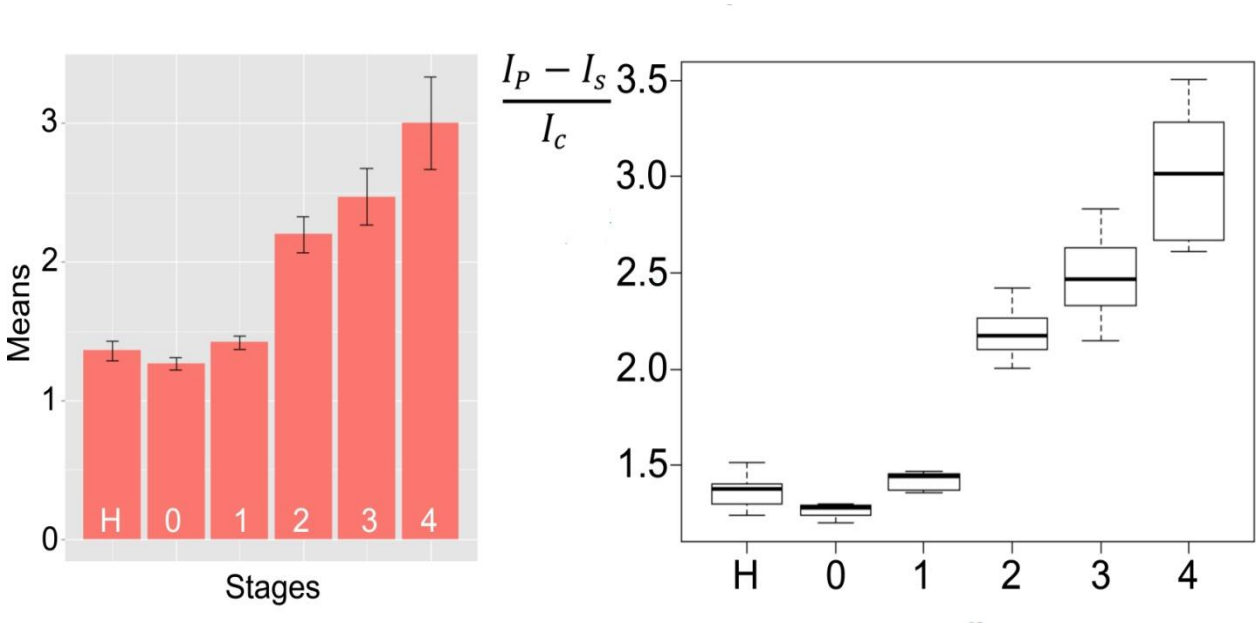

Figure 2.10: Boxplot and Bar-Graph for Cathepsin B

Bar-graph (left, showing means and standard deviations) and boxplot (right, indicating the observed data range) for cathepsin B. The group sizes are H (apparently healthy control group, n=20), 0: breast cancer stage 0 (n=4), 1: breast cancer stage 1 (n=9), 2: breast cancer stage 2 (n=9), 3: breast cancer stage 3 (n=12); 4: breast cancer stage 4 (n=12). All biospecimens were obtained from the Southeastern Nebraska Cancer Center (SNCC). Breast cancer has been staged according to the TNM staging system.[2.7]

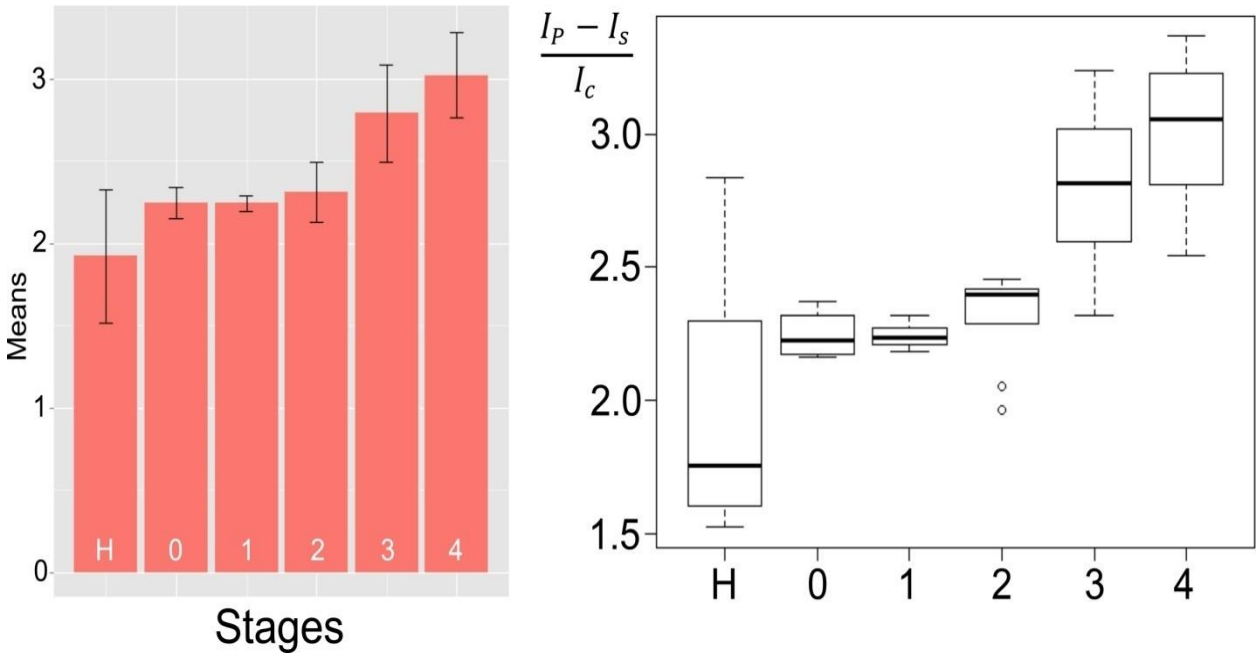

Figure 2.11: Boxplot and Bar-Graph for Cathepsin L

Bar-graph (left, showing means and standard deviations) and boxplot (right, indicating the observed data range) for cathepsin L. The group sizes are H (apparently healthy control group, n=20), 0: breast cancer stage 0 (n=4), 1: breast cancer stage 1 (n=9), 2: breast cancer stage 2 (n=9), 3: breast cancer stage 3 (n=12); 4: breast cancer stage 4 (n=12). All biospecimens were obtained from the South Eastern Nebraska Cancer Center (SNCC). Breast cancer has been staged according to the TNM staging system.[2.7]

Stages	Means	Standard Deviation	Average Protease Activity in Serum (mol L^{-1})
H	1.923536	0.40659660	1.8×10^{-15}
0	2.245194	0.09365240	8.5×10^{-15}
1	2.243285	0.04673341	8.4×10^{-15}
2	2.312233	0.18165558	1.1×10^{-14}
3	2.790727	0.29286377	5.4×10^{-14}
4	3.021944	0.25981286	1.2×10^{-13}

Table 2.2: Means, Standard Deviations, and Average Protease Activities in Serum for Cathepsin L (CTS L)

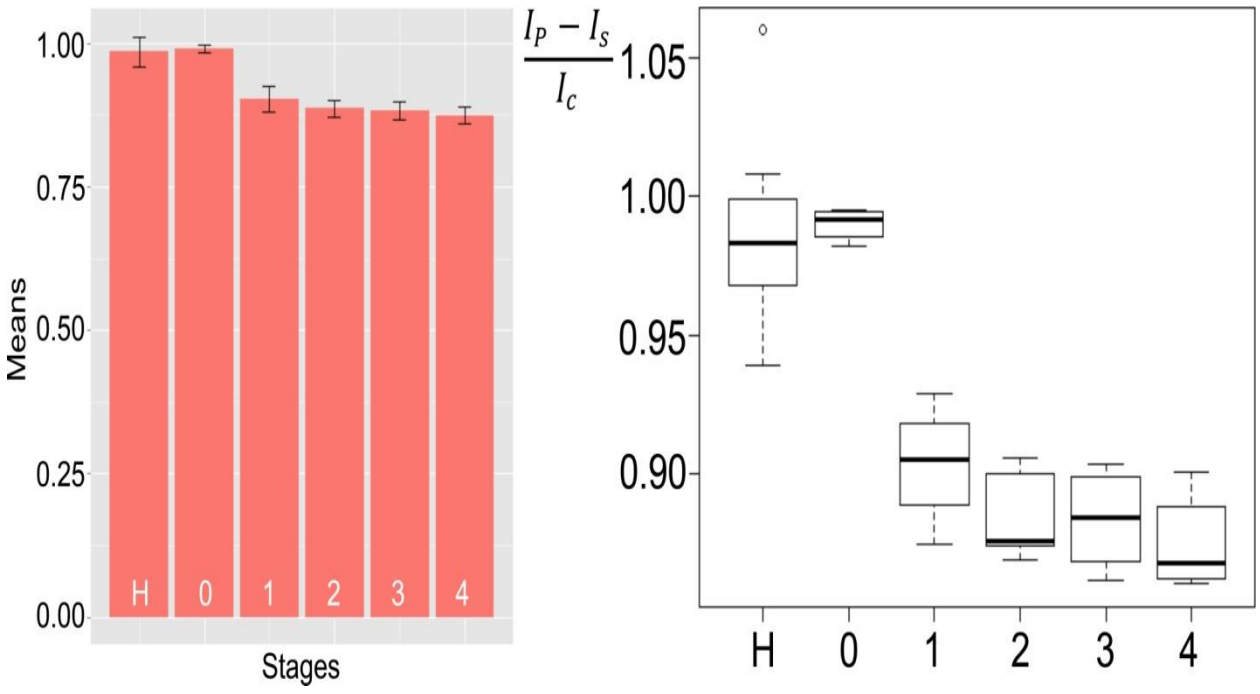

Figure 2.12: Boxplot and Bar-Graph for Urokinase Plasminogen Activator

Bar-graph (left, showing means and standard deviations) and boxplot (right, indicating the observed data range) for urokinase plasminogen activator (uPA). The group sizes are H (apparently healthy control group, n=20), 0: breast cancer stage 0 (n=4), 1: breast cancer stage 1 (n=9), 2: breast cancer stage 2 (n=9), 3: breast cancer stage 3 (n=12); 4: breast cancer stage 4 (n=12). All biospecimens were obtained from the South Eastern Nebraska Cancer Center (SNCC). Breast cancer has been staged according to the TNM staging system.[2.7]

Stages	Means	Standard Deviation	Average Protease Activity in Serum (mol L^{-1})
H	0.9848335	0.025264087	1.3×10^{-15}
0	0.9900917	0.005991484	7.8×10^{-16}
1	0.9034983	0.022280082	2.1×10^{-12}
2	0.8860111	0.015128888	1.0×10^{-11}
3	0.8832422	0.015965042	1.3×10^{-11}
4	0.8741700	0.014332318	2.0×10^{-11}

Table 2.3: Means, Standard Deviations, and Average Protease Activities in Serum for Urokinase Plasminogen Activator (uPA).

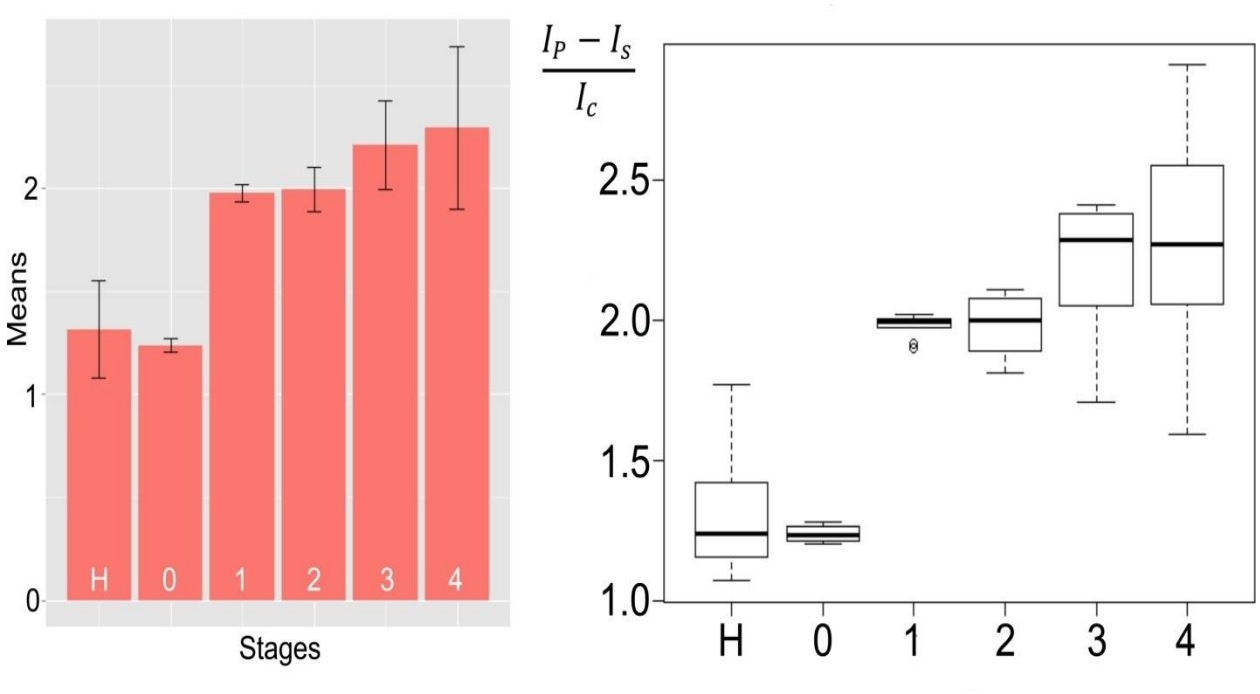

Figure 2.13: Boxplot and Bar-Graph for MMP 1

Bar-graph (left, showing means and standard deviations) and boxplot (right, indicating the observed data range) for matrix metalloproteinase 1 (MMP 1). The group sizes are H (apparently healthy control group, n=20), 0: breast cancer stage 0 (n=4), 1: breast cancer stage 1 (n=9), 2: breast cancer stage 2 (n=9), 3: breast cancer stage 3 (n=12); 4: breast cancer stage 4 (n=12). All biospecimens were obtained from the South Eastern Nebraska Cancer Center (SNCC). Breast cancer has been staged according to the TNM staging system.[2.7]

Stages	Means	Standard Deviation	Average Protease Activity in Serum (mol L^{-1})
H	1.314616	0.23507424	1.6×10^{-15}
0	1.236894	0.03339194	5.9 x 10-^{16}
1	1.978331	0.04220099	7.8×10^{-12}
2	1.995024	0.10799028	9.6×10^{-12}
3	2.210357	0.21628141	1.5×10^{-10}
4	2.292405	0.39496657	4.3×10^{-10}

Table 2.4: Means, Standard Deviations, and Average Protease Activities in Serum for Matrix Metalloproteinase 1 (MMP 1)

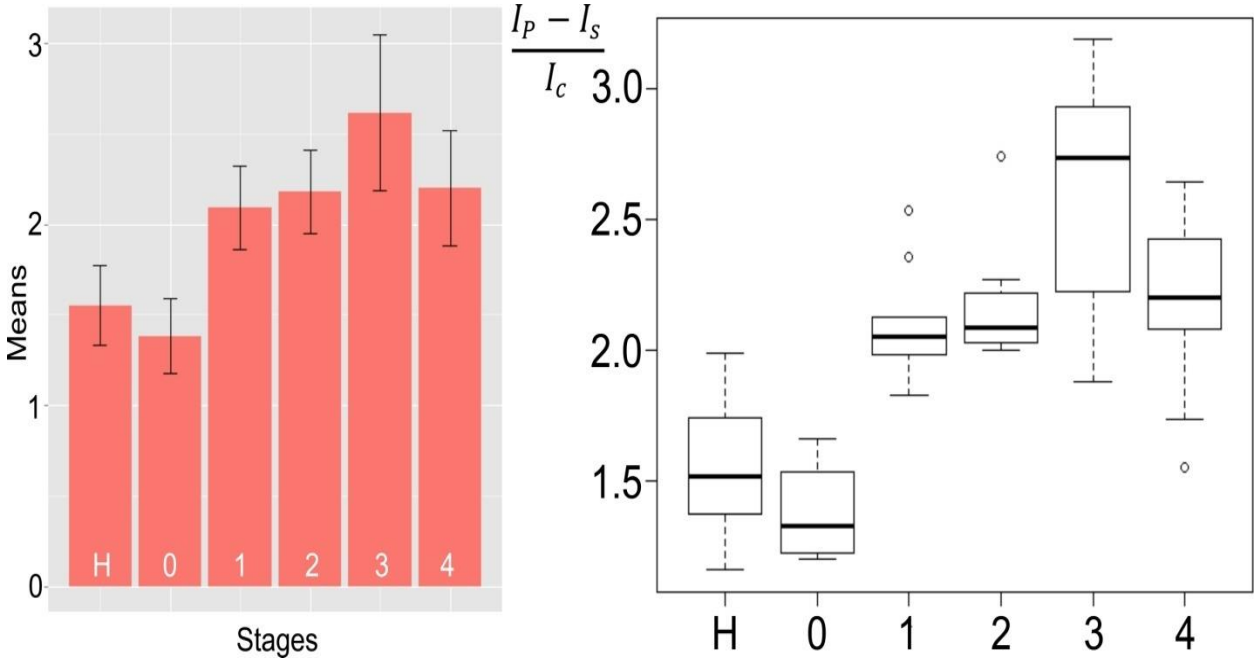

Figure 2.14: Boxplot and Bar-Graph for MMP 2

Bar-graph (left, showing means and standard deviations) and boxplot (right, indicating the observed data range) for matrix metalloproteinase 2 (MMP 2). The group sizes are H (apparently healthy control group, n=20), 0: breast cancer stage 0 (n=4), 1: breast cancer stage 1 (n=9), 2: breast cancer stage 2 (n=9), 3: breast cancer stage 3 (n=12); 4: breast cancer stage 4 (n=12). All biospecimens were obtained from the South Eastern Nebraska Cancer Center (SNCC). Breast cancer has been staged according to the TNM staging system.[2.7]

Stages	Means	Standard Deviation	Average Protease Activity in Serum (mol L^{-1})
H	1.551050	0.2210302	4.0×10^{-15}
0	1.381780	0.2078706	6.4×10^{-16}
1	2.093351	0.2287855	1.4×10^{-12}
2	2.181590	0.2301482	3.6×10^{-12}
3	2.616193	0.4300199	4.0×10^{-10}
4	2.200369	0.3192078	4.4×10^{-12}

Table 2.5: Means, Standard Deviations, and Average Protease Activities in Serum for Matrix Metalloproteinase 2 (MMP 2)

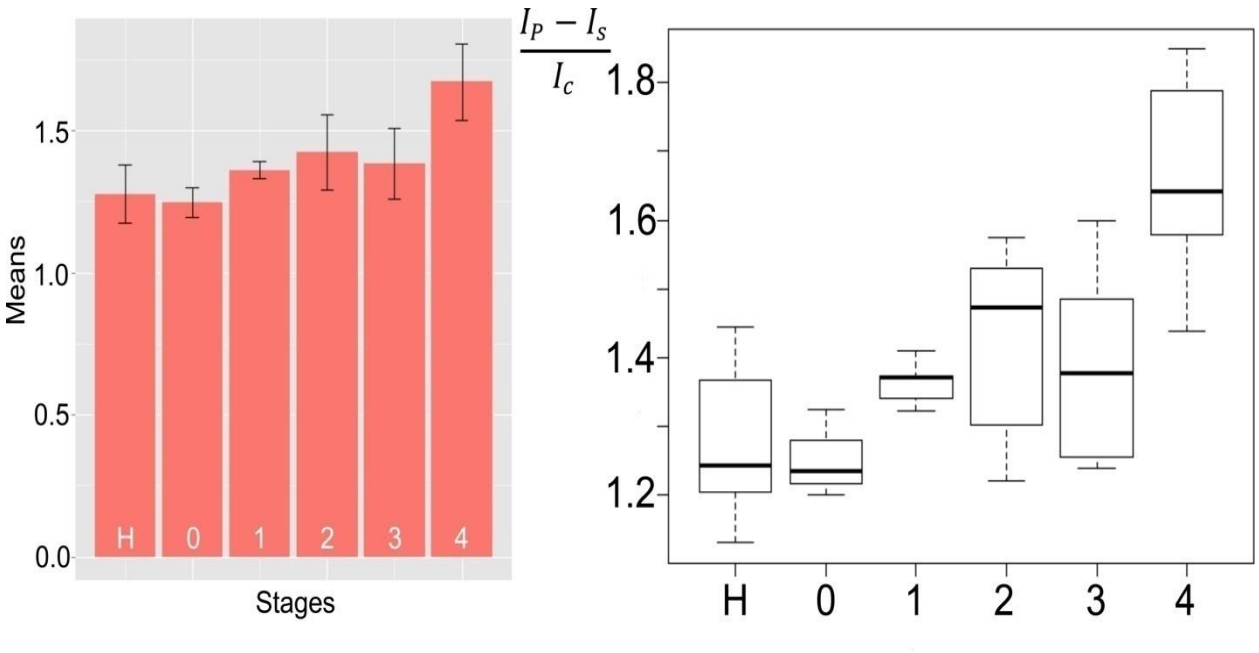

Figure 2.15: Boxplot and Bar-Graph for MMP 3

Bar-graph (left, showing means and standard deviations) and boxplot (right, indicating the observed data range) for matrix metalloproteinase 3 (MMP 3). The group sizes are H (apparently healthy control group, n=20), 0: breast cancer stage 0 (n=4), 1: breast cancer stage 1 (n=9), 2: breast cancer stage 2 (n=9), 3: breast cancer stage 3 (n=12); 4: breast cancer stage 4 (n=12). All biospecimens were obtained from the South Eastern Nebraska Cancer Center (SNCC). Breast cancer has been staged according to the TNM staging system.[2.7]

Stages	Means	Standard Deviation	Average Protease Activity in Serum (mol L^{-1})
H	1.276774	0.10293781	3.4×10^{-16}
0	1.248445	0.05253079	2.2×10^{-16}
1	1.361347	0.02882905	1.2×10^{-15}
2	1.423178	0.13355403	2.9×10^{-15}
3	1.383381	0.12401589	1.6×10^{-15}
4	1.670680	0.13369459	1.2×10^{-13}

Table 2.6: Means, Standard Deviations, and Average Protease Activities in Serum for Matrix Metalloproteinase 3 (MMP 3)

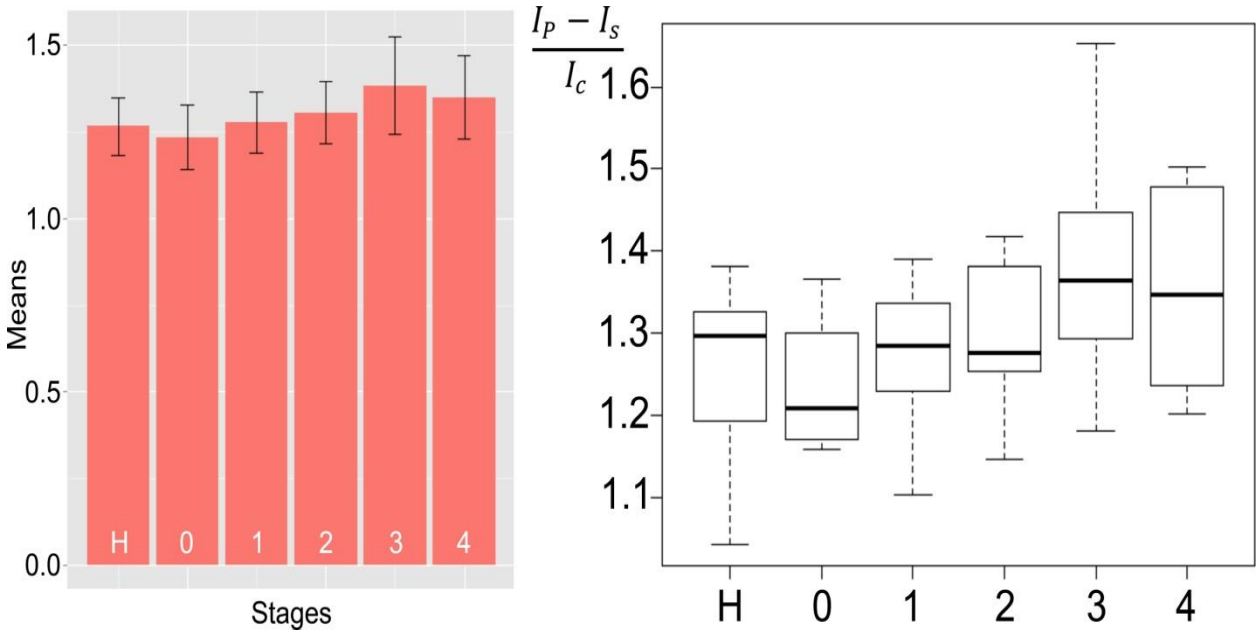

Figure 2.16: Boxplot and Bar-Graph for MMP 7

Bar-graph (left, showing means and standard deviations) and boxplot (right, indicating the observed data range) for matrix metalloproteinase 7 (MMP 7). The group sizes are H (apparently healthy control group, n=20), 0: breast cancer stage 0 (n=4), 1: breast cancer stage 1 (n=9), 2: breast cancer stage 2 (n=9), 3: breast cancer stage 3 (n=12); 4: breast cancer stage 4 (n=12). All biospecimens were obtained from the South Eastern Nebraska Cancer Center (SNCC). Breast cancer has been staged according to the TNM staging system.[2.7]

Stages	Means	Standard Deviation	Average Protease Activity in Serum (mol L^{-1})
H	1.265858	0.08413963	6.4×10^{-16}
0	1.235173	0.09279042	4.5×10^{-16}
1	1.276960	0.08834555	7.2×10^{-16}
2	1.306292	0.09032285	1.0×10^{-15}
3	1.384025	0.14060255	2.5×10^{-15}
4	1.349619	0.12004177	1.7×10^{-15}

Table 2.7: Means, Standard Deviations, and Average Protease Activities in Serum for Matrix Metalloproteinase 7 (MMP 7)

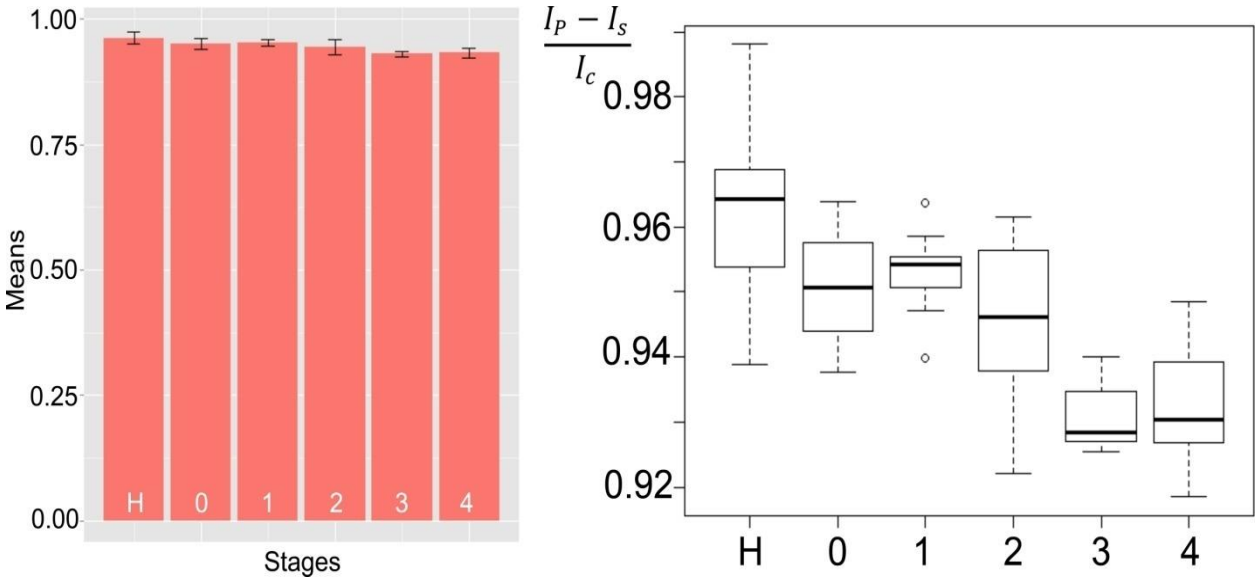

Figure 2.17: Boxplot and Bar-Graph for MMP 9

Bar-graph (left, showing means and standard deviations) and boxplot (right, indicating the observed data range) for matrix metalloproteinase 9 (MMP 9). The group sizes are H (apparently healthy control group, n=20), 0: breast cancer stage 0 (n=4), 1: breast cancer stage 1 (n=9), 2: breast cancer stage 2 (n=9), 3: breast cancer stage 3 (n=12); 4: breast cancer stage 4 (n=12). All biospecimens were obtained from the South Eastern Nebraska Cancer Center (SNCC). Breast cancer has been staged according to the TNM staging system.[2.7]

Stages	Means	Standard Deviation	Average Protease Activity in Serum (mol L^{-1})
H	0.9622952	0.011980785	8.6×10^{-13}
0	0.9507300	0.010709674	5.9×10^{-12}
1	0.9530756	0.006783337	4.0×10^{-12}
2	0.9439189	0.014798504	1.8×10^{-11}
3	0.9308592	0.005204805	1.6×10^{-10}
4	0.9327775	0.009121815	1.2×10^{-10}

Table 2.8: Means, Standard Deviations, and Average Protease Activities in Serum for Matrix Metalloproteinase 9 (MMP 9)

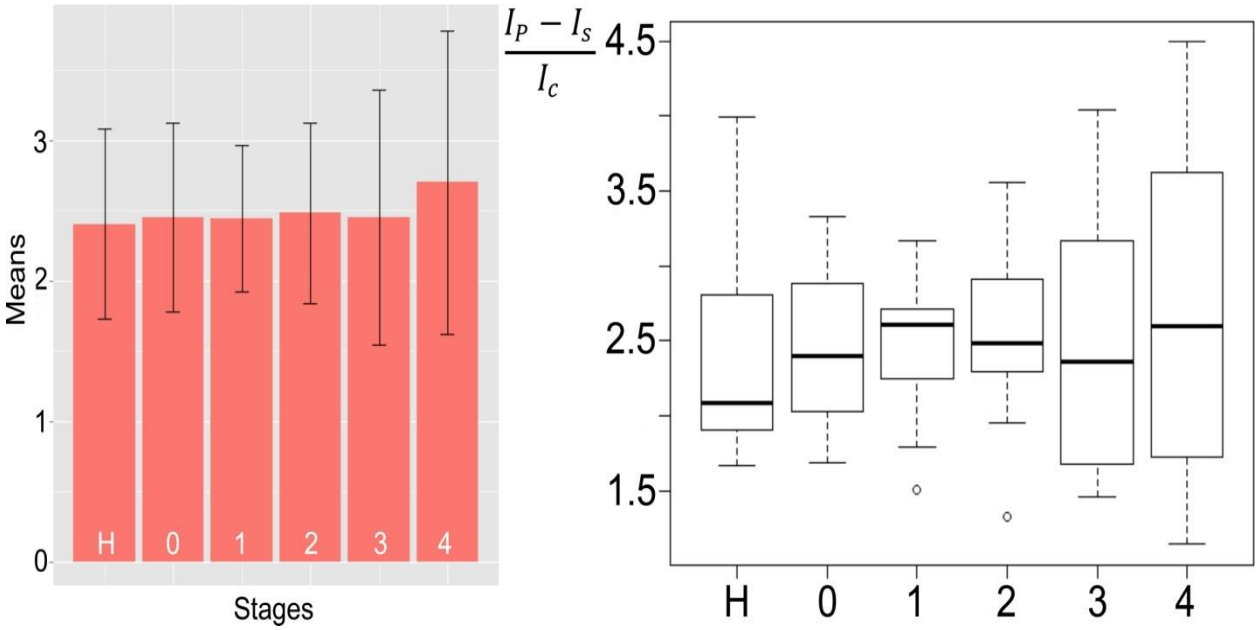

Figure 2.18: Boxplot and Bar-Graphs for MMP 13

Bar-graph (left, showing means and standard deviations) and boxplot (right, indicating the observed data range) for matrix metalloproteinase 13 (MMP 13). The group sizes are H (apparently healthy control group, n=20), 0: breast cancer stage 0 (n=4), 1: breast cancer stage 1 (n=9), 2: breast cancer stage 2 (n=9), 3: breast cancer stage 3 (n=12); 4: breast cancer stage 4 (n=12). All biospecimens were obtained from the South Eastern Nebraska Cancer Center (SNCC). Breast cancer has been staged according to the TNM staging system.[2.7]

Stages	Means	Standard Deviation	Average Protease Activity in Serum (mol L^{-1})
H	2.402871	0.6767673	3.2×10^{-15}
0	2.454853	0.6726423	3.7×10^{-15}
1	2.447914	0.5209525	3.6×10^{-15}
2	2.483194	0.6442519	4.0×10^{-15}
3	2.453076	0.9055961	3.7×10^{-15}
4	2.701158	1.0781773	7.5×10^{-15}

Table 2.9: Means, Standard Deviations, and Average Protease Activities in Serum for Matrix Metalloproteinase 13 (MMP 13)

The analyzed enzymes include Cathepsin B and L, MMP 1, 2, 3, 7, 9, 13 and uPA. Except for MMP9 and uPA, all enzymes display a positive trend with an increasing signal for higher cancer stages. The reason for this behavior is discussed in the text: in short, the nanoplatforms for uPA and MMP 9 detection show decreasing fluorescence intensities with increasing protease activity. We have chosen boxplots and bar-graphs for data analysis, in combination with Welch two sample t-tests (control group and cancer patients at a defined stage) [45], because a combination of these analysis methods provides a simple system for data analysis. The boxplots show the data range that correlates to a certain cancer stage while the bar graphs display the average signal and standard deviation (represented by the error bar) for individual cancer stages.

With respect to detecting cancer at an early stage, the data obtained for cathepsin B and L, uPA and MMP 1, 3 and 9 is superior to MMP 2, 7 and 13. Here the fluorescence signals for each cancer stage are compared with the healthy control group's fluorescence signals. Highly significant differences between cancer patients and healthy control group are achieved with cathepsins B and L, uPA, MMP1 and 9. It is noteworthy that only cathepsins B and L are significantly different from the healthy group for stage 0 breast cancer. Especially cathepsin L seems promising here since it maintains its positive trend of the signal. However, the stage 0 group is very small (n=4). Therefore, all enzymes should be revisited when more data becomes available.

Highly significant differences are achieved with CTS B, L, uPA, MMP 1 and 9. It is interesting to observe that only CTS B and L produce a signal for stage 0 breast cancer that is significantly different from the healthy group. Especially CTS L seems promising here since it maintains its positive trend of the signal. However, the stage 0 group is too small (n=4) and the control group is somewhat spread out. Stage 0 has to be revisited when more data becomes available.

In Figure 2.19, the calculated p-values [45] obtained for comparisons of the protease expression pattern in each cancer stage with those of the healthy control group are tabulated, leading to the "Significance Table". The color green denotes for measured fluorescence signals that are significantly enhanced ($p < 0.05$) in cancer patients compared to the healthy control group. The color yellow represents findings, in which the fluorescence signals detected in the serum of cancer patients were significantly smaller than in the control group. The color red was used for all cases in which significant results could not be obtained. It should be noted (again)

that uPA and MMP 9 are the “defiant proteases”. Their fluorescence signals decrease with increased protease activity.

Significance Table									
	CTS B	CTS L	uPA	MMP1	MMP2	MMP3	MMP7	MMP9	MMP13
Stage 0	0.005417	0.002439	0.2101	0.08649	0.104	0.2196	0.2863	0.05784	0.4471
Stage 1	0.007313	0.001213	0.000809	1.91E-11	1.28E-05	0.00118	0.3776	0.007169	0.4235
Stage 2	1.37E-09	0.000703	8.12E-13	1.75E-11	2.55E-06	0.00618	0.1366	0.00304	0.3818
Stage 3	9.09E-11	5.75E-08	6.63E-15	2.51E-11	5.51E-07	0.01051	0.00895	2.83E-11	0.4349
Stage 4	7.72E-10	1.22E-10	2.23E-16	4.33E-07	4.28E-06	2.25E-08	0.02407	7.14E-09	0.2006

Figure 2.19: Calculated p-values; comparison of breast cancer patients and healthy human subjects for all investigated enzymes, stages 0-4 - Green: fluorescence signal (FS) of cancer patients is significantly larger than of control group (CG); Yellow: FS is significantly smaller; Red: differences in FS and CG are not significant.

The resulting average enzyme activities in the serum of the healthy control group and breast cancer stages 0, 1, 2, 3, and 4 are summarized in Figure 2.20.

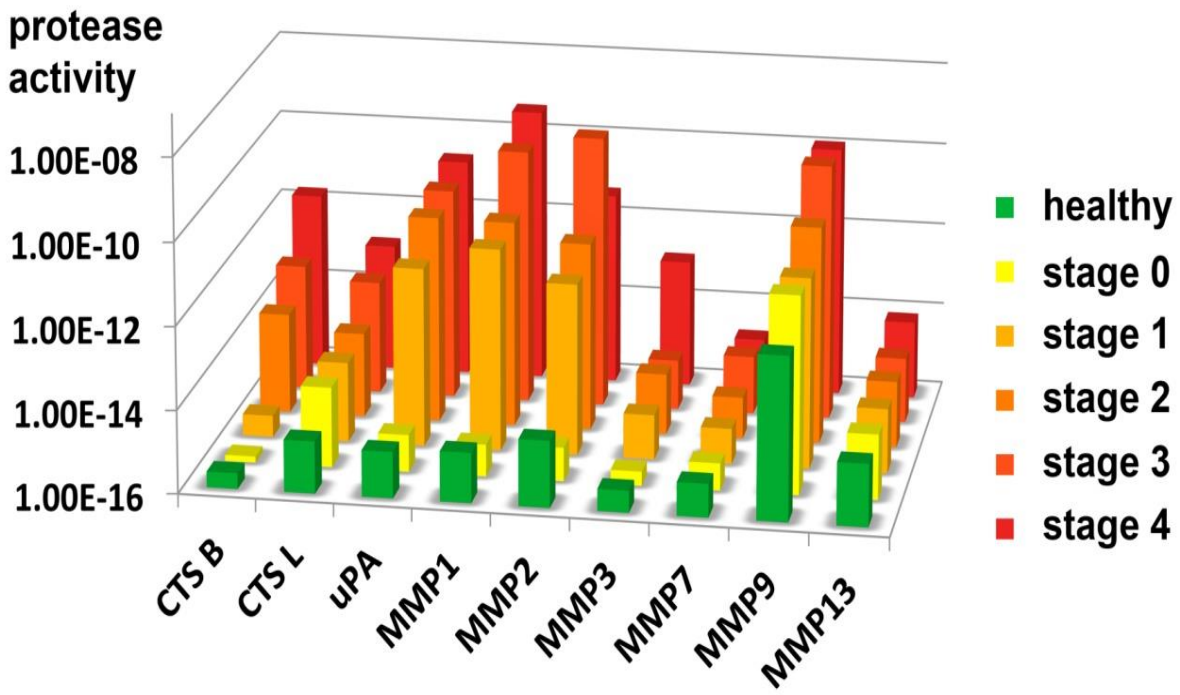

Figure 2.20: Average protease activity as a function of breast cancer stage / healthy control group for all nine proteases monitored in this study. Note that the activity is shown on a logarithmic scale ($\log_{10}$ (protease activity)). The data summarized in this figure is also reported in Tables 2.1 to 2.9.

Healthy control groups and stages are color coded. From this plot, it can be discerned why cathepsin L is the best enzyme to detect both, early breast cancer and cancer staging. MMP 1, MMP 9 and uPA show similar enzyme activity trends, but we were unable to distinguish between healthy patients and stage 0 breast cancer patients. The inability to reach this goal was due to variations of protease expression among the apparently healthy human subjects and the

small sample size (n=4) in stage 0. Cathepsin B, MMP 2 can be used to identify breast cancer patients that are in or beyond stage 2. MMP 3 could, in theory, identify late stage patients. Finally, MMP 7 and MMP 13 did not yield conclusive results. It is noteworthy that although MMP 2, 7, and 9 belong to a group of MMPs that are known to release are known to release growth factors, cleave off pro-angiogenic factors and start pro-angiogenic protease cascades[36,37], MMP 2 and MMP 9 yield conclusive results for stages one to four, whereas MMP 7 is only conclusive at higher stages. MMP 13 did not generate any significant results, although MMP 13 is involved in the epithelial-mesenchymal transition [38]. The reasons for these deviations among related matrix metalloproteinases may be found in different tissue retention and enzymatic degradation of individual proteases, as well as in the activity profiles of tissue inhibitors of metalloproteinases (TIMPs) in blood [46].

2.4. Conclusion

In conclusion, the most important result of this research is that we are able to detect breast cancer at stage I monitoring seven proteases and at stage 0 observing one protease with high statistical significance. This result is of importance, because we have achieved it with relatively small group sizes of breast cancer patients and healthy control subjects. As always when testing biomarkers, the selection process of the required biospecimens is crucial. Therefore, our next steps will consist in testing our liquid biopsy approach with significantly larger group sizes of stage 0 and I breast cancer patients.

2.5. Methods

2.5.1. Synthesis of core/ shell iron/ iron oxide - Fe/Fe3O4 nanoparticles

The synthesis of dopamine-coated nanoparticles (Figure 2.21) has been established in the Bossmann group by performing a modification of a literature procedure depicted by Lacroix et al. The published synthesis procedure Wang et al. (2014) was followed for this research[20].

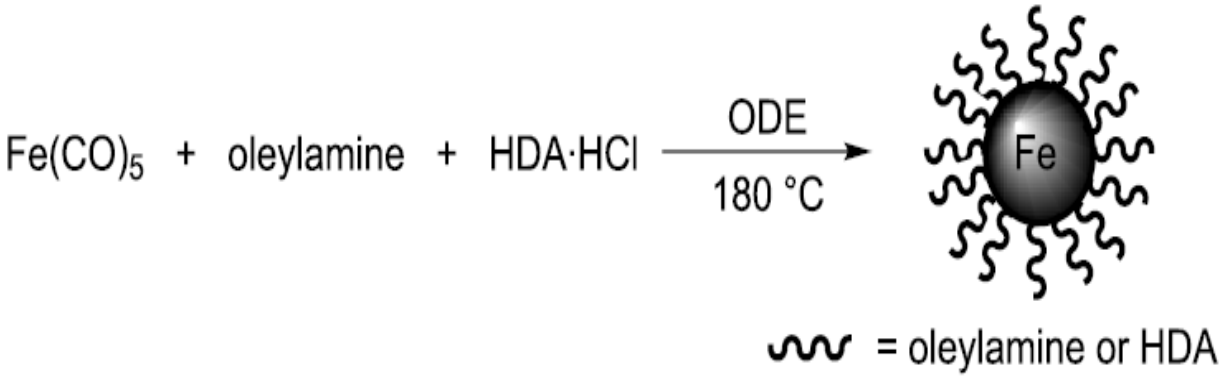

Figure 2.21: Synthesis of core/ shell iron/ iron oxide - Fe/Fe3O4 nanoparticles (Wang et al. 2012)

The synthesis procedure (from Wang et al. (2014)) is reproduced here. A 250 mL, three-necked, round-bottom flask equipped with a magnetic stir bar, one cold water cooled jacket condenser on the middle neck, one septum and one temperature probe on each of the outer necks was charged with 60 mL 1-octadecene (ODE), 0.9 mL oleylamine and 0.831 g hexadecylammonium chloride (HADxHCl). The reaction system was connected to a Schlenk line through the top of the jacket condenser. The reaction mixture was degassed at 120^{o}C for 30 min with vigorous stirring. After being refilled with argon, the reaction mixture was heated to 180o C. Three portions of 0.7 mL $Fe(CO)_5$ were injected into the reaction mixture via syringe, every 20 min. The reaction mixture was kept at 180^{o} C for another 20 min after the last injection, and then cooled to room temperature naturally. The supernatant was decanted, and the iron nanoparticles accumulated on the magnetic stir bar were washed with hexane and ethanol. The

product was dried in vacuum and stored at room temperature under argon for further use. Based on the iron content of the nanoparticles, which was determined spectrophotometrically after dissolving the nanoparticles in aqueous HCl (1.0 M) and subsequent complexation with ferrozine (sodium 4,4'-(3-(pyridin-2-yl)-1,2,4-triazine-5,6-diyl)dibenzenesulfonate)2 , the yield of the reaction is 95%.

2.5.2. Dopamine coating of the core/ shell iron/ iron oxide nanoparticles.

The Fe/Fe_3O_4-nanoparticles will be protected by using dopamine. The synthesis procedure (from Wang et al. (2014)) is reproduced here.

Dopamine Coating of the core/shell Fe/Fe3O4 Nanoparticles 0.50 g of previously synthesized Fe/Fe3O4 nanoparticles was dispersed in 100 mL chloroform via sonication. With vigorous mechanical stirring, a solution of 0.50 g dopamine-hydrochloride in 50 mL chloroform was added drop-wise to the nanoparticle suspension. The reaction mixture was further stirred at room temperature for 24 hours, and then the dopamine coated nanoparticles were collected by centrifugation. After washing with chloroform 5 times, nanoparticles were dried under vacuum. 0.47 g dopamine coated Fe/Fe3O4 nanoparticles were collected [20].

2.5.3. Synthesis of TCPP Fluorophore

The synthesis of (4-carboxyphenyl)porphyrin has been established in the Bossmann group by performing a variation of a literature procedure of Pereira et al. (2008)[51].

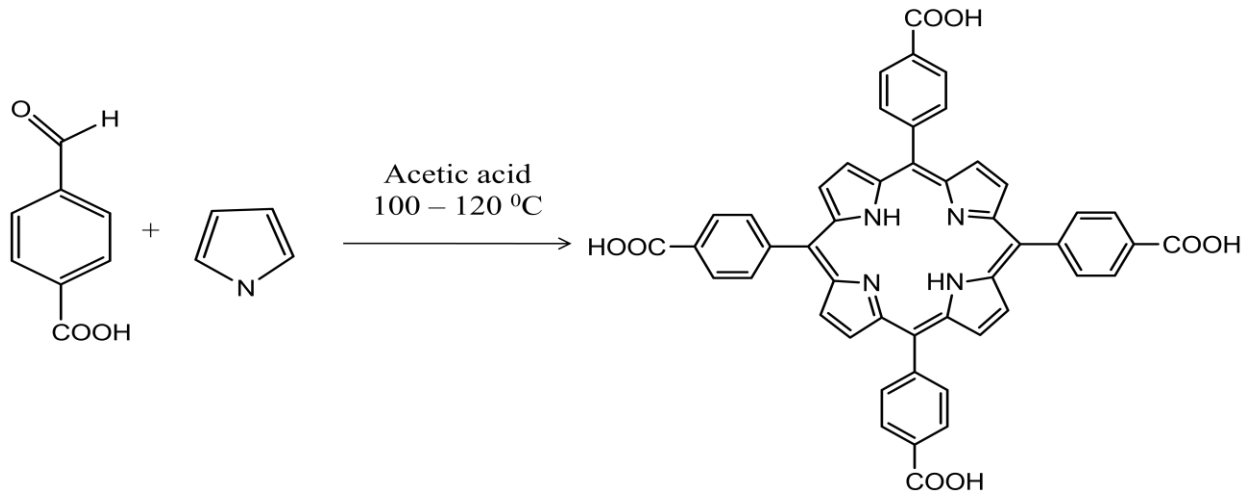

Figure 2.22: Reaction scheme for synthesis of TCPP

The published synthesis procedure (from Wang et al. (2014)) was followed for this research. 1.50 g 4-carboxybenzaldehyde was dissolved in 80 mL acetic acid. The solution was warmed to 100°C and a solution of 0.67 g pyrrole in 10 mL acetic acid was added dropwise over 20 minutes. Upon completion of addition, the solution was warmed to 120 °C slowly and was kept at 120 °C for 1 hour (Figure 2.22). The mixture was cooled to 80o C and 100 mL 95% ethanol was added and then lowered to room temperature, while stirring in 3 hours. Then the mixture was kept in at -15 °C for 24 hours. Purple solid was collected by vacuum filtration. The filter cake was washed with cold 50/50 ethanol/acetic acid (3×5mL) and dried under high vacuum (oil pump) overnight. 0.51g of pure product was obtained (25.5% yield) [20]. 1H NMR (DMSO-d6) δ: -2.94 (s, 2H); 8.35 (d, 8H); 8.39 (d, 8H); 8.86 (s, 8H); 13.31 (s, 4H) (Figure A1) 13C NMR (DMSO-d6) δ: 119.31; 127.90; 130.51; 134.44; 145.42; 167.46. MS-ESI+: m/z 791.2. Molecular weight calculated as 790.2 (Figure A2).

2.5.4. Synthesis of Cyanine 5.5

The fluorescent cyanine 5.5 dye was synthesized following three reaction schemes. Reaction procedures are variation of literature procedures described in Carreon et al. (2007)[52]. The published synthesis procedures (from Wang et al. (2014)) was followed for this research [20].

2.5.4(A) Synthesis of 4-(1,1,2-trimethyl-1H-benzo[e]indol-3-ium-3-yl)butane-1-sulfonate (Figure 2.23)

The published synthesis procedure (from Wang et al. (2014)), which is an alteration of the synthetic procedure in Carreon et al. (2007) was followed.

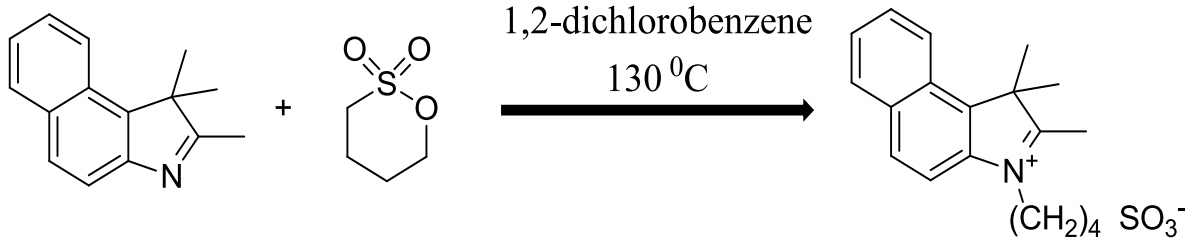

Figure 2.23: Reaction scheme for synthesis of 4-(1,1,2-trimethyl-1H-benzo[e]indol-3-ium-3-yl)butane-1-sulfonate.

A 50 mL two necked round bottom flask fitted with a magnetic stirrer and a condenser was flame dried. 1,1,2-trimethyl-1H-benzo[e]indole (1.0g, 4.78mmol) was dissolved in dry o-dichlorobenzene (10 mL). 1, 4-butanesultone (0.58mL, 5.73mmol) was added drop-wise under a continuous flow of argon. The reaction mixture was, then, allowed to heat up to 130 ^{0}C for 24h. The reaction mixture was allowed to cool down to room temperature to obtain a blue colored precipitate. The precipitate was triturated with ice-cold diethyl ether (40mL) for 15min. The

precipitate was filtered through frit glass, washed with cold diethyl ether (3 x 5mL), dried in vacuum yielding 4-(1,1,2-trimethyl-1H-benzo[e]indol-3-ium-3-yl)butane-1-sulfonate.

2.5.4(B) Synthesis of 3-(5-carboxypentyl)-1,1,2-trimethyl-1H-benzo[e]indol-3-ium (Figure 2.24)

The published synthesis procedure (from Wang et al. (2014)), which is an alteration of the synthetic procedure in Carreon et al. (2007) will be followed.

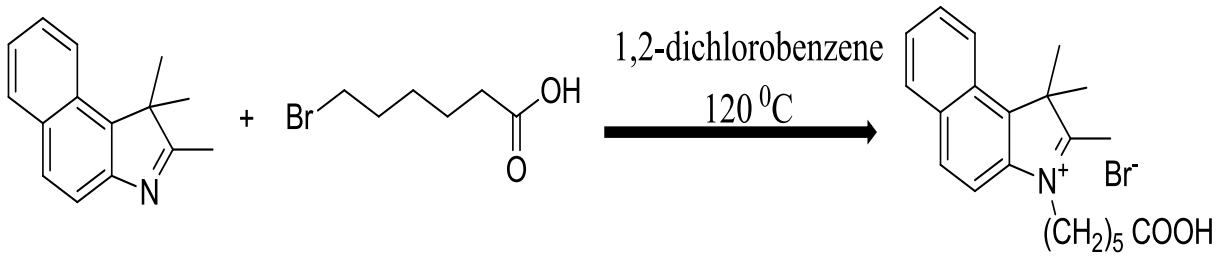

Figure 2.24: Reaction scheme for synthesis of 3-(5-carboxypentyl)-1,1,2-trimethyl-1H-benzo[e]indol-3-ium.

A two-necked 50 mL round bottom flask fitted with reflux condenser and stirring bar was be charged with 1,1,2-trimethyl-1H-benzo[e]indole, (1.0g, 4.78mmol) which was flushed with argon three times. After dissolving in dry o-dichlorobenzene (15 mL), (0.93g, 4.78mmol) of 6-bromohexanoic acid was added. The reaction mixture was stirred for 36h at 120 ^{o}C by using an oil bath. This will result in a dark blue solution. The reaction mixture was allowed to cool down to room temperature. This cooled solution was triturated with 1:1 diethyl ether and hexane mixture (total volume 90 mL) for an hour. The blue precipitate will be filtered off, washed with diethyl ether (3 x 20mL) and dried in vacuum yielding 3-(5-carboxypentyl)-1,1,2-trimethyl-1H-benzo[e]indol-3-ium.

2.5.4(C) Synthesis of Cyanine 5.5 (4-(2-((1E,3E,5E)-5-(3-(5-carboxypentyl)-1,1-dimethyl-1H-benzo[e]indol-2(3H)-ylidene)penta-1,3-dien-1-yl)-1,1-dimethyl-1H-benzo[e]indol-3-ium-3-yl)butane-1-sulfonate, bromide salt) (Figure 2.25)

The published synthesis procedure (from Wang et al. (2014)), which is an alteration of the synthetic procedure in Carreon et al. (2007), was followed.

A 50mL two-necked oven dry round bottom flask fitted with a magnetic stir bar was flushed with argon. Indolium salt, 1 (0.1g, 0.29 mmol) and malondialdehyde bis(phenylimine) monohydrochloride 2 (0.09g, 0.35mmol) were charged into the 50mL round bottom flask. Acetic anhydride (10mL) was added to this mixture and slowly heated to 120 ^{o}C in an oil bath and the reaction was monitored through TLC. The reaction was allowed to remain at 120 ^{o}C for half an hour. The reaction was then cooled to room temperature. An indolium salt, 3 (0.175g, 0.433mmol) in dry pyridine (5mL) was added to the above reaction dropwise. The reaction was allowed to stir at room temperature for 16h. The mixture was, then, concentrated in a rotavap and the residue was dissolved in CH_2Cl_2 (3mL) and loaded on silica column chromatography with CH_2Cl_2: MeOH solvent system (total volume = 2L). A gradient of 100% to 25% of solvent CH_2Cl_2 was used to obtain 0.21g of a deep blue colored dye. Percentage yield of cyanine 5.5: 92%. 1H NMR (DMSO-d6, 400 MHz) δ (ppm): 8.48 (t, J=12Hz, 2H), 8.24(d, J=8.2Hz, 2H), 8.06(m, 2H), 7.78(m, 1H), 7.67(m, 1H), 7.51(m, 2H), 6.65(dd, J=8Hz, 1H), 6.44(d, J=12Hz, 1H), 6.33(d, J=12Hz, 1H), 4.23(m, 4H), 3.0(m, 2H), 2.08(m, 2H), 1.96(m, 2H), 1.78(s, 16H), 1.57(m, 2H), 1.42(m, 2H).

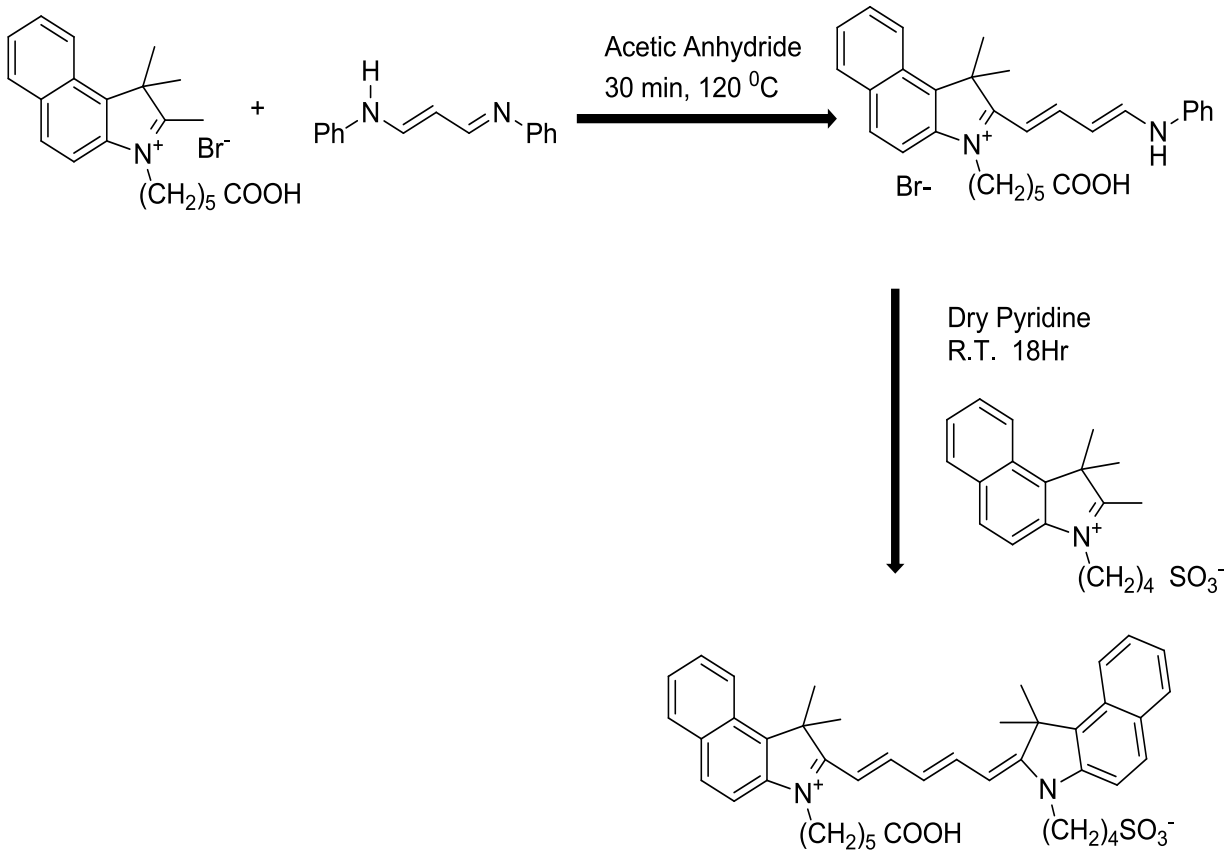

Figure 2.25: Reaction scheme for synthesis of Cyanine 5.5 (4-(2-((1E,3E,5E)-5-(3-(5-carboxypentyl)-1,1-dimethyl-1H-benzo[e]indol-2(3H)-ylidene)penta-1,3-dien-1-yl)-1,1-dimethyl-1H-benzo[e]indol-3-ium-3-yl)butane-1-sulfonate, bromide salt)

2.5.5. Peptide synthesis

The oligopeptides used as consensus sequences, which were synthesized in the Bossmann group by means of solid-supported peptide synthesis [20], are summarized in Table 2.1. Trityl-resin was used as a matrix polymer solid support. Peptide synthesis can be completed in the same peptide synthesis tube by the repetitive steps in addition of specific amino acid, filtration and washings, accordingly. Commercially available N-terminal protected C-terminal amino acids were used for the synthesis[53].

Protease	**Consensus Sequence**	**Isoelectric Point (pI)**	**Hydrophobicity Index at pH=6.8**
MMP1	GAG**VPMS-MRGG**AG	11.18	18.54
MMP2	GAG**IPVS-LRSG**AG	11.18	22.08
MMP3	GAG**RPFS-MIMG**AG	11.18	27.77
MMP7	GAG**VPLS-LTMG**AG	6.09	30.31
MMP9	GAG**VPLS-LYSG**AG	6.0	28.08
MMP13	GAG**PQGLA-GQRGIV**AG	11.18	19.88
uPA	GAG**SGR-SA**G	11.18	22.08
Cathepsin (CTS) B	GAG**SLLKSR-MVPNFN**AG	11.6	20.82
Cathepsin (CTS) L	GAG**SGVVIA-TVIVIT**AG	6.09	43.82

Table 2.10: Consensus sequences in single-letter code for 9 proteases. Essential amino acids of the consensus sequences are bold. (http://www.lifetein.com/peptide-analysis-tool.html)

The resin was preloaded into the peptide synthesis tube and swelled in dichloromethane (DCM) for 20 minutes and then filtered. DCM was washed away by five consecutive of N,N-Dimethylformamide (DMF) washings. A mixture of Fmoc protected amino acid and O-Benzotriazole-N,N,N',N'tetramethyl-uronium-hexafluoro-phosphate (HBTU) as coupling agent were added, swirled 30 minutes, and then filtered. This step was repeated once. Excess amino acid and the coupling agent were washed away by five DMF washings. Then 20% piperidine in DMF was used for N-deprotection. Subsequent amino acid coupling was performed after N-deprotection. The oligopeptides used as consensus sequence were synthesized using amino acid by amino acid from C-terminus to N-terminus[53]. The peptide synthesis process is schematically represented in Figure 2.26.

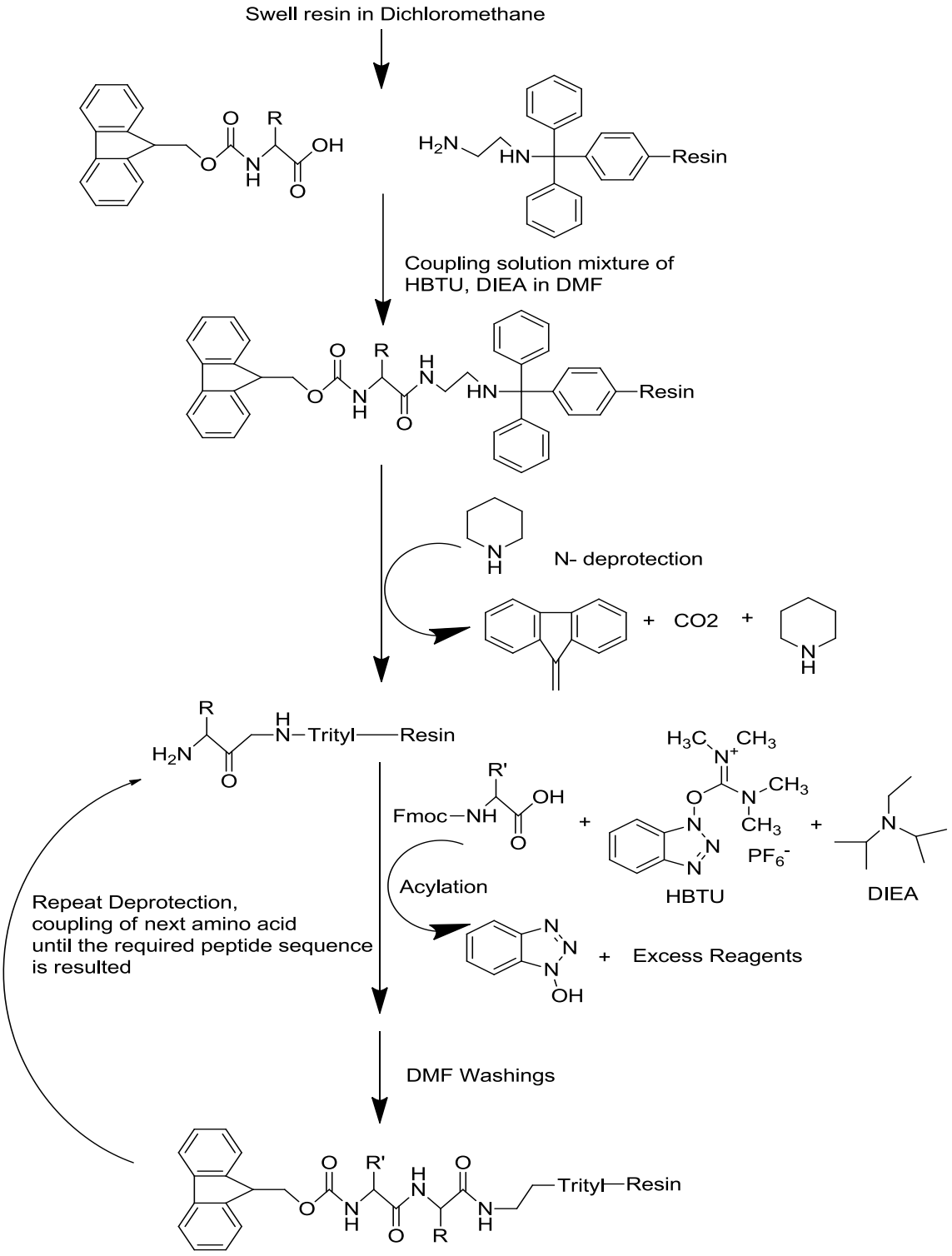

Figure 2.26: Schematic representation of solid phase peptide synthesis process

2.5.6. Coupling of TCPP to the Oligopeptide Consensus Sequences

TCPP is connected to the N-terminal of the oligopeptides while it was still on the resin, following same coupling conditions as for an amino acid.

Finally, the TCPP conjugated oligopeptide was then cleaved off the resin and also the side chain protecting groups were removed using a mixture of TFA, TIPS and water (95: 2.5 : 2.5). TCPP-oligopeptide was precipitated in cold ether and collected by centrifuging at 10000rpm. After precipitation, several DMF washings were carried out to remove the excess of unreacted TCPP and other reagents. Three final ether washings were carried out, in order to remove leftover DMF.

2.5.7. Nanoplatform Synthesis

The published synthesis procedure (from Wang et al. (2014), is reproduced here. 200 mg of dopamine coated Fe/Fe3O4 nanoparticles were dispersed in 5 mL of DMF. 200 mg of dopamine coated Fe/Fe3O4 nanoparticles were dispersed in 5 mL of DMF. A solution of 3 mmol of Cy5.5, 3.3 mmol of EDC, 1 mmol of DMAP in 1 mL of DMF was added to this dispersion. After sonicating for 1 h, the nanoparticles were precipitated by a magnet, and thoroughly washed with DMF (1 mL × 10). The TCPP-oligopeptide was linked to the primary amine groups of Fe/Fe_3O_4-bound via an amide bond [20]. Note that these sequences also contain GAG and AG as peptide linkers. The recovered nanoparticles were redispersed in 5 mL of DMF, and to this dispersion, 2 mmol of TCPP linked peptide sequence, 2.2 mmol of EDC, 1 mmol of DMAP in 2 mL of DMF were added. After sonicating for 1 h, the nanoparticles were precipitated by a magnet (0.55T), and thoroughly washed with DMF (1 mL × 10). After drying in high vacuum, 170-185 mg of nanoplatform can be obtained. The composition of the nanoplatform was

analyzed by means of UV-Vis spectroscopy (Agilent HP 8543A). After combining all washing fractions and subsequent solvent removal in high (682nm) = 5.17) were taken up in 1.0 ml methanol and quantitatively measured taking advantage of their high absorption coefficients. The nanoplatforms were dispersed in PBS, and TCPP and cyanine 5.5 were measured by UV/Vis-spectroscopy as well, using dopamine coated Fe/Fe3O4-nanoparticles in PBS as the reference. The iron-content of the nanoplatforms was independently determined using the ferrozine assay.2 This resulting data, together with the size of the Fe/Fe3O4-nanoparticles, enables the calculation of the average ratio of TCPP and cyanine 5.5 per nanoparticle.

2.5.8. Standard procedure of preparing protease assays (without serum)

3.0 mg of nanoplatform were dissolved in 3.0 ml of PBS. The dispersion was sonicated for 10 min. The resulting dispersion is chemically stable for 14 days at 4°C. 900 mg of dextran were dissolved in 90 ml of PBS. Stock solutions of all 9 enzymes were prepared by consecutive dilution of commercially available proteases (Enzo Lifesciences). 3 ml of PBS–dextran (10 mg dextran in 1.0 ml of PBS) are mixed with 75 µl of the nanoplatform dispersion (3.0 mg in 3.0 ml of PBS, see above) and 30 µl of each of the proteases at every concentration level in PBS. The dispersions were incubated at 25°C for 60min, followed by the recording of a fluorescence spectrum at 25°C using a Fluoromax2 spectrometer (λ_{em} = 421nm, λ_{ex} = 620 – 680nm).

2.5.9. Standard procedure of preparing protease assays (with inactivated serum)

3.0 mg of nanoplatform were dissolved in 3.0 ml of PBS. The dispersion was sonicated for 10 min. The resulting dispersion is chemically stable for 14 days at 277 K. 900 mg of dextran were dissolved in 90 ml of PBS. Stock solutions of all 9 enzymes were prepared by consecutive dilution of commercially available proteases (Enzo Lifesciences). 3 ml of PBS–dextran (10 mg dextran in 1.0 ml of PBS) are mixed with 75 μl of the nanoplatform dispersion (3.0 mg in 3.0 ml of PBS, see above), 30 μl of inactivated serum, and 30 μl of each of the proteases at every concentration level in PBS. The dispersions were incubated at 25ºC for 60min., followed by the recording of a fluorescence spectrum at 25ºC using a Fluoromax2 spectrometer (λ_{ex} = 421nm, λ_{em} = 620 – 680nm). Inactivation of serum was achieved by heating to 56ºC in an incubator for 45min., taking the heating time of the serum from RT to the chosen temperature into account, making sure that the serum is heated for a minimum of 30min. Inactivated serum tested negative with all nine nanoplatforms for protease measurements employed in this study.

References

1. Bogenrieder, T.; Herlyn, M. *Oncogene* **2003,***22* (42), 6524-6536.
2. Radisky, D. C.; Levy, D. D.; Littlepage, L. E.; Liu, H.; Nelson, C. M.; Fata, J. E.; Leake, D.; Godden, E. L.; Albertson, D. G.; Nieto, M. A.; Werb, Z. *Nature* **2005,***436* (7047), 123-127.
3. Grotsky, D. A.; Gonzalez-Suarez, I.; Novell, A.; Neumann, M. A.; Yaddanapudi, S. C.; Croke, M.; Martinez-Alonso, M.; Redwood, A. B.; Ortega-Martinez, S.; Feng, Z.; Lerma, E.; Ramon y Cajal, T.; Zhang, J.; Matias-Guiu, X.; Dusso, A.; Gonzalo, S. *J Cell Biol* **2013,***200* (2), 187-202.
4. Mahmood, U.; Weissleder, R., *Mol Cancer Ther* **2003,***2* (5), 489-496.
5. Pham, W.; Weissleder, R.; Tung, C.-H.*Angew. Chem., Int. Ed.* **2002,***41* (19), 3659-3662.
6. Pham, W.; Choi, Y.; Weissleder, R.; Tung, C. H.*Bioconjug Chem* **2004,***15* (6), 1403-1407.
7. Zhao, M.; Josephson, L.; Tang, Y.; Weissleder, R.*Angew. Chem., Int. Ed.* **2003,***42* (12), 1375-1378.
8. Funovics, M.; Weissleder, R.; Tung, C. H.*Anal Bioanal Chem* **2003,***377* (6), 956-963.
9. Turk, B. E.; Huang, L. L.; Piro, E. T.; Cantley, L. C. *Nat. Biotechnol.* **2001,***19* (7), 661-667.
10. Jaffer, F. A.; Libby, P.; Weissleder, R.*J. Am. Coll. Cardiol.* **2006,***47* (7), 1328-1338.
11. Quillard, T.; Croce, K.; Jaffer, F. A.; Weissleder, R.; Libby, P.*Thromb Haemost* **2011,***105* (5), 828-836.
12. Kelly, K. A.; Bardeesy, N.; Anbazhagan, R.; Gurumurthy, S.; Berger, J.; Alencar, H.; Depinho, R. A.; Mahmood, U.; Weissleder, R.*PLoS Med* **2008,***5* (4), e85.
13. von Burstin, J.; Eser, S.; Seidler, B.; Meining, A.; Bajbouj, M.; Mages, J.; Lang, R.; Kind, A. J.; Schnieke, A. E.; Schmid, R. M.; Schneider, G.; Saur, D.*Int J Cancer* **2008,***123* (9), 2138-2147.

14. Bossmann, S. H.; Troyer, D. L.*Expert Rev Mol Diagn* **2013,***13* (2), 107-109.

15. Liang, J.; Liu, H.; Huang, C.; Yao, C.; Fu, Q.; Li, X.; Cao, D.; Luo, Z.; Tang, Y. *Anal Chem* **2015,***87* (11), 5790-5796.

16. Gao, Y.; Lam, A. W. Y.; Chan, W. C. W.*ACS Appl. Mater. Interfaces* **2013,***5* (8), 2853-2860.

17. Spindel, S.; Sapsford, K. E. *Sensors* **2014,***14* (12), 22313-22341.

18. Joshi, G. K.; Deitz-McElyea, S.; Liyanage, T.; Lawrence, K.; Mali, S.; Sardar, R.; Korc, M.*ACS Nano* **2015,***9* (11), 11075-11089.

19. Bossmann, S. H.; Basel, M. T.; Troyer, D. L.Protease Detection, Kansas State University Research Foundation, US Patent# 8,969,027, 2015.

20. Wang, H.; Udukala, D. N.; Samarakoon, T. N.; Basel, M. T.; Kalita, M.; Abayaweera, G.; Manawadu, H.; Malalasekera, A.; Robinson, C.; Villanueva, D.; Maynez, P.; Bossmann, L.; Riedy, E.; Barriga, J.; Wang, N.; Li, P.; Higgins, D. A.; Zhu, G.; Troyer, D. L.; Bossmann, S. H. *Photochem Photobiol Sci* **2014,***13* (2), 231-240.

21. Jennings, T. L.; Singh, M. P.; Strouse, G. F. *J. Am. Chem. Soc.* **2006,***128* (16), 5462-5467.

22. Selvin, P. R.*Nat Struct Biol* **2000,***7* (9), 730-734.

23. Udukala, D. N. "Protease assays for cancer diagnostics". Doctoraldissertation, Kansas State University, 2014.

24. Chang, W.-S.; Willingham, B.; Slaughter, L. S.; Dominguez-Medina, S.; Swanglap, P.; Link, S.*Acc. Chem. Res.* **2012,***45* (11), 1936-1945.

25. Singletary, S. E.; Connolly, J. L.,*CA Cancer J Clin* **2006,***56* (1), 37-47; quiz 50-1.

26. Howlader, N.; Noone, A. M.; Krapcho, M.; Garshell, J.; Neyman, N.; Altekruse, S. F.; Kosary, C. L.; Yu, M.; Ruhl, J.; Tatalovich, Z.; Cho, H.; Mariotto, A.; Lewis, D. R.; Chen, H. S.; Feuer, E. J.; Cronin, K. A.SEER Cancer Statistics Review, 1975-2010 National Cancer

Institute Bethesda, MD; http://seer.cancer.gov/csr/1975_2010/, based on November 2012 SEER data submission.

27. Siegel, R.; DeSantis, C.; Virgo, K.; Stein, K.; Mariotto, A.; Smith, T.; Cooper, D.; Gansler, T.; Lerro, C.; Fedewa, S.; Lin, C.; Leach, C.; Cannady, R. S.; Cho, H.; Scoppa, S.; Hachey, M.; Kirch, R.; Jemal, A.; Ward, E.*CA Cancer J Clin* **2012,***62* (4), 220-241.
28. World Health Organization Global Health Observatory Data Repository, Mortality and Global Health Estimates 2012. apps.who.int/gho/data/?theme=main. Accessed September05, 2015.
29. Warren, A. D.; Kwong, G. A.; Wood, D. K.; Lin, K. Y.; Bhatia, S. N.*Proc. Natl. Acad. Sci. U. S. A.* **2014,***111* (10), 3671-3676.
30. Pantel, K.; Alix-Panabieres, C.*Cancer Res* **2013,***73* (21), 6384-6388.
31. Ben-Avraham, D.; Schulman, L. S.; Bossmann, S. H.; Turro, C.; Turro, N. J. *J. Phys. Chem. B* **1998,***102* (26), 5088-5093.
32. Kristensen, V. N.; Vaske, C. J.; Ursini-Siegel, J.; Van Loo, P.; Nordgard, S. H.; Sachidanandam, R.; Sorlie, T.; Warnberg, F.; Haakensen, V. D.; Helland, A.; Naume, B.; Perou, C. M.; Haussler, D.; Troyanskaya, O. G.; Borresen-Dale, A.-L.*Proc. Natl. Acad. Sci. U. S. A.* **2012,***109* (8), 2802-2807, S2802/1-S2802/12.
33. Cheang, M. C.; Chia, S. K.; Voduc, D.; Gao, D.; Leung, S.; Snider, J.; Watson, M.; Davies, S.; Bernard, P. S.; Parker, J. S.; Perou, C. M.; Ellis, M. J.; Nielsen, T. O.*J Natl Cancer Inst* **2009,***101* (10), 736-750.
34. van Domselaar, R.; de Poot, S. A.; Bovenschen, N.*Expert Rev Proteomics* **2010,***7* (3), 347-359.
35. Mansfield, L.; Subramanian, A.; Devalia, H.; Jiang, W.; Newbold, R. F.; Mokbel,

K.*Anticancer Res* **2007,***27* (4B), 2265-2268.

36. Davidson, B.; Reich, R.; Risberg, B.; Nesland, J. M.*Arkh Patol* **2002,***64* (3), 47-53.
37. Duffy, M. J.; Maguire, T. M.; Hill, A.; McDermott, E.; O'Higgins, N.*Breast Cancer Res* **2000,***2* (4), 252-257.
38. Asiedu, M. K.; Ingle, J. N.; Behrens, M. D.; Radisky, D. C.; Knutson, K. L.*Cancer Res* **2011,***71* (13), 4707-4719.
39. Xing, R. H.; Rabbani, S. A.*Int J Cancer* **1996,***67* (3), 423-429.
40. Gondi, C.S.; Rao, J. S. *Expert Opin Ther Targets***2013**, *17*, 281-291.
41. http://www.cellgrow.com/heat-inactivation/
42. Antoniou, E.; Alexandridis, P.; Tstanou, M. Nova Science Publishers, Inc., 2014.
43. Pieper, R.; Gatlin, C. L.; Makusky, A. J.; Russo, P. S.; Schatz, C. R.; Miller, S. S.; Su, Q.; McGrath, A. M.; Estock, M. A.; Parmar, P. P.; Zhao, M.; Huang, S.-T.; Zhou, J.; Wang, F.; Esquer-Blasco, R.; Anderson, N. L.; Taylor, J.; Steiner, S.*Proteomics* **2003,***3* (7), 1345-1364.
44. Thompson, J. M.*Anal. Proc. (London)* **1988,***25* (11), 363-365.
45. Welch, B. L.*Biometrika* **1947,***34* (1-2), 28-35.
46. Swellam, M.; Soliman, H. A.; Abdelmaksoud, M. D.; Nageeb, A. M.; El Arab, L. R.; Boshnak, H.*Cancer Biomark* **2014,***14* (6), 409-417.
47. Wang, H.; Shrestha, T. B.; Basel, M. T.; Dani, R. K.; Seo, G.-M.; Balivada, S.; Pyle, M. M.; Prock, H.; Koper, O. B.; Thapa, P. S.; Moore, D.; Li, P.; Chikan, V.; Troyer, D. L.; Bossmann, S. H. *Beilstein J. Nanotechnol.* **2012,***3*, 444-455, 12 pp.
48. Sobczynski, J.; Tonnesen, H. H.; Kristensen, S.*Pharmazie* **2013,***68* (2), 100-109.
49. Patsenker, L.; Tatarets, A.; Kolosova, O.; Obukhova, O.; Povrozin, Y.; Fedyunyayeva, I.; Yermolenko, I.; Terpetschnig, E. *Ann N Y Acad Sci* **2008,***1130*, 179-187.

50. Wang, H.; Shrestha, T. B.; Basel, M. T.; Dani, R. K.; Seo, G.; Balivada, S.; Pyle, M. M.; Prock, H.; Koper, O. B.; Thapa, P. S. Magnetic-Fe/Fe3O4-nanoparticle-bound SN38 as carboxylesterase-cleavable prodrug for the delivery to tumors within monocytes/macrophages. *Beilstein journal of nanotechnology*. **2012**, *3*, 444-455.
51. Pereira, M. M.; Monteiro, C. J.; Peixoto, A. F. Meso-substituted porphyrin synthesis from monopyrrole: An overview. *Targets in Heterocyclic Systems.Chemistry and Properties.* , *12*, 258.
52. Carreon, J. R.; Stewart, K. M.; Mahon Jr, K. P.; Shin, S.; Kelley, S. O. Cyanine dye conjugates as probes for live cell imaging. *Bioorg. Med. Chem. Lett.* **2007**, *17*, 5182-5185.
53. Amblard, M.; Fehrentz, J.; Martinez, J.; Subra, G. Methods and protocols of modern solid phase peptide synthesis. *Mol. Biotechnol.* **2006**, *33*, 239-254.

Chapter 3 - Nanoplatforms for the Detection of Arginase

Acknowledgements

I would like acknowledge all the collaborators, who contributed their knowledge and expertise towards the success of this project. This study was supported by the National Science Foundation (DMR-1242765 and CBET-1337438), as well as Kansas State University.

This material described in chapter 3 will lead to a publication in the near future. I have designed the nanoplatform for arginase detection, utilizing the Fe/Fe_3O_4-nanoparticles synthesized by Dr. Wang. I would like to thank Dr. Emily McLaurin for performing the TEM measurements.

Malalasekera, A. P.; Wang, H.; Samarakoon, T. N.; Udukala, D. N. Ortega, R.; Shrestha, T. B.; Troyer, D. L.; Bossmann, S. H., Nanoplatforms for the Detection of Arginase Activities. *Nanomedicine NBM* **2016,** *in preparation*.

3.1. Abstract

The enzyme arginase, which is overexpressed in many solid tumors, is able to degrade the amino acid arginine. L-arginine deficiency is resulting in an impaired immune system. Two nanoplatforms for arginase detection were designed and synthesized. Both feature a central dopamine-coated iron/iron oxide nanoparticle to which sulfonated cyanine 7.0 or cyanine 7.5 is tethered via stable amide bonds. In both nanoplatforms, cyanine 5.5 is linked to the N-terminal of the peptide sequence GRRRRRRRG. Arginine (R) reacts to ornithine (O) in the presence of arginase II. This chemical transformation occurs without proteolytic cleavage of the oligopeptide. This is the first example for the "posttranslational sensor", which permits detection of arginase within an hour. It is noteworthy that the nanoplatforms for arginase detection do not show a fluorescence increase when incubated with the enzyme NO-reductase, which also uses arginase as substrate, but is indicative of an immune response by the host to cancer and infections. The arginase activity was determined in a syngeneic mouse model for aggressive breast cancer (4T1 tumors in BALB/c mice). It was found that the arginase activity is systemically enhanced, but especially pronounced in the active tumor regions.

Keywords: Posttranslational sensor, arginase detection, iron/iron oxide nanoparticle-based nanoplatform, fluorescence detection

3.2. Introduction

Arginase metabolizes L-arginine to L-ornithine and urea [1]. Besides its fundamental role in the hepatic urea cycle, arginase is a key player in the immune system. In humans, arginase I is constitutively expressed in polymorphonuclear neutrophils, released during inflammation and responsible for the down-regulation of nitric oxide synthesis by converting arginine to ornithine. Arginase-mediated L-arginine depletion is capable of suppressing T cell immune responses, leading to inflammation-associated immune-suppression, which is a hallmark of aggressive solid tumors [2]. Furthermore, L-arginine insufficiency is also responsible for dysfunction of natural killer (NK) cells, which are vital for early host defense against infections and tumors [3]. Arginase can be found in mammalian bodies in two isoforms: arginase I and arginase II. Whereas arginase I is (mainly) a liver enzyme [4], arginase II can be found, in varying concentrations, in tissue [5]. Arginase I has been recognized as a biomarker for pancreatic adenocarcinoma [6]. Arginase II is expressed in cancer-associated fibroblasts and indicates tissue hypoxia and predicts poor outcome in patients with pancreatic cancer [7]. However, since fast, reliable and sensitive plate reader tests for arginase detection are not available to date, numerous potential other applications for this technology can be envisioned [8]. Colorimetric arginase tests kits are commercially available. The most sensitive test to data has a limit of detection (LOD) of 2×10^{-7} moles L^{-1}[9]. In this UV/Vis-absorption-based assay, arginase reacts with arginine and undergoes a series of reactions to form a colored product (λ_{max}= 570 nm). The aim of this endeavor is to design a fluorescence-based arginase sensor that is equally sensitive as the technically more complex immunoassays (target LOD: sub-picomolar) [10].

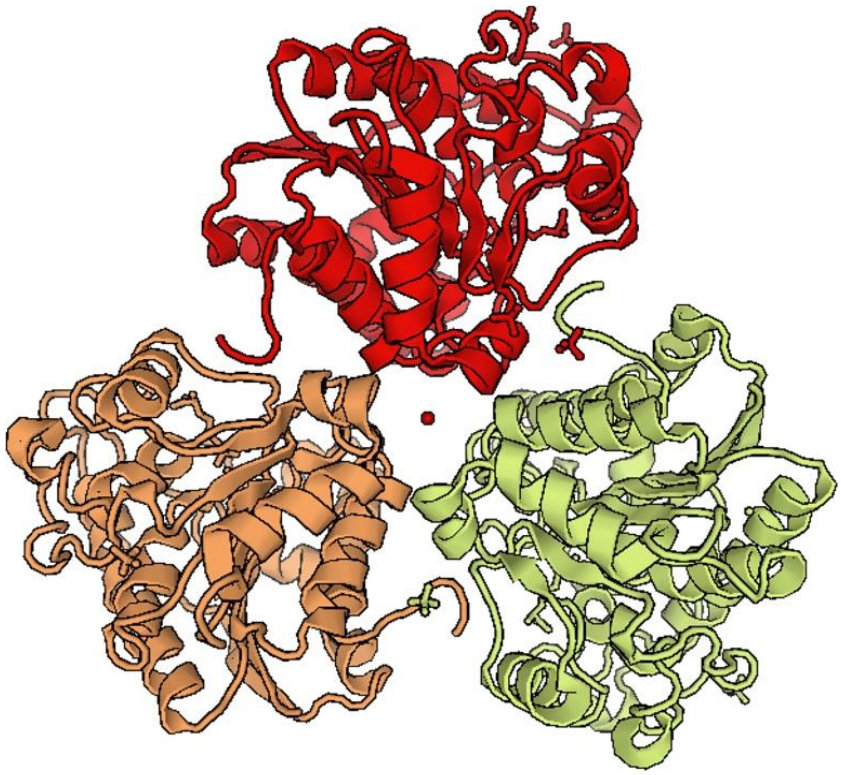

Figure 3.1: X-ray structure of Arginase II (1PQ3)
(http://www.rcsb.org/pdb/pv/pv.do?pdbid=1PQ3&bionumber=1, accessed on 02/12/2016).

Arginases I and II belong to the family of ureohydrolases. Mammalian arginase II is active as a trimer [11]. It requires a manganese cluster to maintain its function. Mn^{2+} coordinates and activates H_2O, thus enabling it to act as effective nucleophile. It is noteworthy that arginase II, contrary to NO-reductase, is not only able to transform free arginine to ornithine, but to catalyze the same reaction if arginine is part of am oligopeptide. The transformation of arginine into ornithine proceeds stepwise and most likely in a random pattern. It ends when all seven arginine units in GRRRRRRRG (pI: 12.78) [12] have been transformed into GOOOOOOOG (pI: 5.52). Assuming a random reaction pattern also means that 176 different reaction intermediates can be formed.

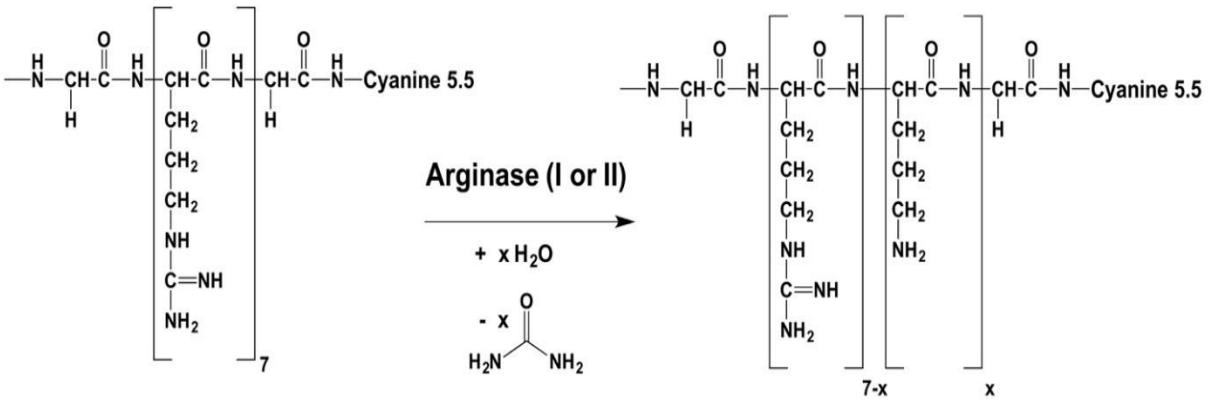

Scheme 3.1: Transformation of GRRRRRRRG into GOOOOOOOR (G: L-glycine, R: L-arginine, O: L-ornithine; stereochemistries not shown)). In each step, urea is hydrolytically cleaved off L-arginine to form L-ornithine. Note that the left side of the oligopeptide is bound to dopamine, which is anchored at the surface of the central iron/iron oxide nanoparticle of the nanoplatform.

The posttranslational arginase sensors utilize cyanine dyes as FRET (Förster Resonance Energy Transfer) probes [13]. Cyanine 5.5 (donor) and cyanines 7.0/7.5 (acceptors) form attractive FRET-pairs, as indicated in Scheme 2, because of the significant spectra overlap between the fluorescence spectrum of cyanine 5.5 and the absorption spectra of both, cyanine 7.0 and 7.5. Furthermore, all cyanine dyes are characterized by their large molecular extinction coefficients and their narrow absorption and emission bands [14]. It should be noted that cyanine dyes have very short fluorescence lifetimes in the range of 200 to 350ps in water [15]. Therefore, they are essentially not quenched by oxygen. Cyanine dyes have reasonable fluorescence quantum yields ranging between 5 and 10 percent in aqueous buffers and *in-vivo* [16].

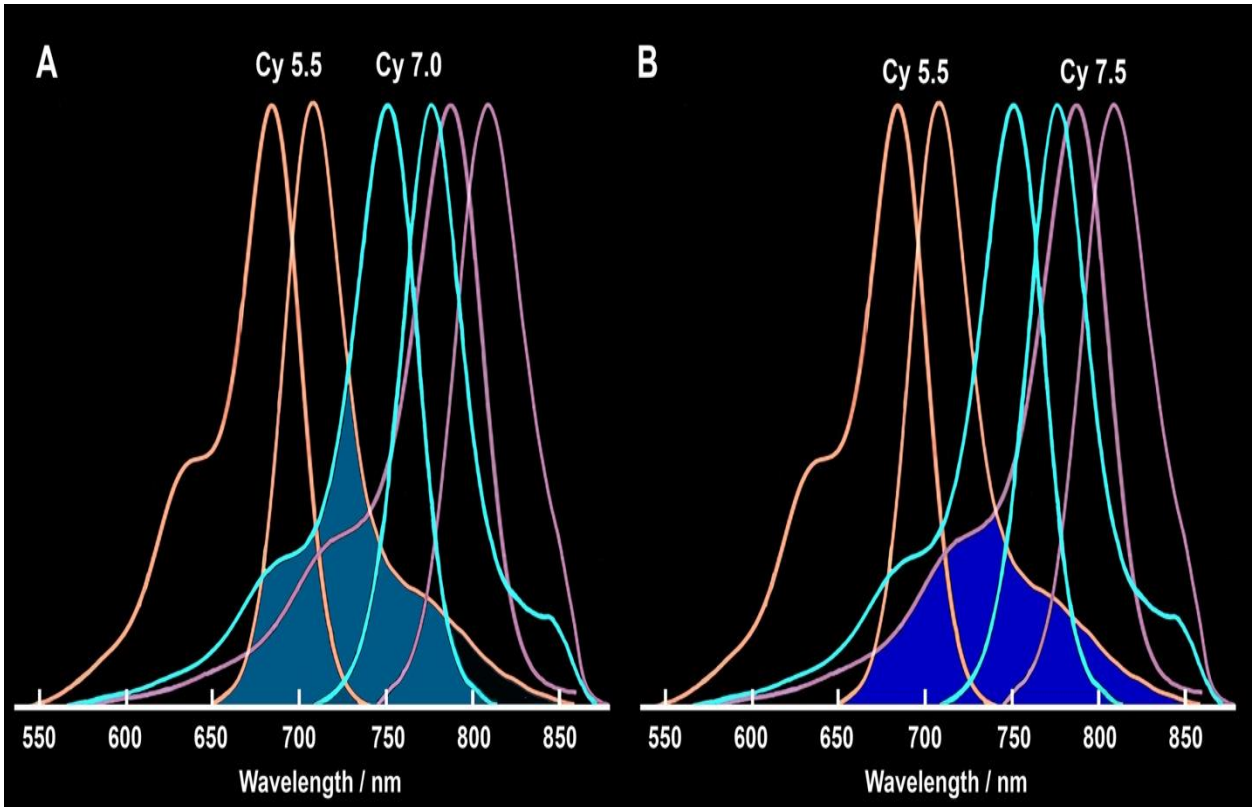

Scheme 3.2: Spectral overlap between the potential Förster Resonance Transfer pairs Cyanine 5.5/Cyanine 7.0 and Cyanine 5.5/Cyanine 7.5. The absorption and emission spectra of the cyanines are normalized. From this estimation, the spectral overlap in both FRET pairs appears to be of the same order of magnitude. Information from www.lumiprobe.com was utilized in preparing this scheme.

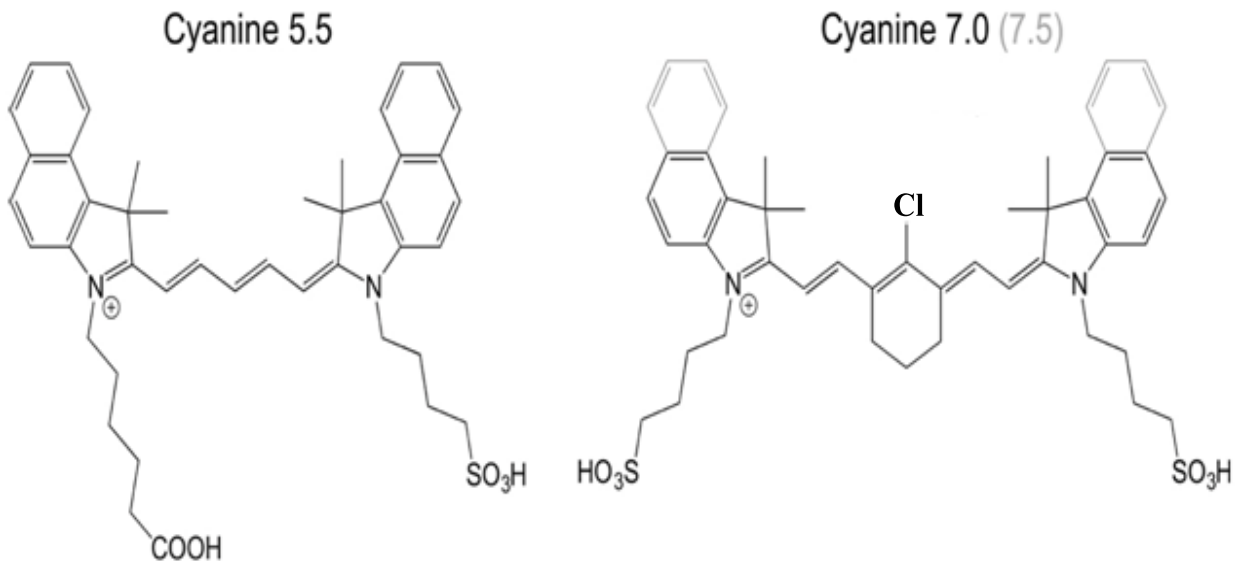

Figure 3.2: Cyanine Dyes used in this study. The extended structure of cyanine 7.5 is marked in gray. The synthesis of the cyanine dyes is described in the Experimental section.

3.3. Results and Discussion

The nanoplatforms for arginase detection were designed from the following components:

1) The central Fe/Fe_3O_4 core/shell nanoparticle. As transmission electron microscopy (TEM) indicates, the average Fe(0) core diameter of the Fe/Fe_3O_4-nanoparticles is 17±0.5 nm and the Fe_3O_4 shell thickness of 3.0±0.5 nm. The polycrystalline nanoparticles were synthesized synthesized by thermal decomposition of $Fe(CO)_5$ in the presence of oleylamine and hexadecylammonium chloride (HADxHCl) using 1-octadecene (ODE) as solvent[17]. The optimization of this synthetic procedure by Dr. Hongwang Wang is described in the "Synthetic Procedures" section below. Dopamine was chosen as organic coating of the Fe/Fe_3O_4-nanoparticles, because, as a typical catechol, it strongly adhers to the Fe(III)-centers of magnetite (Fe_3O_4), with a binding constant of (conservatively estimated) 10^{20}l mol^{-1} [18]. Dopamine also increases the water-dispersibility of the inorganic nanoparticles to > 5 g L-1 [19], which is mandatory for their use in aqueous buffers.
2) Either cyanine 7.0 or cyanine 7.5 was tethered by means of stable amide bonds to the primary amine functions of dopamine. Both near-infrared dyes were selected as FRET acceptors, together with cyanine 5.5 as FRET donor (see below). It is noteworthy that the fluorescence lifetime of cyanines in water is too short to observe significant plasmonic quenching effects (also known as dipole-surface energy transfer (SET) [20]) between the central Fe/Fe_3O_4 nanoparticle and the attached cyanines. This is a substantial design change in comparison with earlier nanoplatforms from the Bossmann group, in which tetracarboxyphenyl-porphyrin (TCPP), was used as a fluorophore. TCPP shows fluorescence lifetimes in the nanosecond range, which increases SET significantly. The number of cyanine 7.0 or 7.5 FRET acceptors

per nanoparticle was estimated to 70±5, based on their Vis-absorption spectra, and assuming that the spectra did not significantly changed when attached to the inorganic nanoparticles.

3) Cyanine 5.5 was tethered to by means of the oligopeptide GRRRRRRRG (GR_7G) to the dopamine-covered Fe/Fe_3O_4 nanoparticles. The synthesis of the oligopeptide, and the attachment of GR_7G to the primary amine functions of the dopamine-coated nanoparticles were performed following procedures that were previously optimized in the Bossmann group [21, 22]. Cyanine 5.5 was attached to the N-terminal glycine of GR_7G while the oligopeptide was still bound to the resin, thus eliminating the possibility of unwanted side reactions. As shown in Scheme 2, cyanine 5.5 was chosen as FRET donor. Based on UV/Vis spectroscopy, we have estimated that 45±5 cyanine 5.5 dyes were attached to the inorganic nanoparticles via GR_7G tethers.

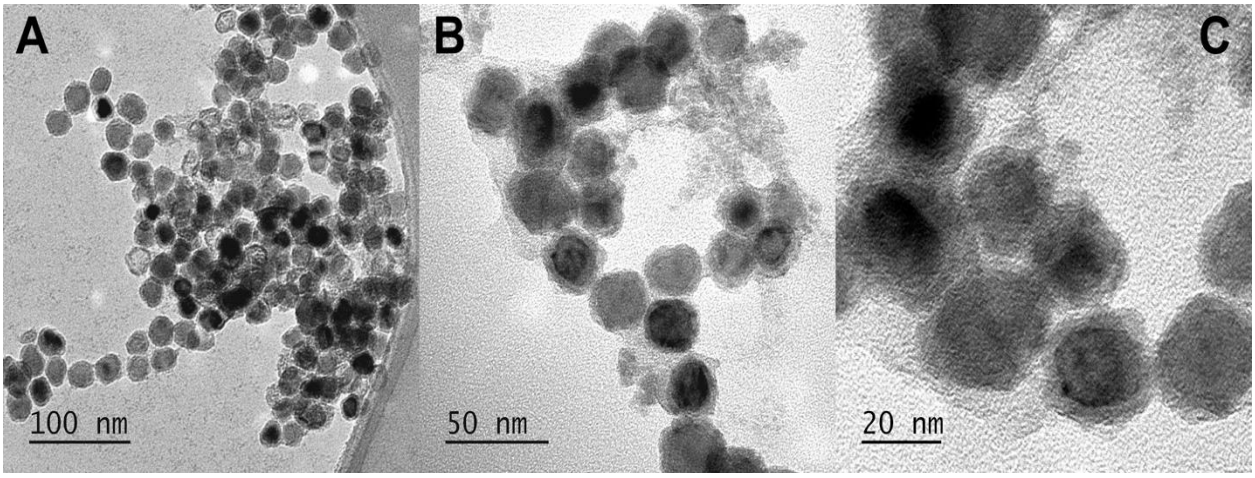

Figure 3.3: Transmission Electron Micrographs of the nanoplatforms for arginase detection, recorded by Assistant Prof. Dr. Emily McLaurin using the FEI Tecnai G2 Spirit BioTWIN, 120KV (GATAN digital imaging system and HAADF detector) TEM of the Nanotechnology Innovation Center at Kansas State University. A: dopamine-coated Fe/Fe_3O_4 nanoparticles; B:

dopamine-coated Fe/Fe_3O_4 nanoparticles featuring GR_7G-attached cyanine 5.5 and tethered cyanine 7.5; C: dopamine-coated Fe/Fe_3O_4 nanoparticles featuring GR_7G-attached cyanine 5.5 and tethered cyanine 7.0). C: dopamine-coated Fe/Fe_3O_4 nanoparticles featuring GR_7G-attached cyanine 5.5 and tethered cyanine 7.0).

Upon excitation at 680 nm, cyanine 5.5 reaches its excited singlet state, which spectrally overlaps with the absorption spectra of both, cyanine 7.0 and cyanine 7.5. The general equation for FRET processes is:

$$E = \frac{k_{ET}}{k_f + k_{ET} + \sum k_i} = \frac{1}{1 + \left(\frac{r}{R^0}\right)^6} \quad \text{Equation 1}$$

E: FRET efficiency, k_{ET}: rate of energy transfer, k_f: radiative decay rate, k_i's: rate constants of any other occurring deactivation processes, r: distance between donor and acceptor, R^0: Förster radius at which the energy transfer efficiency is 50%.

The Förster radii for cyanine dyes are ranging from 5 and 8 nm [23]. The maximal length of both oligopeptides GR_7G and GO_7G is 3.2 nm. Considering the principal geometry of the nanoplatform, cyanine 5.5 can easily undergo FRET with both, cyanine 7.0 and cyanine 7.5, because it is within the Förster radius of more than one FRET-acceptor. Since FRET processes feature a r^{-6} dependence of the distance between donor and acceptor, changes in tether mobility will directly either decrease or increase the FRET efficiency. It is our paradigm that the chemical transformation from arginine to ornithine is causing exactly this effect.

3.3.1. Calibration of the Nanoplatforms

Nanoplatform 1 (FRET pair cyanine 5.5 / cyanine 7.0) and nanoplatform 2 (FRET pair cyanine 5.5 / cyanine 7.5) were dispersed in PBS (1x phosphate buffered saline) (1mg / mL). The dispersion was then sonicated for 10 min. 70 µL of this stock solution was added to a series of 30µL arginase dilutions in 2900µL of dextran/PBS (10mg/ml) solution. The concentration was ranging from 5.22 x 10^{-6} to 5.22 x 10^{-13} moles of arginase II per liter of 1x PBS. Recombinant Arginase II was purchased from Sigma/Aldrich. After adding the nanoplatform for arginase detection, the dispersion was incubated at 37ºC for 1h. The resulting fluorescence was then measured using a Fluoromax 2 spectrofluorometer at 25ºC, excitation wavelength 680 nm. The results are shown in Figures 3.4 to 3.11.

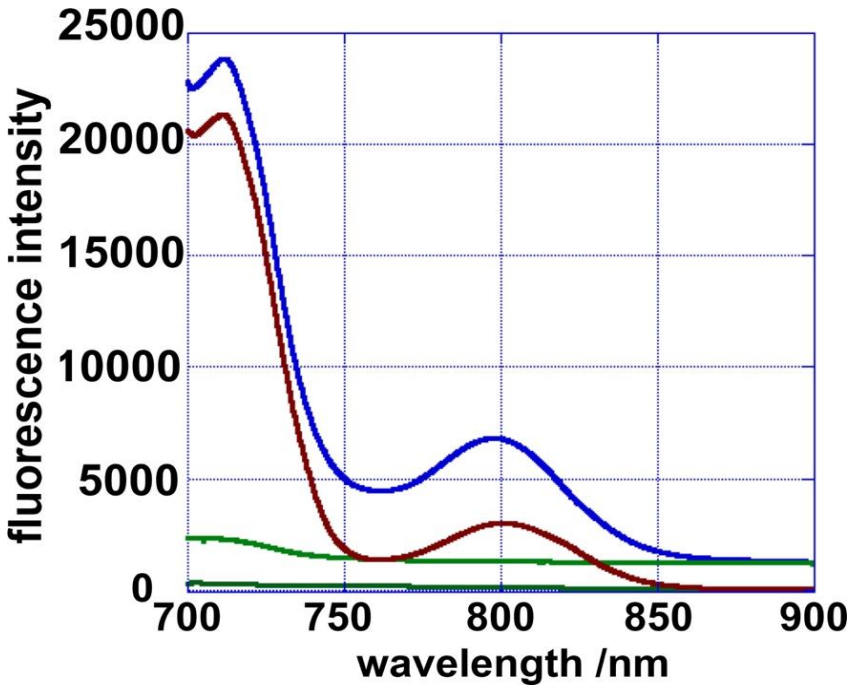

Figure 3.4: Steady-state fluorescence spectra of nanoplatform 1 (FRET pair cyanine 5.5 / cyanine 7.0) in PBS. Dark green line: PBS; light green line: 5.22 x 10^{-6} M arginase II in PBS; brown line: nanoplatform 1 in PBS in the absence of arginase after 1h of incubation at 37ºC; blue line: nanoplatform 1 in PBS after incubation with 5.22 x 10^{-6} M arginase II in PBS at 37ºC.

As Figure 3.4 shows, dual fluorescence from cyanine 5.5 (λ_{max} = 723nm) and cyanine 7.0 (λ_{max} = 794nm) is observed. After incubation with arginase II, an increase in cyanine 7.0 fluorescence is discerned, which indicates that FRET increases upon conversion of arginine to ornithine. It is noteworthy that the fluorescence of nanoplatform 1 increased after incubation with arginase II. I earlier studies, it was found that arginine was capable of forming a complex with a cyanine dye, which resulted in fluorescence quenching [24]. A similar effect is observed here, with the exception that cyanine 5.5 is tethered to GR_7G, which results in an "infinite" binding constant. The fluorescence quantum yield of nanoplatform 1 increases upon conversion of arginine to ornithine, because the latter does not form complexes with cyanine 5.5.

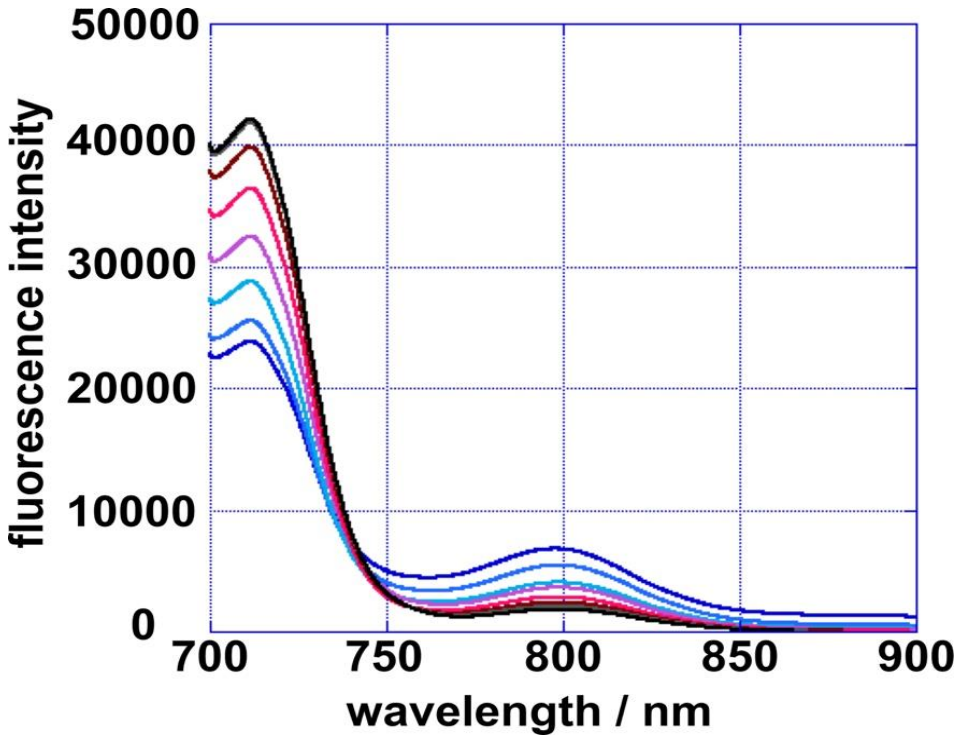

Figure 3.5: Steady-state fluorescence spectra of nanoplatform 1 (FRET pair cyanine 5.5 / cyanine 7.0) in PBS. Fluorescence spectra for the whole calibration (5.22 x 10^{-6} M to 5.22 x 10^{-13} M of arginase II in PBS, incubation at 37°C for 1h). Dark blue line: 5.22 x 10^{-6} M or arginase II; blue line: 5.22 x 10^{-7} M; light blue line: 5.22 x 10^{-8} M; pink line: 5.22 x 10^{-9} M; red line: 5.22 x 10^{-10}

M; brown line: 5.22 x 10^{-11} M, gray line: 5.22 x 10^{-12} M; black line: 5.22 x 10^{-13} M of arginase II in PBS.

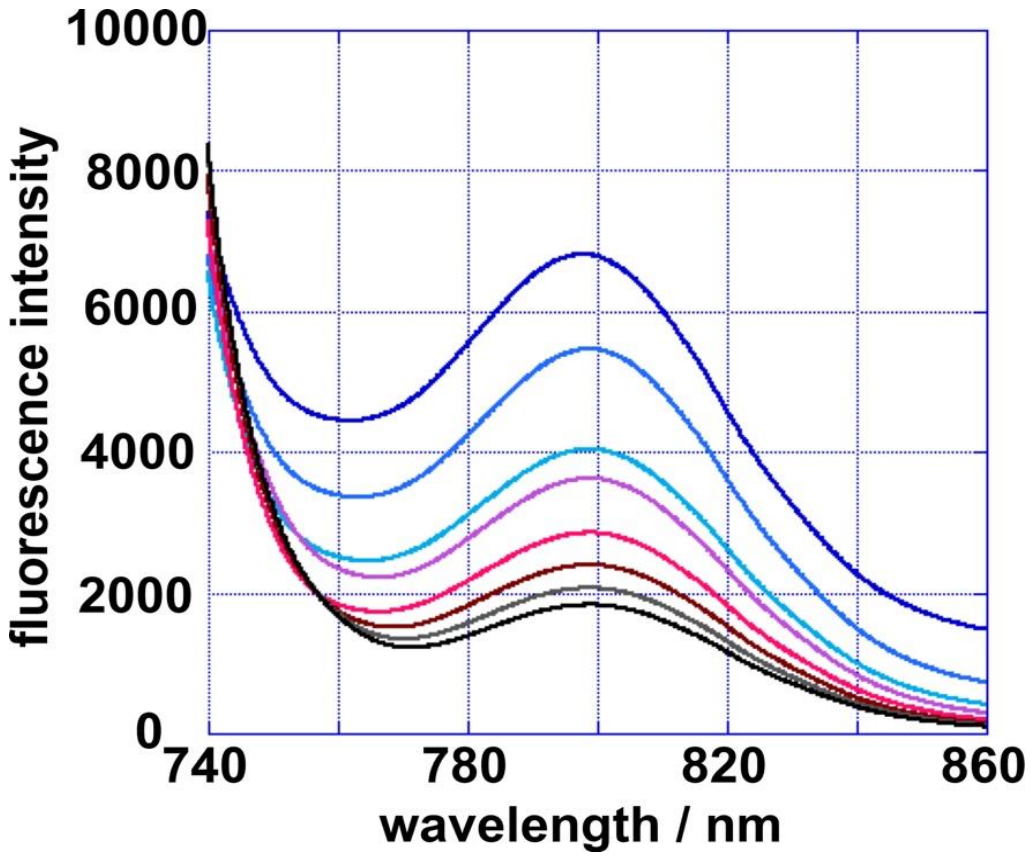

Figure 3.6: Steady-state fluorescence spectra of nanoplatform 1 (FRET pair cyanine 5.5 / cyanine 7.0) in PBS. Fluorescence spectra for the whole calibration (5.22 x 10^{-6} M to 5.22 x 10^{-13} M of arginase II in PBS, incubation at 37ºC for 1h). Dark blue line: 5.22 x 10^{-6} M or arginase II; blue line: 5.22 x 10^{-7} M; light blue line: 5.22 x 10^{-8} M; pink line: 5.22 x 10^{-9} M; red line: 5.22 x 10^{-10} M; brown line: 5.22 x 10^{-11} M, gray line: 5.22 x 10^{-12} M; black line: 5.22 x 10^{-13} M of arginase II in PBS.

Most interestingly, the observed FRET efficiency is strongest after 1h of incubation with the highest arginase II concentration and weakest in the absence of arginase. This finding is providing experimental evidence in favor of our paradigm: GO_7G possesses the higher mobility than GR_7G. Furthermore, complex formation between cyanine 7.0 and arginine is not observed.

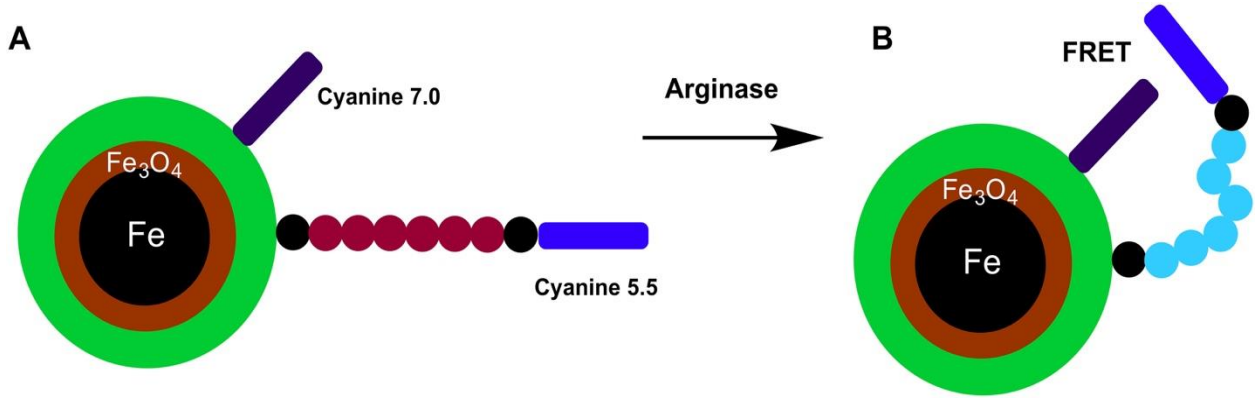

Scheme 3.3: Paradigm for the observed FRET efficiency as a function of arginase II concentration in nanoplatform 1. Black dots: glycine; brown dots: arginine, light blue dots: ornithine. A: FRET is inefficient before reaction of the tether with arginase II. B: FRET is strongest when virtually all arginine units have to be converted to ornithine.

The calibration curve for nanoplatform 1 is shown in Figure 3.7. Plotting the quotient of the integrated fluorescence bands of cyanine 5.5 (710 to 730nm) and cyanine 7.0 (760 to 840nm) vs. the decadic logarithm of arginase II concentration yielded the best (=most sensitive) results. Based on the experimental error of +/- 7 percent (rel.), the LOD of nanoplatform 1 under the experimental conditions described here is picomolar.

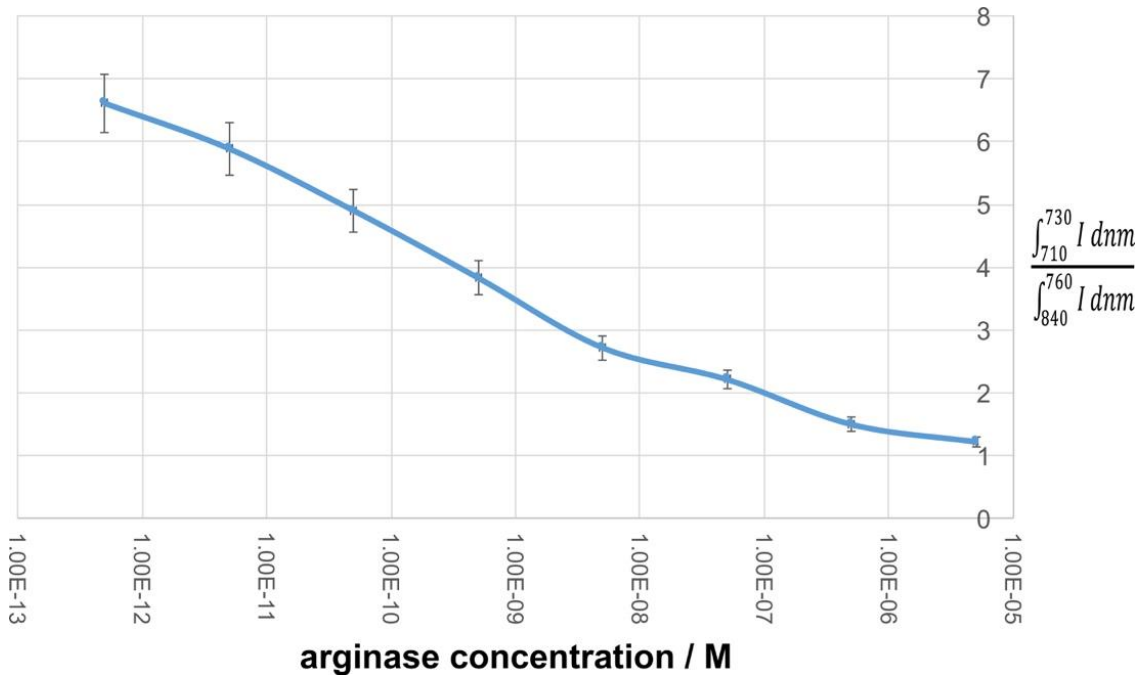

Figure 3.7: Calibration curve for nanoplatform 1 measuring arginase II (Sigma/Aldrich) activity in PBS. The plot shows the quotient of the integrated fluorescence bands of cyanine 5.5 (710 to 730nm) and cyanine 7.0 (760 to 840nm) as a function of log10 of arginase II concentration. The error from three repetitions was determined to 7% (rel.). Based on this error, the LOD (limit of detection) of nanoplatform 1 is picomolar.

Nanoplatform 2 (FRET pair cyanine 5.5 / cyanine 7.5) was tested/calibrated using the same protocols and procedures as described for nanoplatform 1. The only principal difference between the two nanoplatforms is that cyanine 7.5 is tethered to the dopamine coated Fe/Fe_3O_4 nanoparticles instead of cyanine 7.0. Although both nanoplatforms are very similar in their chemical composition, we cannot exclude minor differences in nanoparticle diameter, dopamine coating and tethering efficacy to fluorescent dyes and GR_7G. However, they should not account for the major differences in photophysical behavior between the two nanoplatforms.

The most striking difference between the photophysical behaviors of nanoplatforms 1 and 2 is that the latter does not show increased FRET efficiency with increased arginase II concentration and incubation time. For nanoplatform 2, a significant fluorescence increase over the whole observed fluorescence range is observed. This permits the calibration of nanoplatform 2. However, due to the absence of FRET, its LOD is only at 10^{-10} M of arginase II concentration, which is two orders of magnitude less than the LOD of nanoplatform 1.

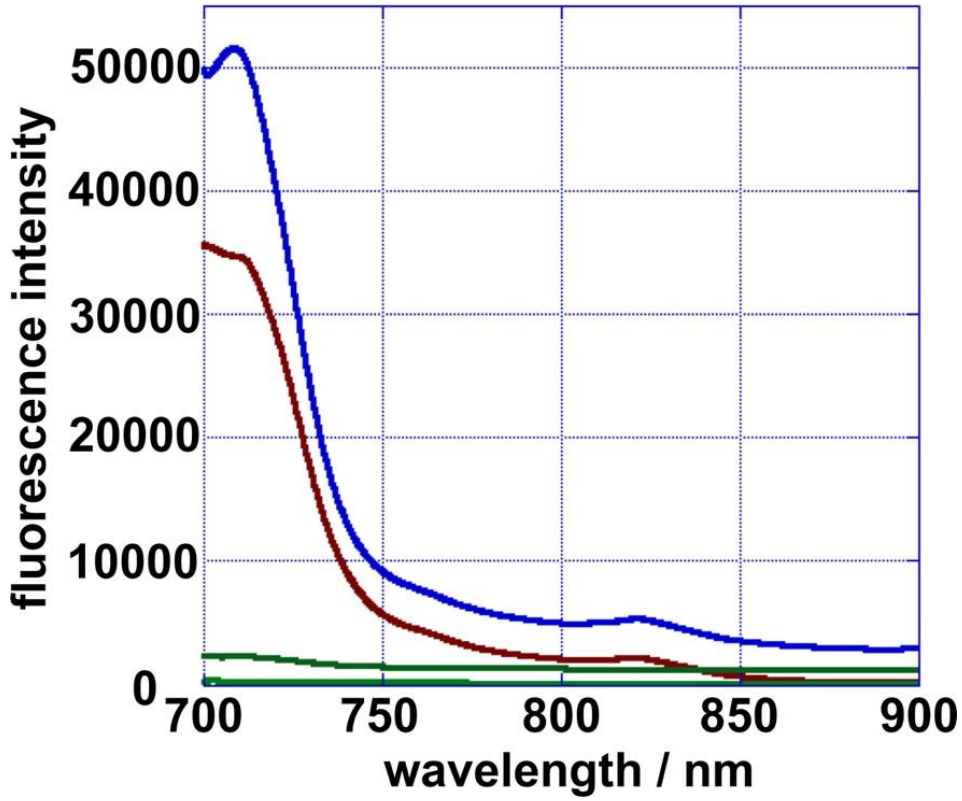

Figure 3.8: Steady-state fluorescence spectra of nanoplatform 2 (FRET pair cyanine 5.5 / cyanine 7.5) in PBS. Dark green line: PBS; light green line: 5.22 x 10^{-6} M arginase II in PBS; brown line: nanoplatform 2 in PBS in the absence of arginase after 1h of incubation at 37ºC; blue line: nanoplatform 2 in PBS after incubation with 5.22 x 10^{-6} M arginase II in PBS at 37ºC.

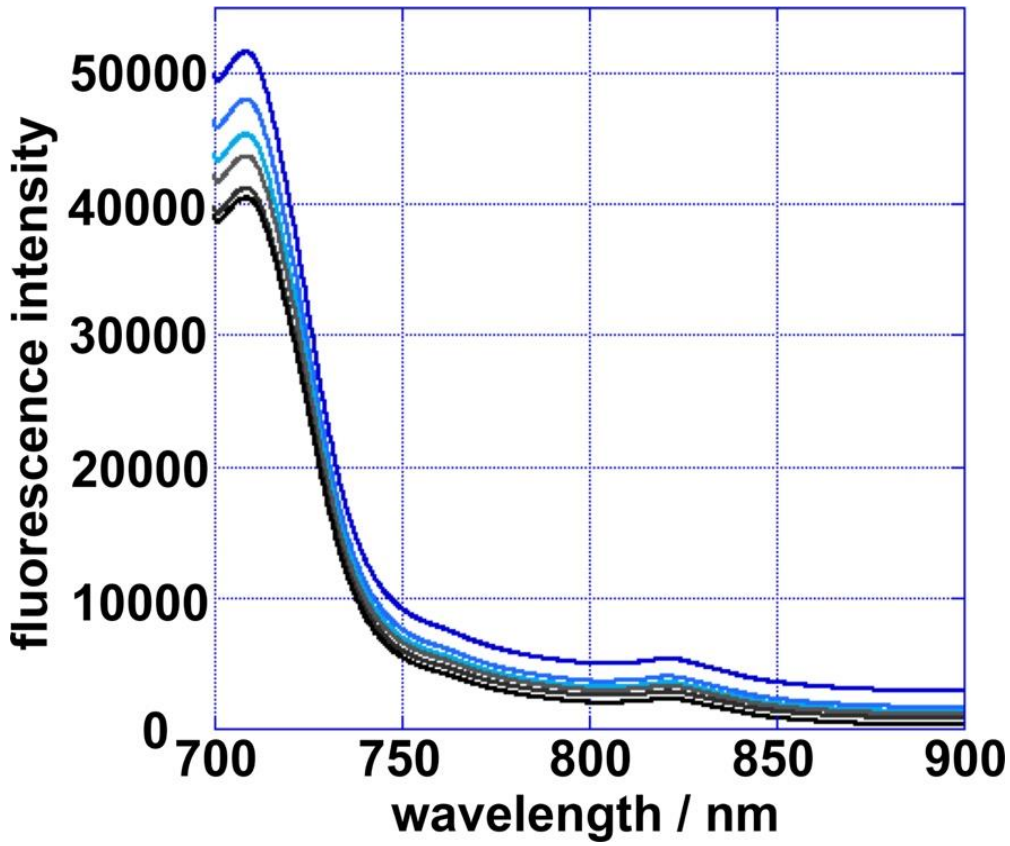

Figure 3.9: Steady-state fluorescence spectra of nanoplatform 2 (FRET pair cyanine 5.5 / cyanine 7.5) in PBS. Fluorescence spectra for the whole calibration (5.22 x 10^{-6} M to 5.22 x 10^{-13} M of arginase II in PBS, incubation at 37ºC for 1h). Dark blue line: 5.22 x 10^{-6} M or arginase II; blue line: 5.22 x 10^{-7} M; light blue line: 5.22 x 10^{-8} M; brown line: 5.22 x 10^{-9} M; gray line: 5.22 x 10^{-10} M; black line: 5.22 x 10^{-11} M of arginase II in PBS.

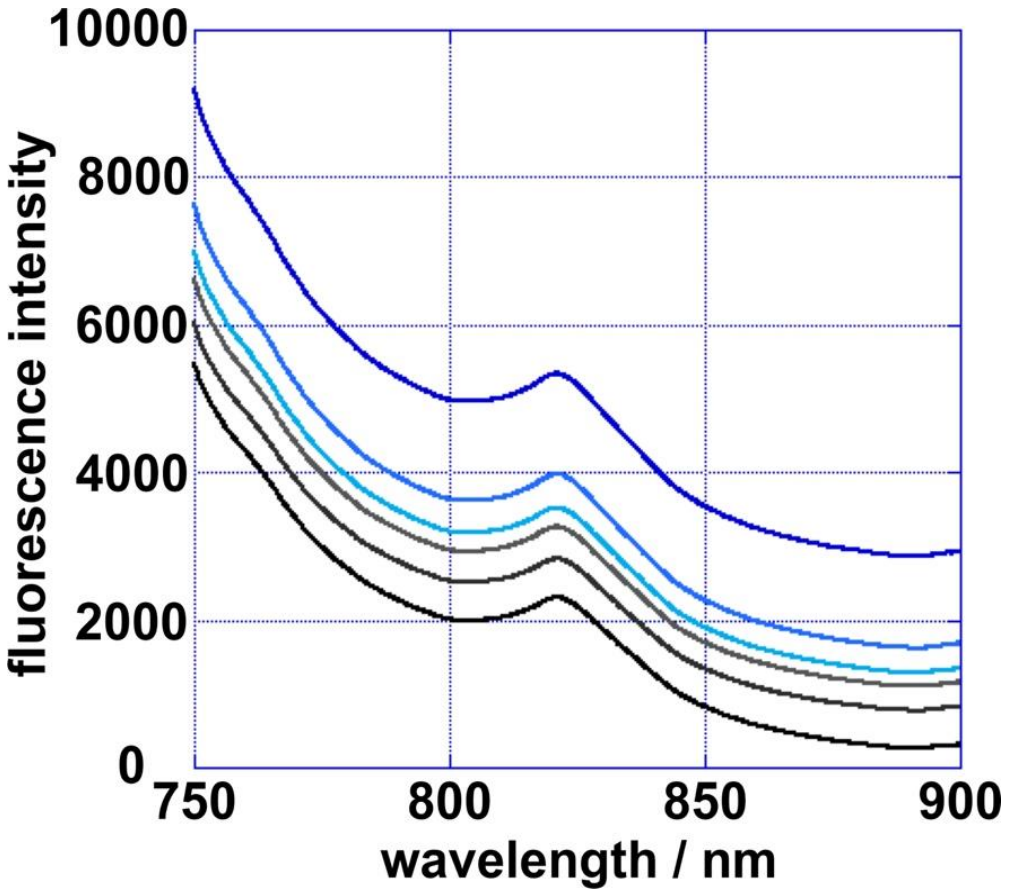

Figure 3.10: Steady-state fluorescence spectra of nanoplatform 2 (FRET pair cyanine 5.5 / cyanine 7.5) in PBS. Fluorescence spectra for the whole calibration (5.22 x 10^{-6} M to 5.22 x 10^{-13} M of arginase II in PBS, incubation at 37ºC for 1h). Dark blue line: 5.22 x 10^{-6} M or arginase II; blue line: 5.22 x 10^{-7} M; light blue line: 5.22 x 10^{-8} M; brown line: 5.22 x 10^{-9} M; gray line: 5.22 x 10^{-10} M; black line: 5.22 x 10^{-11} M of arginase II in PBS.

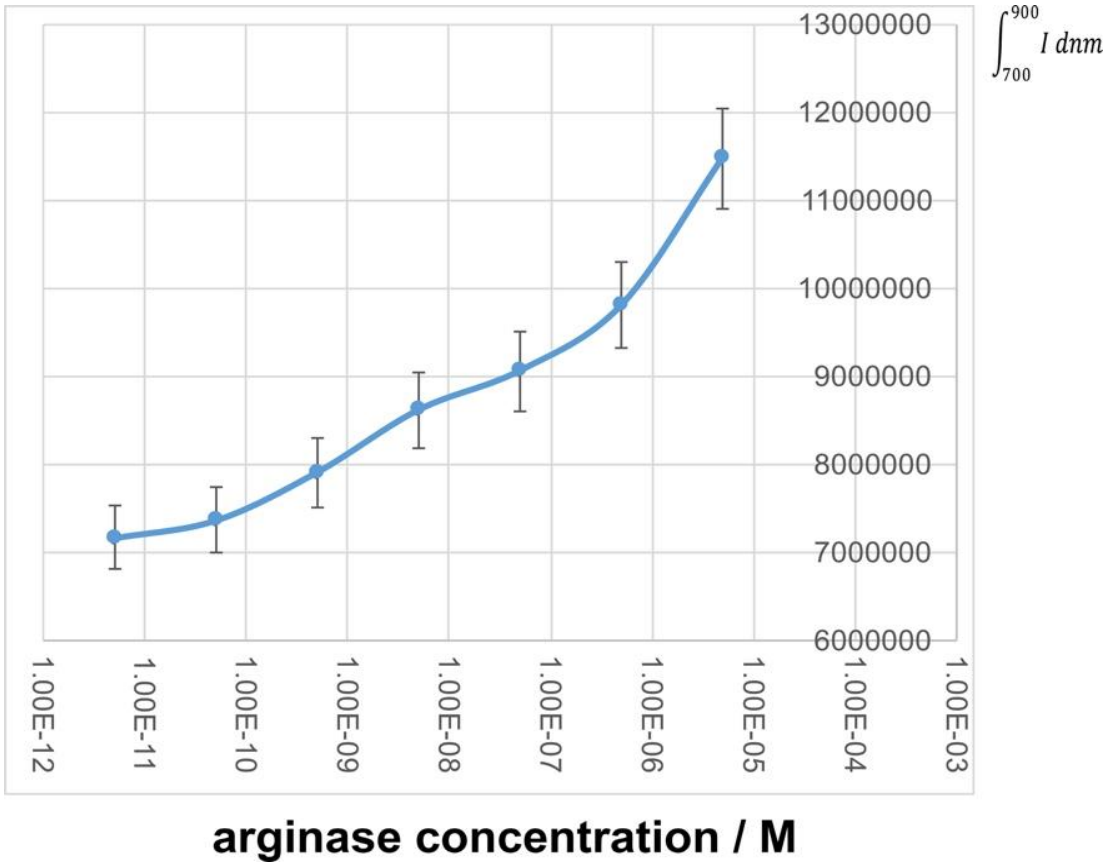

Figure 3.11: Calibration curve for nanoplatform 2 measuring arginase II (Sigma/Aldrich) activity in PBS. The plot shows the quotient of the integrated fluorescence bands of cyanine 5.5 and cyanine 7.5 over the complete fluorescence range (700 to 900nm) as a function of log10 of arginase II concentration. The error from three repetitions was determined to 5% (rel.). Based on this error, the LOD (limit of detection) of nanoplatform 2 is 10^{-10} M.

What could be the reason for the observed differences? According to reference 24, cyanine dyes form complexes with cationic aromatic compounds, which results in fluorescence quenching. Besides arginine, a fraction of the dopamine ligands at the Fe_3O_4 surface of the central nanoparticle is also quaternized in PBS. Both cyanine dyes are negatively charged in PBS, due to the deprotonation of their sulfonic acid group. The only chemical difference between

cyanine 7.0 and cyanine 7.5 is the existence of two additional fused benzene rings. Apparently, the presence of extended aromatic ring systems in cyanine 7.5 units favors their adsorption at the dopamine-coated interfaces. This enables more efficient fluorescence deactivation of cyanine 7.5 and, therefore, distinctly less fluorescence occurring from cyanine 7.5. However, this does not explain the observed fluorescence increase of nanoplatform 2 with increased arginase II concentration and incubation time. Therefore, we have to assume that complex formation between arginine and cyanine 7.5 occurs as well.

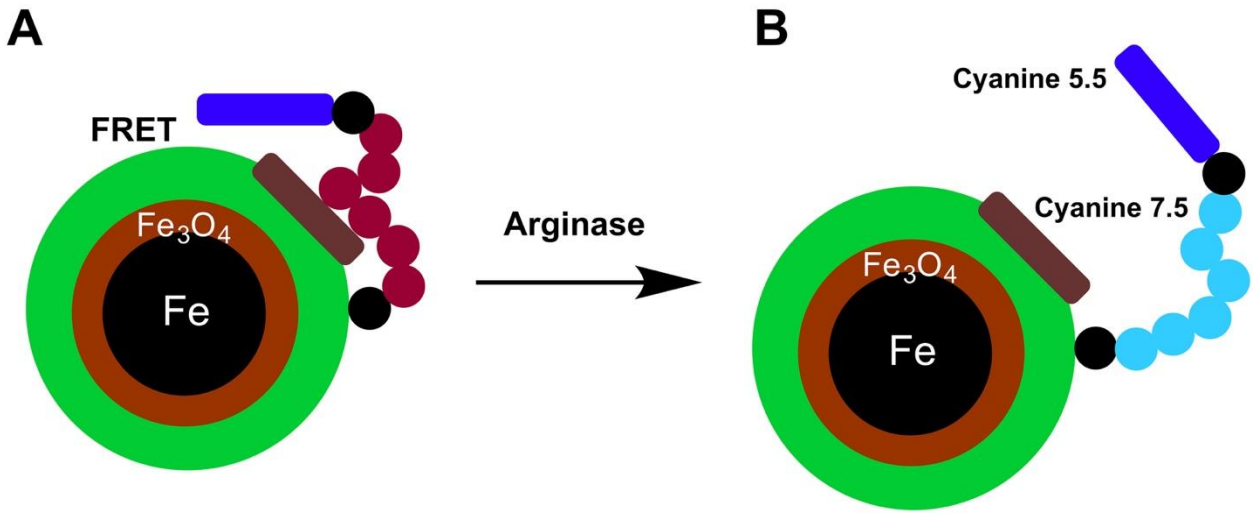

Scheme 3.4: Paradigm for the observed FRET efficiency as a function of arginase II concentration in nanoplatform 2. Black dots: glycine; brown dots: arginine, light blue dots: ornithine. A: FRET can occur between cyanine 5.5 and 7.5 before reaction with arginase II. However, complexation of both cyanines with quaternized arginine- and dopamine-units decreases their fluorescence quantum efficiencies. B: FRET between cyanine 5.5 and cyanine 7.5 does not occur after conversion of arginine to ornithine in the tether. However, the total fluorescence efficiency of both cyanine dyes increases due to reduced complex formation with quaternized organic bases.

3.3.2. Arginase II Concentration in Mouse Tissues

The tissue samples of BALB/c mice bearing 4T1 mammary tumors were obtained from Dr. Tej B. Shrestha in the group of Prof. Dr. Deryl L. Troyer, DMV, Department of Anatomy & Physiology at Kansas State University. The animal handling procedures are described in detail in reference [25]. The mouse tissue was harvested after the mice were euthanized 26d after tumor initiation in mammary fatpad #11. The mouse tissue was then homogenized following procedures that were previously established in collaboration with the group of Dr. Troyer, DVM [26]. All measurements of arginase II in tissue samples were performed using 2900 μL of PBS/Dextran, 30 μL of tissue extract and 70 μL of nanoplatform 1 dispersion in PBS/dextran. Assay controls were using 2970μL of PBS/Dextran and 30 μL of tissue extract. The solutions/dispersions were incubated for 60 min at 37^{o}C, followed by measuring their fluorescence spectra at 25^{o}C using a Fluoromax 2 device. The results are summarized in Figures 3.12 to 3.14 and Table 3.1.

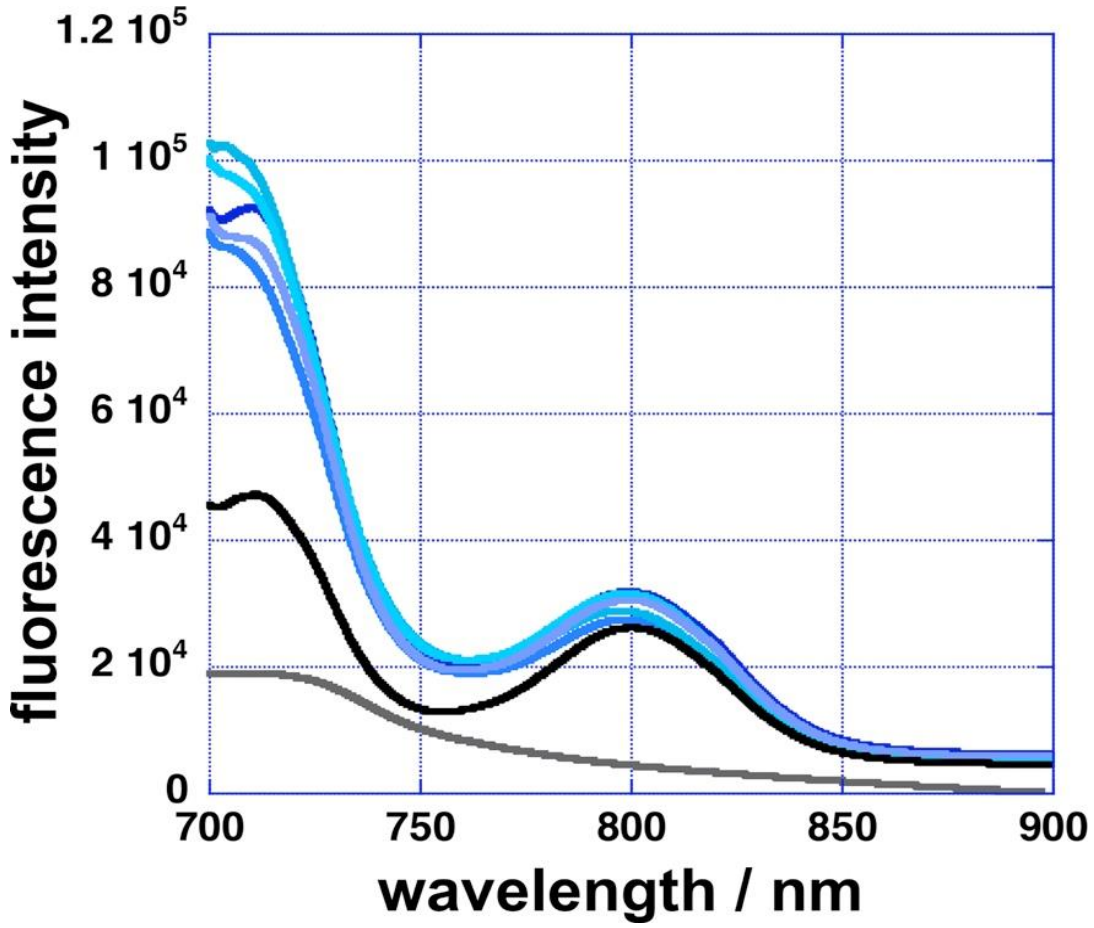

Figure 3.12: Steady-state fluorescence spectra of nanoplatform 1 (FRET pair cyanine 5.5 / cyanine 7.0) in PBS/Dextran (3.0 mL) in the presence of 30µL tissue extract from **core regions of murine 4T1 tumors**. Blue lines: nanoplatform 1 in the presence of tissue extract after 1h of incubation at 37ºC. Black line: nanoplatform 1 in PBS after 1h of incubation at 37ºC. Gray line: fluorescence of 30µL tissue extract from core regions of murine 4T1 tumors in PBS/Dextran (3.0 mL).

As summarized in Figure 3.12, all **five tumor core samples** obtained from BALB/c mice bearing **4T1 mammary tumors** show similar fluorescence behavior, which translated into similar arginase II concentrations. The exact concentrations were calculated using the calibration curve for nanoplatform 1 (Figure 3.7) and are summarized in Table 3.1. These measurements are making use of the "ratiometric principle" by monitoring two emission bands at the same time,

and then calculating the ratio between them [27]. The major advantage of ratiometric detection methods is that the measurement is becoming virtually independent of the influence of the exact nanoplatform concentration and the biological matrix on the fluorescence measurements.

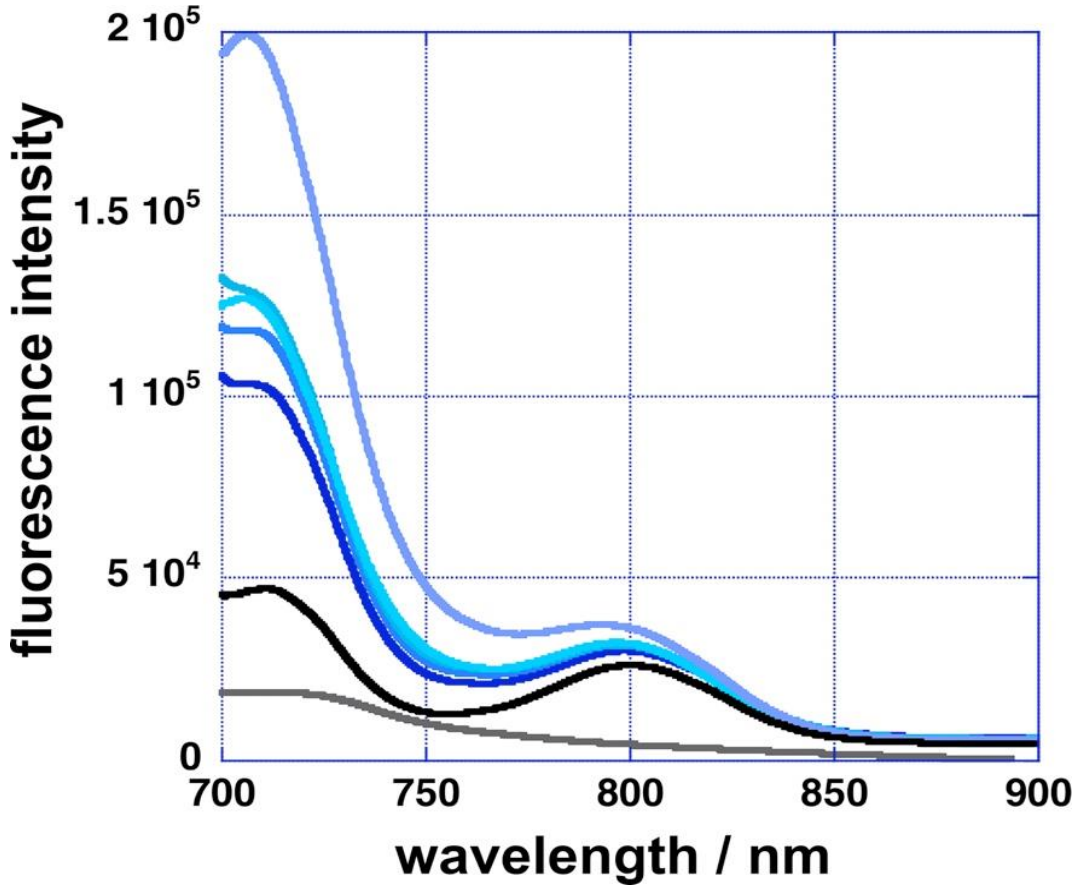

Figure 3.13: Steady-state fluorescence spectra of nanoplatform 1 (FRET pair cyanine 5.5 / cyanine 7.0) in PBS (3.0 mL) in the presence of 30μL tissue extract from **boundary regions of murine 4T1 tumors**. Blue lines: nanoplatform 1 in the presence of tissue extract after 1h of incubation at 37ºC. Black line: nanoplatform 1 in PBS after 1h of incubation at 37ºC. Gray line: fluorescence of 30μL tissue extract from boundary regions of murine 4T1 tumors.

It is noteworthy that four tissue samples from the **boundary regions of murine 4T1 tumors** result in similar photophysical behavior of nanoplatform 1, whereas one tissue sample was clearly different, resulting in a different fluorescence measurement. Since this is a syngeneic mouse model (possessing an intact immune system), it is very likely that one mouse developed a (weak) immune response to the tumor, resulting in a lower local arginase II activity. A comparison between the fluorescence spectra of tumor core samples and tumor boundary samples in Figures 3.12 and 3.13 clearly indicates that the intensity of the fluorescence spectra resulting from each tissue group are different. This may be caused by the presence of different proteins in tumor core and boundary regions. Nevertheless, the ratiometric principle is working well, permitting a direct comparison of the arginase II concentrations in both kinds of tissue (see Table 3.1).

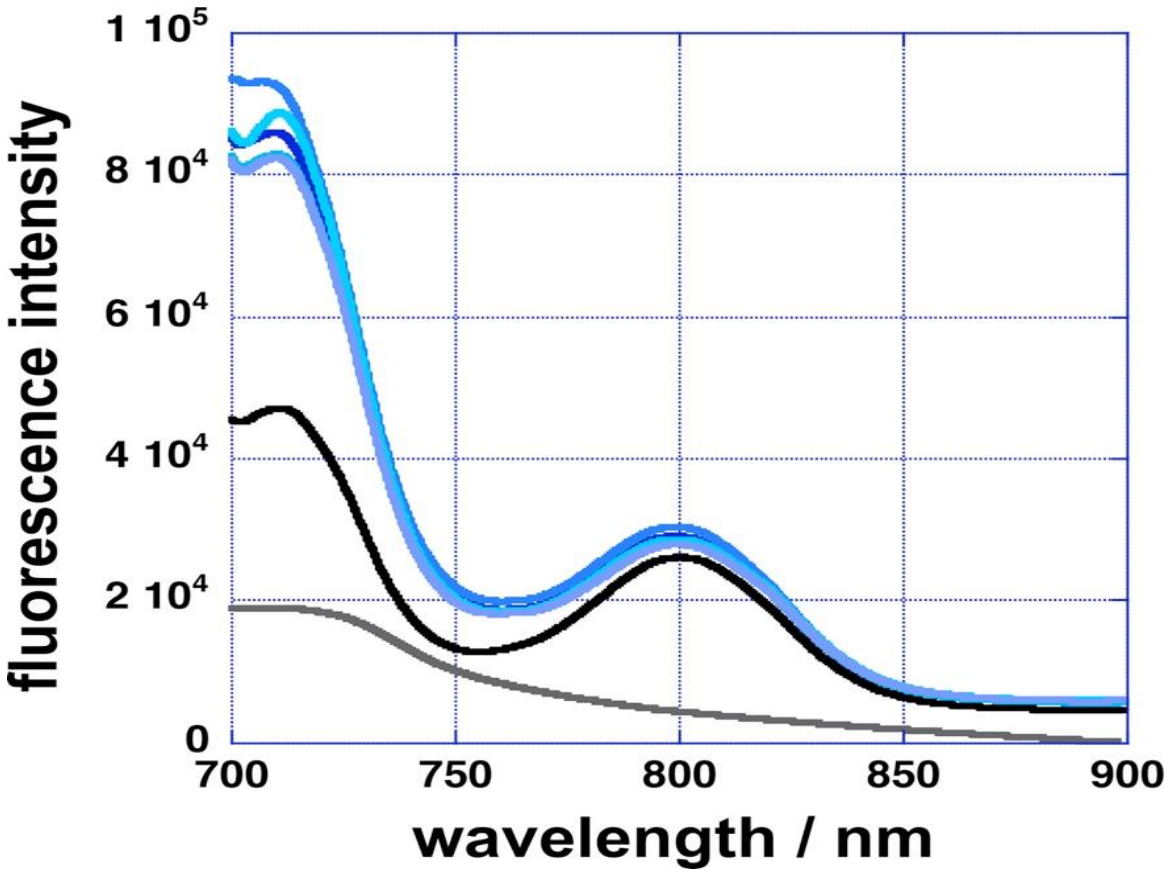

Figure 3.14: Steady-state fluorescence spectra of nanoplatform 1 (FRET pair cyanine 5.5 / cyanine 7.0) in PBS (3.0 mL) in the presence of 30µL tissue extract from **presumably non-cancerous regions of murine 4T1 tumors**. Blue lines: nanoplatform 1 in the presence of tissue extract after 1h of incubation at 37ºC. Black line: nanoplatform 1 in PBS after 1h of incubation at 37ºC. Gray line: fluorescence of 30µL tissue extract from presumably non-cancerous regions of murine 4T1 tumors.

Principally, the fluorescence occurring from nanoplatform 1 in the presence of nanoplatform 1 is similar as observed with tumor core and boundary tissue samples (Figures 3.12 and 3.13). However, differences in total fluorescence intensity can be discerned here as well. Again, the ratiometric principles permits the comparison of all findings shown in Figures 3.12 to 3.14.

Table 3.1: Calculated Arginase II Concentrations in Tissue Samples Collected from BALB/c Mice Bearing 4T1 Tumors in a Mammary Fatpad. Nanoplatform 1 was used to collect the fluorescence data, as described above.

Tissue	$\frac{\int_{710}^{730} I d\lambda}{\int_{760}^{840} I d\lambda}$	Arginase II Concentration / M
Tumor core 1	1.77	1.2×10^{-7}
Tumor core 2	1.78	1.1×10^{-7}
Tumor core 3	1.67	3.9×10^{-7}
Tumor core 4	1.74	1.8×10^{-7}
Tumor core 5	1.73	2.1×10^{-7}
Tumor boundary 1	1.15	$7.1 \times 10^{-6*}$
Tumor boundary 2	1.19	5.1×10^{-6}
Tumor boundary 3	1.16	$7.0 \times 10^{-6*}$
Tumor boundary 4	1.15	$7.1 \times 10^{-6*}$
Tumor boundary 5	1.38	9.8×10^{-7}
Presumably healthy tissue from tumor mouse 1	1.68	3.8×10^{-7}
Presumably healthy tissue from tumor mouse 2	1.74	1.8×10^{-7}
Presumably healthy tissue from tumor mouse 3	1.61	4.8×10^{-7}
Presumably healthy tissue from tumor mouse 4	1.65	4.1×10^{-7}
Presumably healthy tissue from tumor mouse 5	1.73	2.1×10^{-7}

3.4. Conclusions

Nanoplatforms for arginase detecting were developed, comprised of a central, dopamine-covered Fe/Fe_3O_4 nanoparticle and the FRET pairs cyanine 5.5 / 7.0 (nanoplatform 1) and cyanine 5.5 / 7.5 (nanoplatform 2). Cyanine 5.5 was tethered to the central nanoparticle via the oligopeptide GR_7G. Cyanine 7.0 was linked directly to the central inorganic nanoparticle. Nanoplatform 1 performed superior, permitting arginase II detection down to picomolar levels, while providing a very wide range of measurement from 5×10^{-6} to 10^{-12} M.

We have utilized nanoplatform 1 for the determination of arginase II levels in tissue extracts from 4T1 tumor bearing white mice with exact immune system. Most interestingly, the arginase II concentration in the boundary region between tumor and presumably healthy tissue is on average 3.5 times higher than in the tumor core region, and 2.2 times higher than in presumably healthy tissue. From this data, two potentially important conclusions can be drawn: 1) The immune suppression is highest in the cancer boundary regions. This is of importance for novel approaches to immunotherapy, which have to target the boundary region to be successful. 2) There is a systemic immunodepression effect in cancer, which influences the biochemistry of the whole organism. Although immunodepression is strongest in the boundary region, it is by no means limited to that region.

3.5. Methods

Cyanine 5.5 and dopamine coated core/ shell iron/ iron oxide nanoparticles were synthesized following the same procedure as explained in chapter 2.

3.5.1. Cyanine 7.0 synthesis

3.5.1(A) Synthesis of 4-(2,3,3-trimethyl-3H-indol-1-ium-1-yl)butane-1-sulfonate

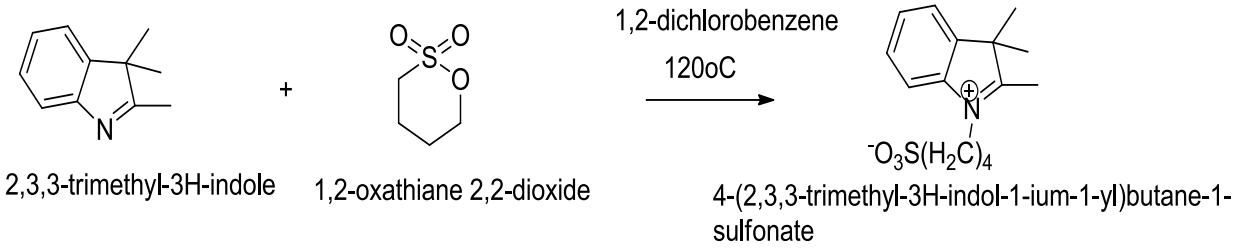

Figure 3.15: Reaction scheme for Synthesis of 4-(2,3,3-trimethyl-3H-indol-1-ium-1-yl)butane-1-sulfonate

6.37g 2,3,3-trimethyl-3H-indole and 10.89 g 1,2-oxathiane 2,2-dioxide(1/2 ratio) were dissolved in 30 mL of 1,2-dichlorobenzene, the reaction mixture was stirred at 120 ^{o}C under Argon for 12 hours. After cooling to room temperature, product was collected via vacuum filtration, and followed by washing with ether (3 ×10 mL). 5.91g 4-(2,3,3-trimethyl-3H-indol-1-ium-1-yl)butane-1-sulfonate was obtained as product [22,29].

3.5.1(B) Synthesis of (E)-2-chloro-3-(hydroxymethylene)cyclohex-1-enecarbaldehyde

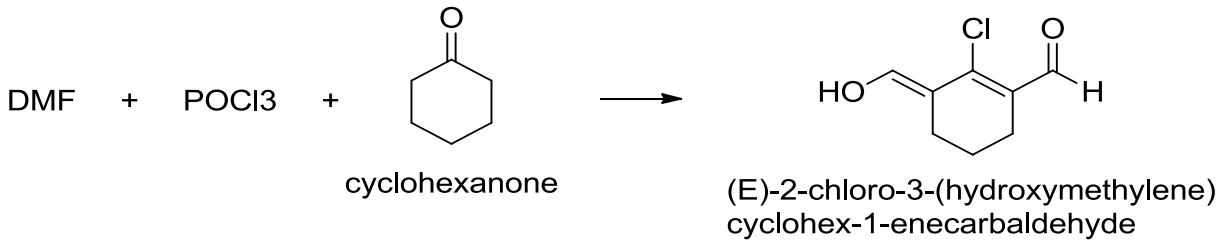

Figure 3.16: Reaction scheme for Synthesis of (E)-2-chloro-3-(hydroxymethylene)cyclohex-1-enecarbaldehyde

A solution of 40 mL DMF in 40 mL of CH_2Cl_2 was chilled in a ice bath, and 37 mL of $POCl_3$ in 35 mL of CH_2Cl_2 was added dropwise with stirring. Upon the completion of addition, 10 g of cyclohexanone was added via a syringe. The formed solution was refluxed at 60 ^oC for 3 hours. After cooling to room temperature, the solution was poured onto 200g crushed ice, and allowed to stand overnight. The yellow solid was collected by vacuum filtration, and further recrystallized in acetone [22,29]. 36% yield.

3.5.1(C) Synthesis of sodium 4-((E)-2-((E)-2-(2-chloro-3-((E)-2-(3,3-dimethyl-1-(4-sulfonatobutyl)-3H-indol-1-ium-2-yl)vinyl)cyclohex-2-en-1-ylidene)ethylidene)-3,3-dimethylindolin-1-yl)butane-1-sulfonate (cyanine 7.0)

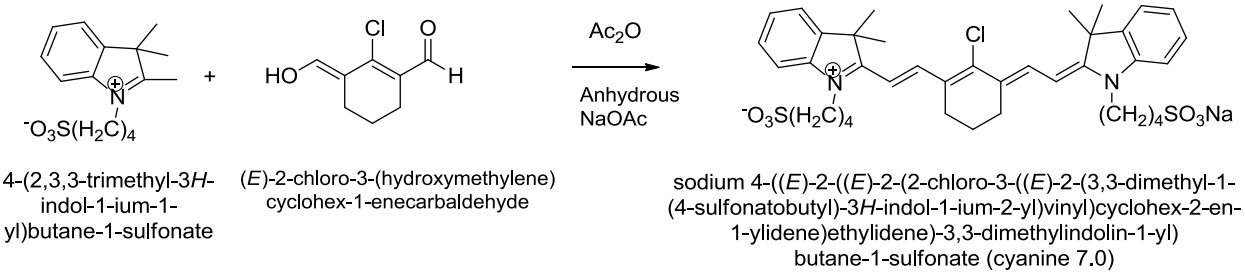

Figure 3.17: Reaction scheme for Synthesis of sodium 4-((E)-2-((E)-2-(2-chloro-3-((E)-2-(3,3-dimethyl-1-(4-sulfonatobutyl)-3H-indol-1-ium-2-yl)vinyl)cyclohex-2-en-1-ylidene)ethylidene)-3,3-dimethylindolin-1-yl)butane-1-sulfonate (cyanine 7.0)

0.5 g compound 4-(2,3,3-trimethyl-3H-indol-1-ium-1-yl)butane-1-sulfonate, 0.122 g compound (E)-2-chloro-3-(hydroxymethylene)cyclohex-1-enecarbaldehyde and 0.12 g NaOAc were heated in 13 mL of acetic anhydride at 70 ^oC for 40 min. After cooling to room temperature, the green solution was poured into 15 mL saturated lithium bromide water solution. The mixture was stirred at room temperature for 30 min. 30 mL of methylene chloride was added

to extract the product. The organic phase was washed with water (10 ×10 mL), and then dried over anhydrous $MgSO_4$. After evaporation of solvent, the product was purified by column chromatography (Silica gel, eluted with ethyl acetate/ethanol 3/1 to 1/1 then CH_2Cl_2/ethanol/acetic acid 1/1/0.05) [22, 29]. 56% yield.

3.5.2. Synthesis of sodium 4-((E)-2-((E)-2-(2-((2-carboxyethyl)thio)-3-((E)-2-(3,3-dimethyl-1-(4-sulfonatobutyl)-3H-indol-1-ium-2-yl)vinyl)cyclohex-2-en-1-ylidene)ethylidene)-3,3-dimethylindolin-1-yl)butane-1-sulfonate

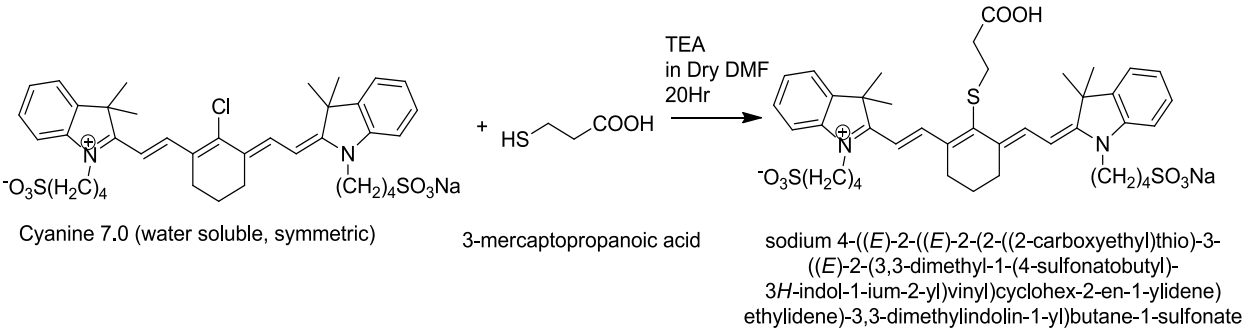

Figure 3.18: Reaction scheme for Synthesis of sodium 4-((E)-2-((E)-2-(2-((2-carboxyethyl)thio)-3-((E)-2-(3,3-dimethyl-1-(4-sulfonatobutyl)-3H-indol-1-ium-2-yl)vinyl)cyclohex-2-en-1-ylidene)ethylidene)-3,3-dimethylindolin-1-yl)butane-1-sulfonate.

300mg of cyanine 7.0 (water soluble, symmetric), 52µL of 3-mercaptopropylacid (1.5 equivalent) and 90µL of triethylamine (1.5 equivalent) were mixed in 2mL of dry DMF and stirred at room temperature for 20 hours under dark conditions. 10ml of ice cold ether was added dropwise to the reaction mixture, to precipitate out the product. Precipitated product was separated and dried under high vacuum [22,29].

3.5.3. Cyanine 7.5 (water soluble) synthesis

3.5.3(A) Synthesis of 4-(1,1,2-trimethyl-1H-benzo[e]indol-3-ium-3-yl)butane-1-sulfonate

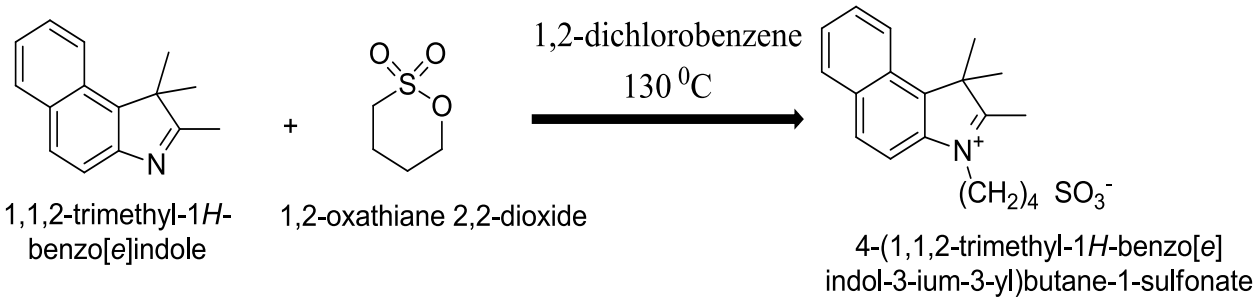

Figure 3.19: Reaction scheme for Synthesis of 4-(1,1,2-trimethyl-1H-benzo[e]indol-3-ium-3-yl)butane-1-sulfonate

A 50 mL two necked round bottom flask fitted with a magnetic stirrer and a condenser was flame dried. 1,1,2-trimethyl-1H-benzo[e]indole (1.0g, 4.78mmol) was dissolved in dry o-dichlorobenzene (10 mL). 1,4-butanesultone (0.58mL, 5.73mmol) was added drop-wise under a continuous flow of argon. The reaction mixture was, then, allowed to heat up to 130^0 C for 24h. The reaction mixture was allowed to cool down to room temperature to obtain a blue colored precipitate. The precipitate was triturated with ice-cold diethyl ether (40mL) for 15min. The precipitate was filtered through frit glass, washed with cold diethyl ether (3 x 5mL), dried in vacuum yielding 4-(1,1,2-trimethyl-1H-benzo[e]indol-3-ium-3-yl)butane-1-sulfonate [22,29].

3.5.3(B) Synthesis of Cyanine 7.5 (water soluble, symmetric), sodium 4-(2-((E)-2-((E)-2-chloro-3-((E)-2-(1,1-dimethyl-3-(4-sulfonatobutyl)-1H-benzo[e]indol-2(3H)-ylidene)ethylidene)cyclohex-1-en-1-yl)vinyl)-1,1-dimethyl-1H-benzo[e]indol-3-ium-3-yl)

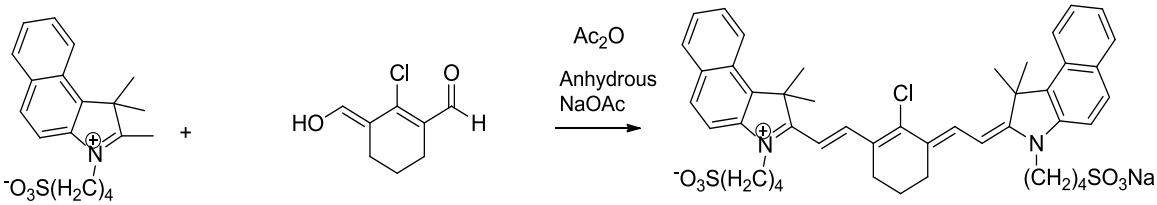

4-(1,1,2-trimethyl-1*H*-benzo[*e*] indol-3-ium-3-yl)butane-1-sulfonate

(*E*)-2-chloro-3-(hydroxymethylene) cyclohex-1-enecarbaldehyde

sodium 4-(2-((*E*)-2-((*E*)-2-chloro-3-((*E*)-2-(1,1-dimethyl-3-(4-sulfonatobutyl)-1*H*-benzo[*e*]indol-2(3*H*)-ylidene)ethylidene)cyclohex-1-en-1-yl) vinyl)-1,1-dimethyl-1*H*-benzo[*e*]indol-3-ium-3-yl) butane-1-sulfonate

Figure 3.20: Reaction scheme for Synthesis of sodium 4-(2-((E)-2-((E)-2-chloro-3-((E)-2-(1,1-dimethyl-3-(4-sulfonatobutyl)-1H-benzo[e]indol-2(3H)-ylidene)ethylidene)cyclohex-1-en-1-yl)vinyl)-1,1-dimethyl-1H-benzo[e]indol-3-ium-3-yl)

0.58g compound 4-(1,1,2-trimethyl-1H-benzo[e]indol-3-ium-3-yl)butane-1-sulfonate, 0.122 g compound (E)-2-chloro-3-(hydroxymethylene)cyclohex-1-enecarbaldehyde and 0.12 g NaOAc were heated in 13 mL of acetic anhydride at 70 ^{o}C for 40 min. After cooling to room temperature, the green solution was poured into 15 mL saturated lithium bromide water solution. The mixture was stirred at room temperature for 30 min. 30 mL of methylene chloride was added to extract the product. The organic phase was washed with water (10 ×10 mL), and then dried over anhydrous $MgSO_4$. After evaporation of solvent, the product was purified by column chromatography (Silica gel, eluted with ethyl acetate/ethanol 3/1 to 1/1 then CH_2Cl_2/ethanol/acetic acid 1/1/0.05) [22,29]. 54% yield.

3.5.4. Synthesis of sodium 4-(2-((E)-2-((E)-2-((2-carboxyethyl)thio)-3-((E)-2-(1,1-dimethyl-3-(4-sulfonatobutyl)-1H-benzo[e]indol-2(3H)-ylidene)ethylidene)cyclohex-1-en-1-yl)vinyl)-1,1-dimethyl-1H-benzo[e]indol-3-ium-3-yl)butane-1-sulfonate

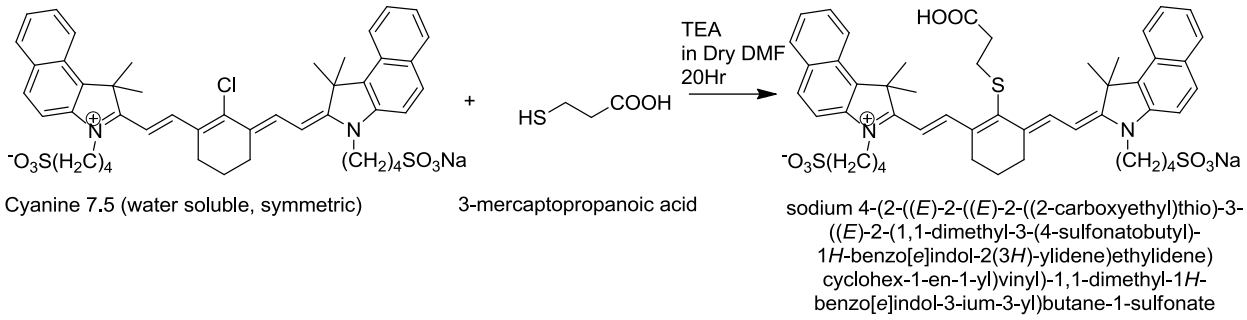

Figure 3.21: Reaction scheme for Synthesis of sodium 4-(2-((E)-2-((E)-2-((2-carboxyethyl)thio)-3-((E)-2-(1,1-dimethyl-3-(4-sulfonatobutyl)-1H-benzo[e]indol-2(3H) ylidene)ethylidene)cyclohex-1-en-1-yl)vinyl)-1,1-dimethyl-1H-benzo[e]indol-3-ium-3-yl)butane-1-sulfonate

250mg of cyanine 7.5 (water soluble, symmetric), 39µL of 3-mercaptopropylacid (1.5 equivalent) and 62µL of triethylamine (1.5 equivalent) were mixed in 2mL of dry DMF and stirred at room temperature for 20 hours under dark conditions. 10mL of ice cold ether was added dropwise to the reaction mixture, to precipitate out the product. Precipitated product was separated and dried under high vacuum [22,29].

3.5.5. Synthesis of GR_7G and GO_7G oligopeptide sequences

The GR_7G and $G0_7G$ consensus sequence were synthesized by standard solid phase peptide synthesis. Trityl-resin was used as a matrix polymer solid support. Peptide synthesis was completed in the same peptide synthesis tube by the repetitive steps in addition of specific amino acid, filtration and washings, accordingly. Commercially available N-terminal protected C-terminal amino acids are used for the synthesis [28].

The resin was preloaded into the peptide synthesis tube and swelled in dichloromethane (DCM) for 20 minutes and then filtered. DCM was washed away by five consecutive of N,N-Dimethylformamide (DMF) washings. A mixture of Fmoc protected amino acid and O-Benzotriazole-N,N,N',N'tetramethyl-uronium-hexafluoro-phosphate (HBTU) as coupling agent were added, swirled 30 minutes, and then filtered. This step was repeated once. Excess amino acid and the coupling agent were washed away by five DMF washings. Then 20% piperidine in DMF was used for N-deprotection. Subsequent amino acid coupling was performed after N-deprotection. Both GR_7G and $G0_7G$ consensus sequences were synthesized using amino acid by amino acid from C-terminus to N-terminus [28].

3.5.6. Coupling of Cyanine 5.5 to the GR_7G Oligopeptide Sequence

Cyanine 5.5 was coupled to the N-terminal on the GR_7G sequence following same coupling conditions as for an amino acid.

Finally, the cyanine 5.5 conjugated GR_7G consensus sequence was cleaved from the resin and also the side chain protecting groups were removed using a mixture of TFA, TIPS and water (95: 2.5 : 2.5). Cy5.5-GR_7G was precipitated in cold ether and collected by centrifuging at 10000rpm. After precipitation, several DMF washings were carried out to remove the excess of unreacted cyanine 5.5 and other reagents. Three final ether washings were carried out, in order to remove leftover DMF.

3.5.7. Coupling of Cyanine 5.5 to the GO_7G Oligopeptide Sequence

Cyanine 5.5 was coupled to the N-terminal on the GO_7G sequence following same coupling conditions as for an amino acid.

Finally, the cyanine 5.5 conjugated GO_7G consensus sequence was cleaved from the resin and also the side chain protecting groups were removed using a mixture of TFA, TIPS and water (95: 2.5 : 2.5). Cy5.5-GO_7G was precipitated in cold ether and collected by centrifuging at 10000 rpm. After precipitation, several DMF washings were carried out to remove the excess of unreacted cyanine5.5 and other reagents. Three final ether washings were carried out, in order to remove leftover DMF.

3.5.8. Sensor 1 development

The published synthesis procedure (from Wang et al. (2014), is reproduced here.

125 mg of dopamine coated Fe/Fe_3O_4 nanoparticles were dispersed in 2 mL of DMF. A solution of 3mmol of sodium 4-((E)-2-((E)-2-(2-((2-carboxyethyl)thio)-3-((E)-2-(3,3-dimethyl-1-(4-sulfonatobutyl)-3H-indol-1-ium-2-yl)vinyl)cyclohex-2-en-1-ylidene)ethylidene)-3,3-dimethylindolin-1-yl)butane-1-sulfonate (cyanine 7.0), 3.2 mmol of EDC, 1.7 mmol of DMAP in 1 mL of DMF was added to this dispersion. After sonicating for 1 h, the nanoparticles were precipitated by centrifugation (10,000 RPM for 20 min), and thoroughly washed with DMF (1 mL × 10). The recovered nanoparticles were redispersed in 2 mL of DMF, and to this dispersion, 2.6 mmol of Cyanine 5.5 linked GR7G peptide sequence, 3 mmol of EDC, 2.6 mmol of DMAP in 1 mL of DMF was added. After sonicating for 1 h, the nanoparticles were precipitated by a magnet (0.55T), and thoroughly washed with DMF (1mL × 10). After drying in high vacuum, 90-100 mg of nanoplatform was obtained.

3.5.9. Sensor 2 development

The published synthesis procedure (from Wang et al. (2014), is reproduced here.

125 mg of dopamine coated Fe/Fe_3O_4 nanoparticles were dispersed in 2 mL of DMF. A solution of 3mmol of sodium 4-(2-((E)-2-((E)-2-((2-carboxyethyl)thio)-3-((E)-2-(1,1-dimethyl-3-(4-sulfonatobutyl)-1H-benzo[e]indol-2(3H)-ylidene)ethylidene)cyclohex-1-en-1-yl)vinyl)-1,1-dimethyl-1H-benzo[e]indol-3-ium-3-yl)butane-1-sulfonate (Cyanine 7.5), 3.2 mmol of EDC, 1.7 mmol of DMAP in 1 mL of DMF was added to this dispersion. After sonicating for 1 h, the nanoparticles were precipitated by centrifugation (10,000 RPM for 20 min), and thoroughly washed with DMF (1 mL × 10). The recovered nanoparticles were redispersed in 2 mL of DMF, and to this dispersion, 2.6mmol of Cyanine 5.5 linked GR7G peptide sequence, 3mmol of EDC, 2.6 mmol of DMAP in 1 mL of DMF was added. After sonicating for 1 h, the nanoparticles were precipitated by a magnet (0.55T), and thoroughly washed with DMF (1mL × 10). After drying in high vacuum, 90-100 mg of nanoplatform was obtained.

References

1. Caldwell, R. B.; Toque, H. A.; Narayanan, S. P.; Caldwell, R. W., Arginase: an old enzyme with new tricks. *Trends Pharmacol. Sci.* **2015,***36* (6), 395-405.
2. Munder, M., Arginase: an emerging key player in the mammalian immune system. *Br J Pharmacol* **2009,***158* (3), 638-51.
3. Lamas, B.; Vergnaud-Gauduchon, J.; Goncalves-Mendes, N.; Perche, O.; Rossary, A.; Vasson, M. P.; Farges, M. C., Altered functions of natural killer cells in response to L-Arginine availability. *Cell Immunol* **2012,***280* (2), 182-90.
4. Di Costanzo, L.; Sabio, G.; Mora, A.; Rodriguez, P. C.; Ochoa, A. C.; Centeno, F.; Christianson, D. W., Crystal structure of human arginase I at 1.29-A resolution and exploration of inhibition in the immune response. *Proc Natl Acad Sci U S A* **2005,***102* (37), 13058-63.
5. Das, P.; Lahiri, A.; Lahiri, A.; Chakravortty, D., Modulation of the arginase pathway in the context of microbial pathogenesis: a metabolic enzyme moonlighting as an immune modulator. *PLoS Pathog* **2010,***6* (6), e1000899.
6. Fatima, N.; Cohen, C.; Siddiqui, M. T., Arginase-1: A Highly Specific Marker Separating Pancreatic Adenocarcinoma from Hepatocellular Carcinoma. *Acta Cytol.* **2014,***58* (1), 83-88.
7. Ino, Y.; Yamazaki-Itoh, R.; Oguro, S.; Shimada, K.; Kosuge, T.; Zavada, J.; Kanai, Y.; Hiraoka, N., Arginase II expressed in cancer-associated fibroblasts indicates tissue hypoxia and predicts poor outcome in patients with pancreatic cancer. *PLoS One* **2013,***8* (2), e55146.
8. Malalasekera, A.P.; Wang, H.; Wendel, S. O.; Zhu, G.; Troyer, D. L.; US 62/135366: Nanoplatforms for Arginase, Indoleamine 2,3-dioxygenase and Tryptophan 2,3-

dioxygenase Detection by Means of Posttranslational Modification.

9. http://www.biovision.com/arginase-activity-colorimetric-assay-kit-7400.html
10. Liang, J.; Liu, H.; Huang, C.; Yao, C.; Fu, Q.; Li, X.; Cao, D.; Luo, Z.; Tang, Y., Aggregated Silver Nanoparticles Based Surface-Enhanced Raman Scattering Enzyme-Linked Immunosorbent Assay for Ultrasensitive Detection of Protein Biomarkers and Small Molecules. *Anal. Chem.* **2015,***87* (11), 5790-5796.
11. Cama, E.; Colleluori, D. M.; Emig, F. A.; Shin, H.; Kim, S. W.; Kim, N. N.; Traish, A. M.; Ash, D. E.; Christianson, D. W., Human arginase II: crystal structure and physiological role in male and female sexual arousal. *Biochemistry* **2003,***42* (28), 8445-51.
12. http://web.expasy.org/cgi-bin/compute_pi/pi_tool
13. Selvin, P. R., The renaissance of fluorescence resonance energy transfer. *Nat. Struct. Biol.* **2000,***7* (9), 730-734.
14. Patsenker, L.; Tatarets, A.; Kolosova, O.; Obukhova, O.; Povrozin, Y.; Fedyunyayeva, I.; Yermolenko, I.; Terpetschnig, E., Fluorescent probes and labels for biomedical applications. *Ann. N. Y. Acad. Sci.* **2008,***1130* (Fluorescence Methods and Applications), 179-187.
15. Lee, H.; Berezin, M. Y.; Henary, M.; Strekowski, L.; Achilefu, S., Fluorescence lifetime properties of near-infrared cyanine dyes in relation to their structures. *J. Photochem. Photobiol., A* **2008,***200* (2-3), 438-444.
16. James, N. S.; Chen, Y.; Joshi, P.; Ohulchanskyy, T. Y.; Ethirajan, M.; Henary, M.; Strekowski, L.; Pandey, R. K., Evaluation of polymethine dyes as potential probes for near infrared fluorescence imaging of tumors: part - 1. *Theranostics* **2013,***3* (9), 692-702,

11 pp.

17. Lacroix LM, Huls NF, Ho D, Sun X, Cheng K, Sun S. Stable single-crystalline body centered cubic Fe nanoparticles. Nano Lett. 2011;11:1641-5.
18. Schweigert, N.; Zehnder, A. J. B.; Eggen, R. I. L., Chemical properties of catechols and their molecular modes of toxic action in cells, from microorganisms to mammals. *Environ. Microbiol.* **2001,***3* (2), 81-91.
19. Xu C, Xu K, Gu H, Zheng R, Liu H, Zhang X, Guo Z, Xu B. Dopamine as a robust anchor to immobilize functional molecules on the iron oxide shell of magnetic nanoparticles. J Am Chem Soc. 2004;126:9938-9.
20. Jennings, T. L.; Singh, M. P.; Strouse, G. F. *J. Am. Chem. Soc.* **2006,***128* (16), 5462-5467.
21. Wang, H.; Shrestha, T. B.; Basel, M. T.; Dani, R. K.; Seo, G.-M.; Balivada, S.; Pyle, M. M.; Prock, H.; Koper, O. B.; Thapa, P. S.; Moore, D.; Li, P.; Chikan, V.; Troyer, D. L.; Bossmann, S. H., Magnetic-Fe/Fe3O4-nanoparticle-bound SN38 as carboxylesterase-cleavable prodrug for the delivery to tumors within monocytes/macrophages. *Beilstein J. Nanotechnol.* **2012,***3*, 444-455, 12 pp.
22. Wang, H.; Udukala, D. N.; Samarakoon, T. N.; Basel, M. T.; Kalita, M.; Abayaweera, G.; Manawadu, H.; Malalasekera, A.; Robinson, C.; Villanueva, D.; Maynez, P.; Bossmann, L.; Riedy, E.; Barriga, J.; Wang, N.; Li, P.; Higgins, D. A.; Zhu, G.; Troyer, D. L.; Bossmann, S. H., Nanoplatforms for highly sensitive fluorescence detection of cancer-related proteases. *Photochem. Photobiol. Sci.* **2014,***13* (2), 231-240.
23. http://www.thermofisher.com/us/en/home/references/molecular-probes-the-handbook/tables/r0-values-for-some-alexa-fluor-dyes.html

24. Merid, Y. Study of Cyanine Dye Binding to Amino Acids and Its Analytical Utility. Georgia State University, 2010.
25. Alshetaiwi, H. S.; Balivada, S.; Shrestha, T. B.; Pyle, M.; Basel, M. T.; Bossmann, S. H.; Troyer, D. L., Luminol-based bioluminescence imaging of mouse mammary tumors. *J. Photochem. Photobiol., B* **2013,***127*, 223-228.
26. Udukala, D. N., Protease assasys for cancer diagnostics, Kansas State University, 2014.
27. Lee, M. H.; Kim, J. S.; Sessler, J. L., Small molecule-based ratiometric fluorescence probes for cations, anions, and biomolecules. *Chem. Soc. Rev.* **2015,***44* (13), 4185-419
28. Amblard, M.; Fehrentz, J.; Martinez, J.; Subra, G. Methods and protocols of modern solid phase peptide synthesis. *Mol. Biotechnol.* **2006**, *33*, 239-254.
29. Carreon, J. R.; Stewart, K. M.; Mahon Jr, K. P.; Shin, S.; Kelley, S. O. Cyanine dye conjugates as probes for live cell imaging. *Bioorg. Med. Chem. Lett.* **2007**, *17*, 5182-5185.

Chapter 4 - Combinatorial phenotypic screen uncovers unrecognized family of extended thiourea inhibitors with copper-dependent anti-staphylococcal activity

Acknowledgements

I would like acknowledge all the collaborators, who contributed their knowledge and expertise towards the success of this project. Also I would like to thank Saran Kupul for excellent technical assistance and lab management. Some research of this study was supported in part by the University of Alabama at Birmingham Center for AIDS Research (UAB CFAR) and its Cytometry Core/Joint UAB Flow Cytometry Core which are funded by NIH/NIAID P30 AI027767 and by NIH 5P30 AR048311, and NIH grant RO1 AI104952 to F.W S.H.B. thanks the National Science Foundation for supporting this study (DMR-1242765 and CBET-1337438), as well as University of Alabama at Birmingham, Department of Medicine.

This material described in chapter 4 has led to the following publication. Whereas the biological research was performed by the group at UAB, I was the principal chemistry graduate student on the team. I have discovered the novel complexation mode of Cu(I) by drugs with NNSN motif. My research has also established that drugs with modest Cu(I)-binding constants are suitable for activation via nutritional immunity.

Combinatorial phenotypic screen uncovers unrecognized family of extended thiourea inhibitors with copper-dependent anti-staphylococcal activity

Alex G. Dalecki[1], Aruni P. Malalasekera[2], Kaitlyn Schaaf[1], Olaf Kutsch[1], Stefan H. Bossmann[2], Frank Wolschendorf[1#]

[1]Department of Medicine, University of Alabama at Birmingham, Birmingham, AL, USA;
[2]Department of Chemistry, Kansas State University, Manhattan, KS, USA;

4.1. Abstract

The continuous rise of multi-drug resistant pathogenic bacteria has become a significant challenge for the health care system. In particular, novel drugs to treat infections of methicillin-resistant Staphylococcus aureus strains (MRSA) are needed, but traditional drug discovery campaigns have largely failed to deliver clinically suitable antibiotics. More than simply new drugs, new drug discovery approaches are needed to combat bacterial resistance. The recently described phenomenon of copper-dependent inhibitors has galvanized research exploring the use of metal-coordinating molecules to harness copper's natural antibacterial properties for therapeutic purposes. Here, we describe the results of the first concerted screening effort to identify copper-dependent inhibitors of Staphylococcus aureus. A standard library of 10000 compounds was assayed for anti-staphylococcal activity, with hits defined as those compounds with a strict copper-dependent inhibitory activity. A total of 53 copper-dependent hit molecules were uncovered, similar to the copper independent hit rate of a traditionally executed campaign conducted in parallel on the same library. Most prominent was a hit family with an extended thiourea core structure, termed the NNSN motif. This motif resulted in copper-dependent and copper-specific S. aureus inhibition, while simultaneously being well tolerated by eukaryotic cells. Importantly, we could demonstrate that copper binding by the NNSN motif is highly unusual and likely responsible for the promising biological qualities of these compounds. A subsequent chemoinformatic meta-analysis of the ChEMBL chemical database confirmed the NNSNs as an unrecognized staphylococcal inhibitor, despite the family's presence in many chemical screening libraries. Thus, our copper-biased screen has proven able to discover inhibitors within previously screened libraries, offering a mechanism to reinvigorate exhausted molecular collections.

4.2. Introduction

The advent of high throughput screening (HTS) technologies over thirty years ago revolutionized drug discovery efforts. Having apparently exhausted the readily identifiable repertoire of natural antibacterials derived from soil bacteria, HTS strategies began a renaissance in drug discovery, promising an effectively unlimited supply of novel compounds to combat the emerging threat of antibiotic resistance [1]. However, despite ever-expanding compound libraries and highly efficient screening methodologies, new classes of synthetic antibiotics have yet to materialize. The increasing concerns of returning to a pre-antibiotic era have proven severe enough to warrant attention and action by top governmental agencies [2,3].

Of the sixteen antibiotic classes used clinically, all but two were derived from environmental sources, and there is growing interest in returning to natural inspirations [1,4–6]. Among these inspirations lies metal-mediated innate immunity, by which the innate immune system directly modulates environmental levels of metals such as manganese, iron, zinc, and copper at the site of infection [7,8]. Through limitation, in the case of iron, zinc, and manganese or oversaturation, in the case of copper, the intrinsic properties of these ions are utilized to form a crucial line of defense against pathogens. Growing bodies of evidence point toward copper's essentiality in particular. In many systems, including *Mycobacterium tuberculosis*, *Pseudomonas aeruginosa*, *Listeria monocytogenes*, and *Streptococcus pneumoniae*, bacterial copper resistance is linked to virulence; [9] conversely, attenuation of the ''copper burst'' within macrophages weakens the phagocytic response, promoting bacterial survival [10,11]. All sequenced bacteria possess at least a rudimentary level of copper resistance machinery,[12] varying from simple expression of an efflux pump,[13] to a complex network including pumps, sequestration proteins, oxidases, chaperones, and transcriptional regulators [14]. As free copper levels are

buffered below one ion per cell in both prokaryotes [15] and eukaryotes,[16] that even obligate intracellular bacteria retain resistance machinery further underscores copper's profound role as an environmental and immunological insult [12].

Recent advances in our understanding of copper's role in immunity have paralleled the rise of reports detailing the phenomenon of copper-dependent antibiotics. These compounds are highly inhibitory in the presence of copper, yet impotent in its absence. Example inhibitors have been described for Gram negatives,[17] Gram positives,[18] and mycobacteria,[19] as well as eukaryotic targets including pathogenic fungi [20] and cancer cells [21–23]. The broad range of potential targetable pathogens, coupled with the wide array of novel mechanisms of action, has generated interest in exploiting copper's antibiotic properties [24,25]. However, until now, discoveries have been largely serendipitous, or based upon established metal-binding motifs; though well suited for chemical probes, these scaffolds are often poorly adaptable to therapeutic uses. Exploring the full potential of copper-mediated therapeutics requires new motifs and a directed discovery effort to identify proof-of-principle compounds.

Here, we demonstrate for the first time the power of a copper focused HTS screening campaign. This approach is uniquely able to uncover new interactions between copper ions and compounds in existing chemical libraries, and their subsequent synergistic inhibitory activities. A copper-biased combinatorial screen against *Staphylococcus aureus* revealed nearly twice as many hits as a traditional, copper-blind campaign. A reoccurring extended thiourea motif, dubbed NNSN, featured novel copper binding properties, and was revealed by UV/Vis and NMR analysis to participate in a new interaction between the ligand and copper ion. This motif was highly inhibitory against *S. aureus* in a copper-dependent and copper-specific manner, yet was well tolerated in cell culture. Finally, despite their presence in many screening libraries, a

chemoinformatic meta-analysis demonstrated NNSNs as previously unrecognized antistaphylococcal agents, confirming the ability of copper-biased screens to discover new compounds hiding in existing chemical space.

4.3. Methods

4.3.1. Bacterial strains, antibiotics and compounds

S. aureus clinical isolate SA3 (resistant to ampicillin, clindamycin, erythromycin, penicillin, and tetracycline) was characterized by and obtained in a de-identified manner from UAB Laboratory Medicine. Bacteria were routinely grown in Mueller Hinton (MH) medium (Oxoid Ltd, Basingstoke, Hampshire, England) overnight at 37 ^{0}C before inoculating plates according to assay conditions unless otherwise stated. All experiments were performed in 96-well plates using MH medium or RPMI 1640 medium supplemented with trace metals. The trace metal mix was prepared as a 1000-fold stock solution containing 3 mM EDTA, 50 mM $MgCl_2$, 0.7 mM $CaCl_2$, 80 mM $NaMoO_4$, 168 mM $CoCl_2$, 0.55 mM $MnCl_2$, 0.7 mM $ZnSO_4$, 2 mM $FeSO_4$. All screened compounds were randomly taken from our 43,000 in-house compound library (Chembridge) or Chembridge's Hit2Lead online library (www.hit2lead.com). Copper sulfate and all other commercial compounds were purchased from Sigma-Aldrich. Copper treated assays were supplemented with 50 mM $CuSO_4$ unless otherwise indicated. Other metals were used at 100 mM or as indicated.

4.3.2. High throughput screening assay

The HTS assay was conducted as published previously [18]. Briefly, all compounds were screened at 10 mM in duplicate plates run in parallel, one containing only medium (trace-copper conditions) and one containing medium supplemented with 50 mM $CuSO_4$. *S. aureus* was added to each well to achieve a final optical density (OD_{600}) of ~ 0.001 to 0.004 (1 : 1000 dilution of an overnight culture) in a total volume of 160 mL. All steps were performed using the Precision automated microplate pipetting system (BioTek). Plates were sealed with parafilm (Millipore) to minimize evaporation and incubated on a Heidolph Titramax 1000 plate shaker at 450 rpm at 37 ^{0}C for 8 hours. Optical density, as a quantitative surrogate marker of bacterial growth, was determined using a Synergy HT plate reader (BioTek). Background correction was performed against wells containing only medium and compounds that decreased the growth of *S. aureus* were identified and further analyzed.

4.3.3. HTS data analysis

An in-house algorithm was utilized for analysis. The software package used MySQL and PHP as a server backend, and a web accessible HTML interface as the front end. Hits were defined based upon number of standard deviations (1 SD = 20%) from the overall mean, which averaged 94% across all copper-replete samples after blank correction and normalization to positive controls. Independent hits were compounds with less than 34% growth (3 SDs from the mean) in both standard and copper supplemented conditions. Copper dependent hits had under 34%growth in the copper replete plate, with at least 40 percentage points (2 SD) more growth in copper trace plates (e.g., 20% growth in Cu-replete and 460% growth in Cu-trace plates). Inverse hits were the opposite, with under 34% growth in trace plates and at least 40 percentage points

more growth in replete plates. Substructure analysis was completed using the Open Babel 2.3.2 chemistry toolbox, as installed on a Linux server.26 The SMARTS search string for non-cyclic thioureas was "[N;!R]C(=S)[N;!R]," while the NNSN substructure search was extended to "[#7][#6][N;!R]C(=S)[N;!R]" to include both cyclic and non-cyclic carbons and nitrogens.

4.3.4. Structure Activity Relationship (SAR) Studies (SAR-by-catalogue)

Active molecules were grouped based on the occurrence of structural motifs identified during visual and computational inspection of their chemical structures. Representative compounds and additional derivatives of each group were ordered from www. hit2lead.com. Activity was confirmed in dose response curves, of which we also determined the MIC (for details see below). Additional compounds featuring respective key motifs were identified in the Chembridge Hit2Lead online library using the search feature provided on the website (www.hit2lead.com).

4.3.5. Determination of the minimal inhibitory concentration (MIC)

Compounds were reconstituted in sterile DMSO (Sigma-Aldrich) typically at a concentration of 10 mM, then aliquotted, and stored at -80 ^{0}C. In some instances, a decline in potency of the compounds was noted over a period of 6 months and after repeatedly freezing and thawing reconstituted compounds. Compounds were diluted in 96-well in 2-fold increments, typically covering a concentration range from ~ 0.07 to 10 mM. Control wells containing media only (sterility control) and media with cells in the absence of compound with or without 50 mM copper were included as well. Assay conditions and incubation procedure were similar to that of the pilot screen. Dose–response curves were analyzed by determining the OD_{600} using a plate

reader (Synergy HT, BioTek). Data was analyzed as the average value of 3 wells with identical conditions and normalized to the proper growth controls. MIC was defined as the concentration at which growth was reduced by at least 85%. Additional transition metals were assayed in Roswell Park Memorial Institute 1640 medium without phenol red (RPMI; Life Technologies) and supplemented with a 1 : 1000 dilution of a copper-free trace metal mix (RPMI1640 + TM) to promote growth [27].

4.3.6. Eukaryotic toxicity assessment

THP-1 cells were grown in standard RPMI plus 10% FBS. Cells were plated in RPMI at 100 000 cells per well in a total volume of 200 mL in a 96 well plate, and challenged with compound in the presence or absence of 15 mM Cu for 24 hours. This copper concentration was well tolerated by THP-1 cells in our system and lies within the physiological range of copper levels in blood (10–25 mM) [28]. Viability was read using a Guava flow cytometer, through gating on live populations as assessed through forward and side scatter measurements.

4.3.7. Characterization of metal complexation and structure modeling.

The binding constants of CuBr in Trizma-HCl (pH = 7)/methanol (90/10 v/v) to compounds were determined according to the method of Benesi and Hildebrand [29]. The binding of Cu(II) and Cu(I) enhances the UV-absorption band of APT-6i at λ_{max} = 235 nm. The differences in UV-absorption at λ_{max} = 235 nm were used to calculate the binding constants KB. UV/Vis spectra of 8.3, 17, 41, 83, 170 and 410 nM of APT-6i were recorded in the absence and presence of 10 mM CuBr (Sigma-Aldrich, ACS grade) at 283 K in Trizma-HCl (pH = 7.0)/methanol (1 : 1 v/v) using a Varian Cary 500 UV/Vis-NIR spectrophotometer and 4.0 mL

quartz cuvettes. The measurements were performed under argon to avoid Cu(I) oxidation to Cu(II).

4.3.8. NMR Titrations:

^{1}H-NMR spectra were recorded using a Bruker Avance III, 600 MHz NMR-spectrometer at 298K. Compound APT-6i was dissolved in deuterated acetone (6.25 mM), total volume: 400 µl. Cu(I) was added from a stock solution of 1.5 x 10^{-4} M CuBr in deuterated acetone. 5 mL of CH_3OD was added as internal standard (peak not shown).

4.3.9. ChEMBL database meta-analysis.

The ChEMBLdb relational database, version 20, was downloaded as the provided virtual machine (MyChEMBL; (30, 31). All SQL searches were conducted from a Linux command line interface.

4.4. Results

4.4.1. Copper-biased HTS environment uncovers numerous copper-dependent hits.

4.4.1(A) Nearly twice as many hits discovered through copper-biased screen as in a traditional screen.

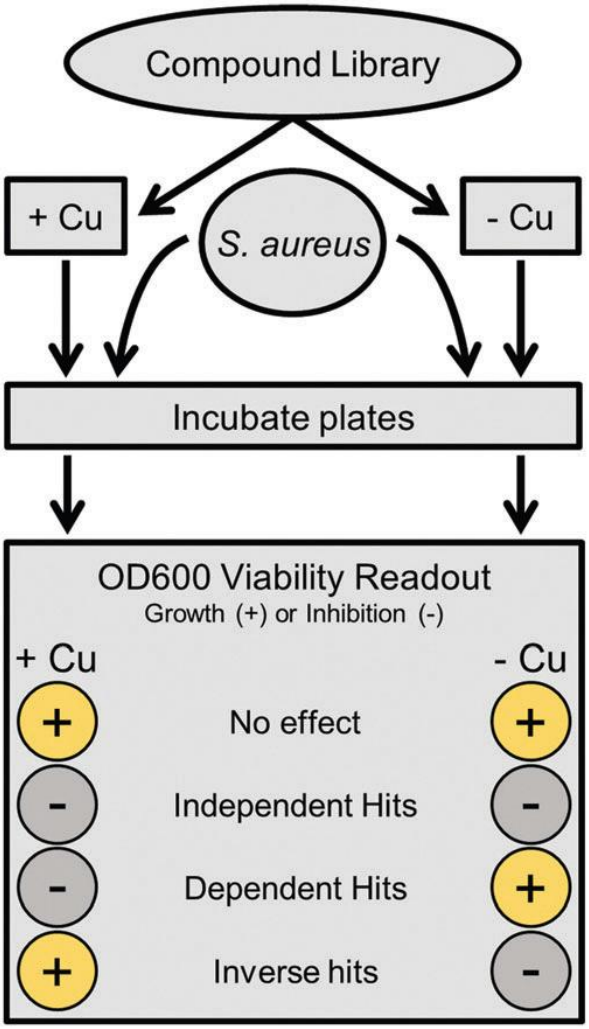

Figure 4.1: Parallel combinatorial scheme. Compounds from a master library are assayed twice in parallel, with one plate containing added copper sulfate, and the other containing only base medium. After adding S. aureus, both plates are incubated and viability is determined via OD600. Hits were classified by comparing growth values in both plates; the specific criteria used are detailed in the Methods.

Metal-based antibiotics have not yet advanced to clinical or veterinarian use and are therefore an attractive alternative to conventional antibiotics. Surprisingly, high throughput screening (HTS) solutions for the discovery of novel metal-related antibacterial activities do not exist. We focused our screen on compounds that display antibacterial properties through the interaction of copper because of its potential physiological relevance in the context of coppermediated innate immune functions [7,24], competitiveness over other physiological metal ions [32], and intrinsic antibacterial properties [33]. To reveal novel copper binding compounds not active in the absence of copper, we conducted a parallel screen, in which compounds were tested both under standard, traditional conditions, as well as in the presence of copper (Figure 4.1). This strategy allowed us to comprehensively determine the spectrum of effects that copper ions might have on the antibacterial properties of potential bacterial inhibitors with copper-related activities (enhancing or mitigating). Screening only in the presence of copper and testing only hits for their activity in the absences of copper would have missed a group of compounds that we classify as inverse hits. We chose to screen at 50 mM copper to enable detection of compounds with weaker copper-dependent activity (classified as secondary and tertiary hits), in order to better inform SAR, hit cluster expansion, and hit prioritization strategies.

Screening our 10 000 compound test library against a clinically isolated drug-resistant *S. aureus* strain (SA3) identified 129 total hits, or 1.29% of the overall number of compounds. Comparison of the hits from both the trace-copper screen (Figure 4.2A) and copper supplemented screen (Figure 4.2B) revealed 70 compounds (54%) that were similarly inhibitory under both screening conditions (copper independent hits) and 6 compounds (5%) that lost their antibacterial properties in the presence of copper (copper inverse hits).Importantly, 53 molecules

(41%) were found only in the presence of copper, demonstrating that copper-activated antibacterial activities occur rather frequently. Of the copper-dependent hits, over half (28) met our criteria for a primary hit, i.e., more than 90% inhibition. These copper-dependent hits represent hitherto unrecognized inhibitors, given that conventional screening campaigns for antibiotics do not contain sufficient and physiological quantities of copper ions.

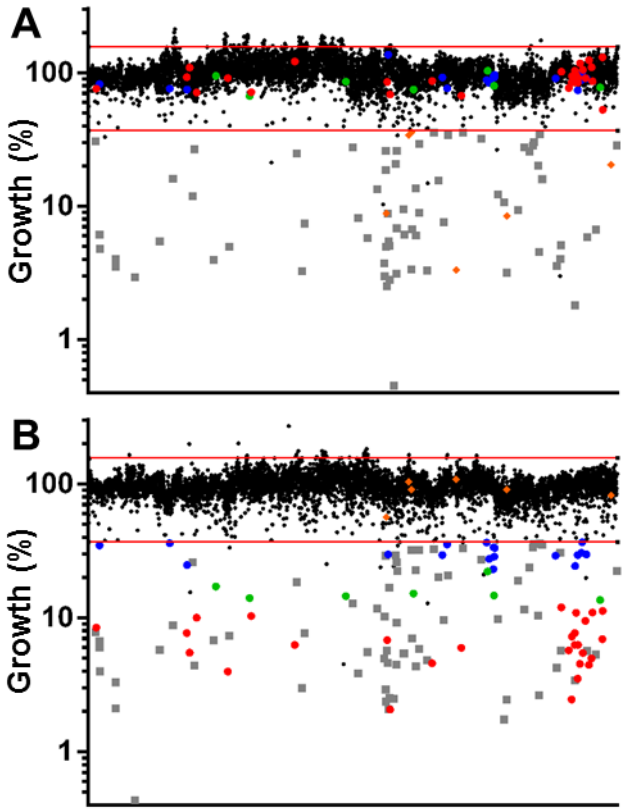

Figure 4.2: Combinatorial screening results.

(A) Growth values of all 10 000 compounds in standard screening medium as normalized to plate controls. The red lines represent three standard deviations above and below the mean growth value as a cutoff for hits.

(B) Growth values of all compounds in medium with copper added, as normalized to plate controls. Red, green, and blue circles are Primary (growth ≤10%, and greater than 2 SD below the –Cu plate), Secondary (10% > growth ≤ 20%, and greater than 2 SD below the –Cu plate),

and Tertiary (20% > growth ≤ 34%, and greater than 2 SD below the –Cu plate) dependent hits; grey boxes are independent hits; and orange diamonds are inverse hits. Some outliers may have fallen below the lower cut-off line but were classified as inactive because they did not meet hit criteria.

4.4.1(B) Copper-dependent hits display significantly different chemical properties compared to the library as a whole

Unfortunately, there is often a great disparity between molecules with desirable activities and molecules that are ‘‘druggable’’. To concentrate discovery efforts on promising compounds, coefficient (c log P) ≤ 5, hydrogen bond donors 5, and hydrogen bond acceptors ≤ 10. The criteria were later extended to include topological polar surface area (tPSA) ≤ 140 Å2 and rotational bonds (RB) ≤ 10. To visualize our results in aggregate, we compared Ro5 values of dependent hits, independent hits, inverse hits, and the screened library as a whole. Molecular weight only varied slightly between groups, and all were statistically indistinguishable from the library as a whole (Figure 4.3A). Rotational bonds and c log P values were slightly significantly different when comparing copper-dependent hits to the screened library ($p = 0.0122$ and 0.0116, respectively), though all three categories clustered toward the top of the c log P and bottom of the RB ranges (Figures 4.3B and 4.3C). Topological polar surface area (tPSA) differed greatly between dependent hits and all other categories ($p < 0.0001$), with the dependent hit median tPSA 38% lower than the library average (Figure 4.3D). The most striking comparison, however, came from numbers of hydrogen bond donors and acceptors. The screened library had a relatively even distribution of both acceptors and donors (Figure 4.3E), with a median of 4 acceptors and 1 donor; while the median of copper-dependent hits clustered tightly at only 1

acceptor and 2 donors (Figure 4.3G). These structural differences may enable assembly or construction of custom libraries targeted towards enhanced copper-binding molecules.

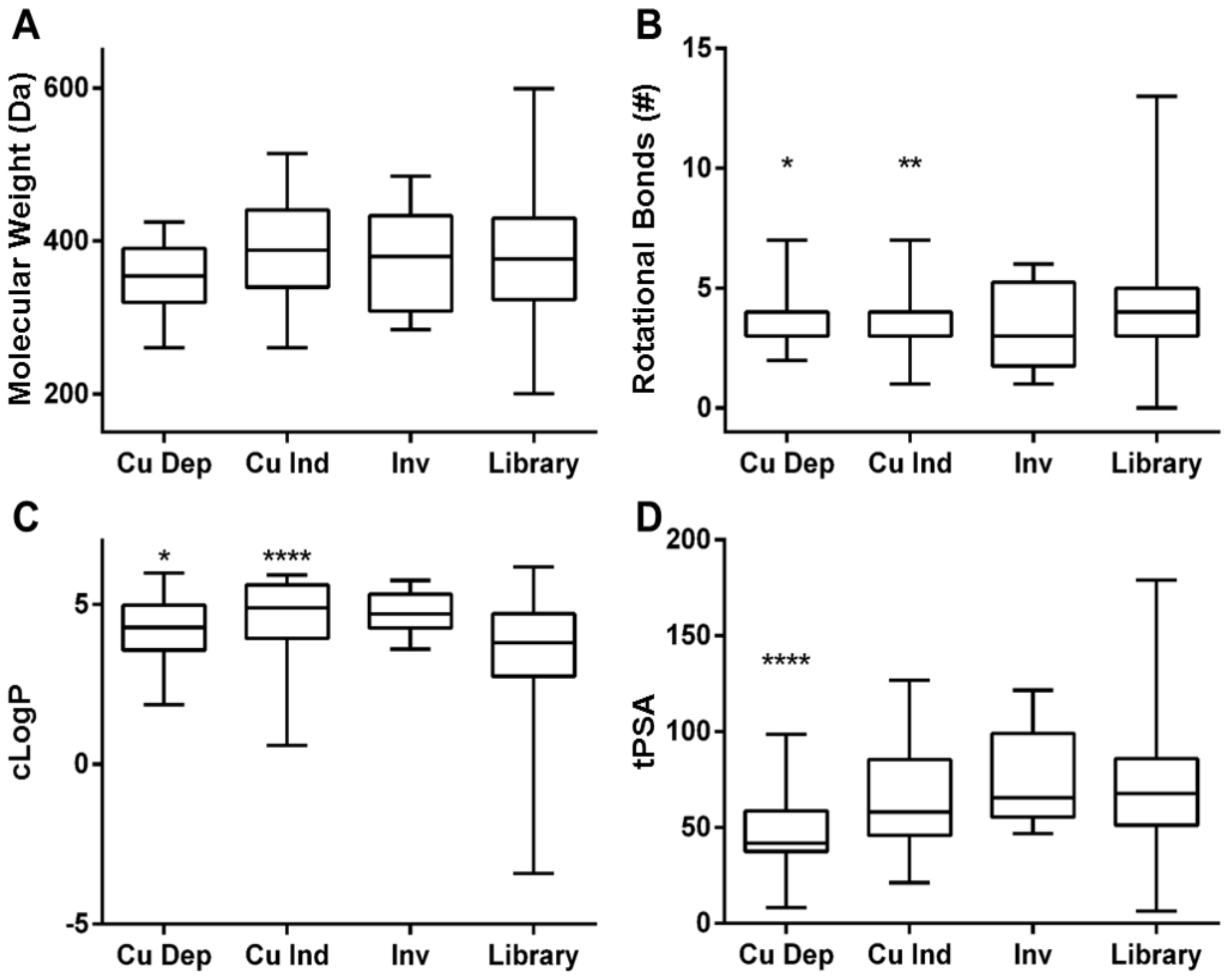

Figure 4.3: Lipinski Rule of Five characteristics.

Aggregate (A) molecular weight, (B) rotational bonds, (C) calculated LogP (cLogP), and (D) topological polar surface area (tPSA) properties of copper-dependent hits (Cu Dep), copper-independent hits (Cu Ind), and inverse hits (Inv).

All groups were compared to the screened library as a whole (Library) using a one way ANOVA and Dunnett's multiple comparisons test. * $p < 0.05$, ** $p < 0.01$, **** $p < 0.0001$.

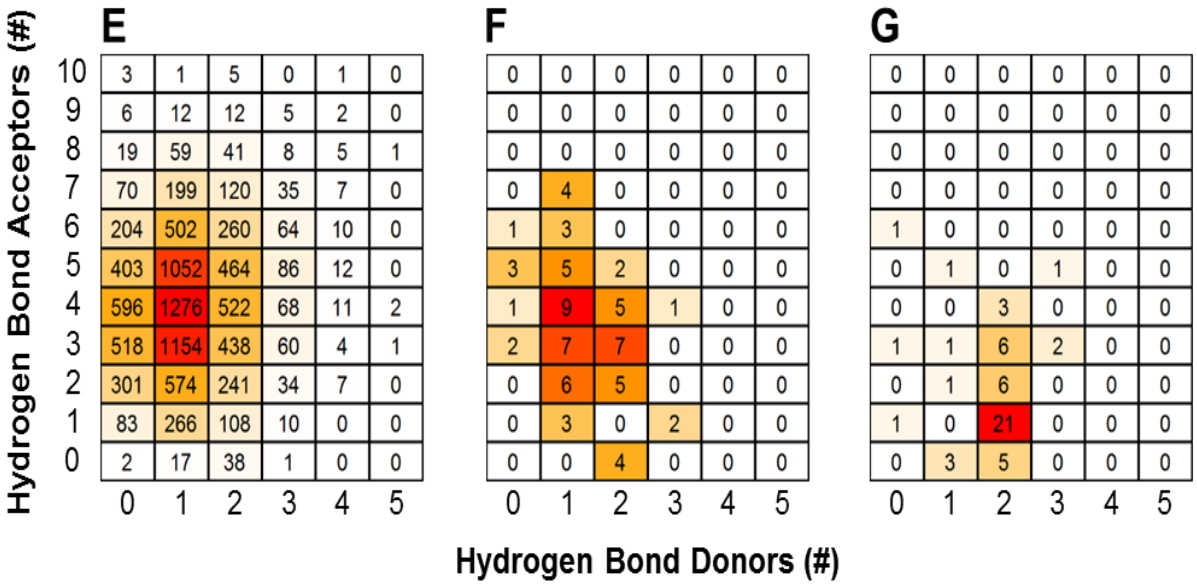

Figure 4.3: Lipinski Rule of Five characteristics.

(E) Heatmap comparisons of the hydrogen bond acceptors and donors within the entire screened library, (F) copper-independent hits, and (G) copper-dependent hits.

4.4.2. Extended thiourea structure comprised a well-established hit cluster

4.4.2(A) Novel NNSN motif associated with copper-dependent antistaphylococcal activity

While our data indicates that the presence of physiologically relevant trace elements, specifically copper, reveals new hit molecules within a given compound collection, it is also important to demonstrate that the identified hits found by this alternative method are functionally relevant and responsive to optimizations. To substantiate this, we began a substructure analysis of our copper-dependent hits with the goal to identify repeatedly occurring chemical motifs and use such motifs as starting points for future SAR analysis. Thioureas (Figure 4.4A) dominated our copper-dependent hits, comprising 45 of the 53 total hits, or 85%. Such a high proportion greatly contrasted with the library as a whole, which featured only 570 thioureas in total (5.7%). Further, thioureas were not found to be generally active but rather possessed a specific copper-

dependent activity, as only 7 of the 70 copper-independent hits contained a thiourea motif. This fraction was not significantly different in proportion from the entire library as judged by a chi-squared analysis ($p = 0.119$). Thus, not only did the screening conditions appear to have enriched our results specifically for the thiourea motif, but also have identified thioureas as the first example of a discrete chemical substructure identified by HTS that possesses strictly metal-dependent antibacterial activities.

Interestingly, 12 of the 45 thioureas featured an extendedthiourea structure, which we dubbed NNSN-motif (Figure 4.4B). No NNSN-motif was found among the copper-independent hits. All 12 copper-dependent NNSN molecules featured a linear thiourea structure, complemented by a heterocyclic ring system (pyrazolyl, tetrazolyl, thiazolyl, pyridinyl, pyrimidinyl or pyrazinyl) to form the full NNSN motif (Figure 4.4C). Molecular flexibility appeared to be essential for activity since rigid NNSN motifs with a cyclic thiourea structure as in triazolethiones (Figure 4.4D), imidazopyrimidine- thiones (Figure 4.4E) or pyrido-pyrimidine-thiones (Figure 4.4F) were inactive. A substructure search within the structures of all 10 000 randomly pickedmolecules that were included in our screen identified 30 total non-cyclic NNSN motifs; thus, the screen discovered 40% of all possible NNSN molecules.

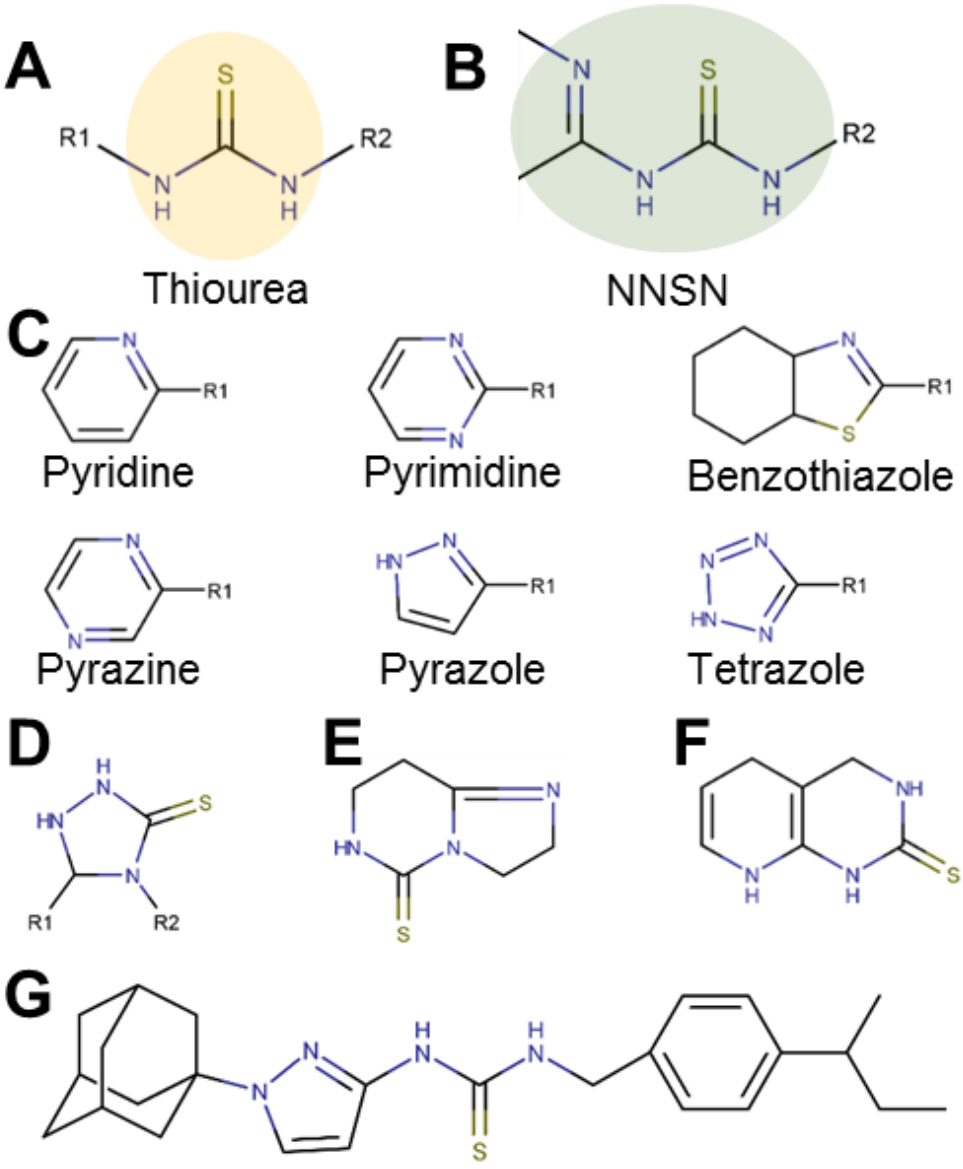

Figure 4.4: A novel copper-binding NNSN motif and side groups.

47 copperdependent hits contained a thiourea (A), with 12 featuring an extended NNSN motif (B) that consists of the thiourea base group paired with one of 6 possible heterocyclic nitrogen-containing ring structures (C). Compounds with a rigid and inflexible NNSN motif (D, E and F) conferred no activity. (G) Full structure of APT-6i.

4.4.2(B) Adamantyl-bearing pyrazolyl-thioureas (APTs) yielded fruitful structure activity relationship analysis

In order to probe whether NNSN-compounds have the potential of being further developed towards early lead status, we conducted a limited structure activity relationship study on 9 commercially available pyrazolyl-thiourea derivatives featuring an adamantly group (Figure 4. 5). Adamantyl bearing pyrazolyl-thioureas (APTs) were chosen because adamantyl substituents are known to improve drug stability and plasma half-life by impeding the access of hydrolytic enzymes through restricting or altering intramolecular reactivity,[36] and because adamantyl groups have no significant reactivity allowing us to link activity differentials to other substituents.[36] No activity was observed in medium without copper for any of these molecules, but in copper supplemented medium the compounds had minimum inhibitory concentrations (MICs) between 0.3 and 10 mM (Figure 4.5).

Among the analogs tested, APT-6i (Figure 4.4G) exhibited excellent copper-dependent inhibition of S. aureus (Figure 4.6A), with a minimum inhibitory concentration of 0.3 mM. Additionally, APT-6i was relatively benign toward THP-1 cells, a human monocyte cell line (Figure 4.6A). Activity was also entirely copper specific, with no observed inhibition when growth media was supplemented with other transition metals such as Mn, Fe, Co and Zn (Figure 4.6B). However, the presence of additional metals did not preclude activity, as full inhibition was restored upon co-incubation of Zn and Cu with APT-6i (Figure 4.6B).

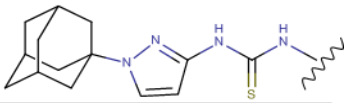

	Structure	MIC
6a	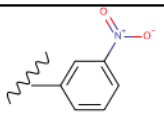	10
6b	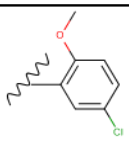	5-10
6c	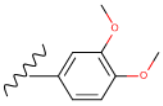	5-10
6d	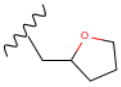	5-10
6e	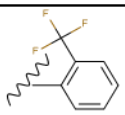	2.5
6f	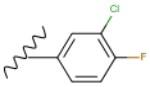	2.5
6g	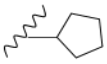	1.25
6h	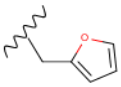	0.6
6i	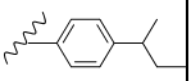	0.3

Figure 4.5: Structure activity relationship analysis. Nine analogs of a promising hit molecule were purchased from the supplier (ChemBridge) and examined for antimicrobial activity.

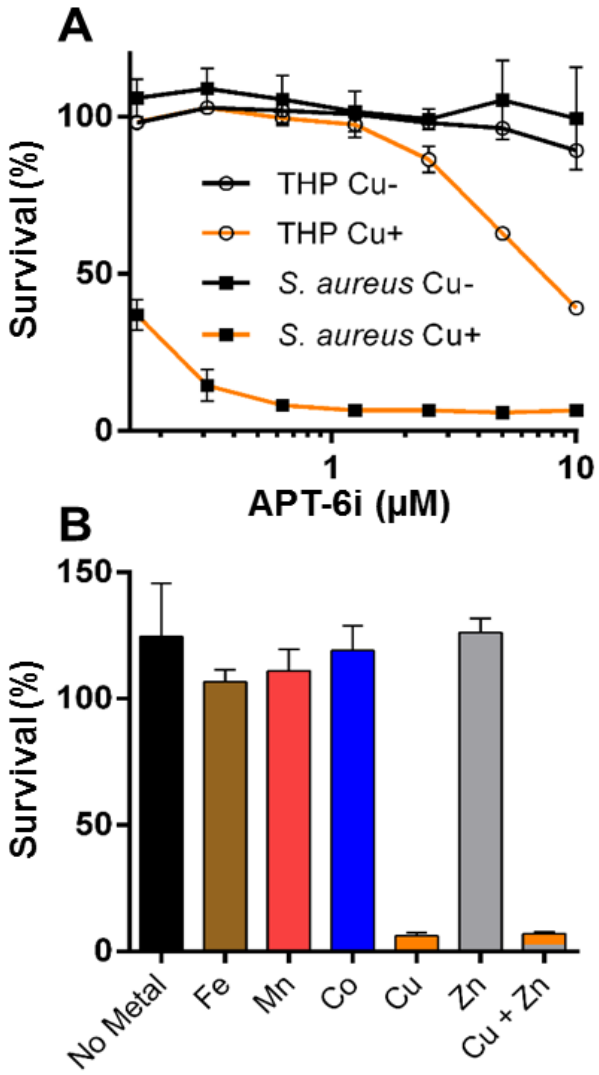

Figure 4.6: APT-6i exhibits stark copper dependency and specificity.

(A) Inhibitory effects of APT-6i against *S. aureus* (black squares) and THP-1 cells, a human monocyte line (open circles). APT-6i is active only in the presence of copper (orange line). (B) Activity of 10 μM APT-6i against *S. aureus* grown in RPMI to better resolve metal dependencies. Cu is included at 50 μM, and Fe, Mn, Co, and Zn are included at 100 μM. Inhibition is strictly copper-specific, and occurs in the presence of other ions, such as a Cu/Zn coincubation. All values are normalized to the respective 0 mM compound control (either with or without copper), and expressed as percentages of survival.

4.4.3. Pyrazolyl-thioureas are functionalized through unique copper-coordination chemistry

To further examine the interaction between APT-6i and copper, we analyzed the metal–ligand complex using UV-Vis spectroscopy and ^{1}H-NMR. UV-Vis titrations are a straightforward method to visualize metal–ligand complex formation, and revealed a main absorption peak at λ = 235 nm, with intensity strongly dependent on the APT-6i concentration (Figure 4.7A). This peak represents an energy shift in electron orbitals, indicative of complex formation and subsequent p bonding between the copper ion and ligand. Further analysis through the Benesi–Hildebrand method [29] produced linear plots, confirming a 1 : 1 stoichiometry within the ligand–metal complex (Figure 4.7B). The binding constant of CuBr and APT-6i in Trizma/methanol was calculated to KB = 476,700 ± 1200 (L mol^{-}1).

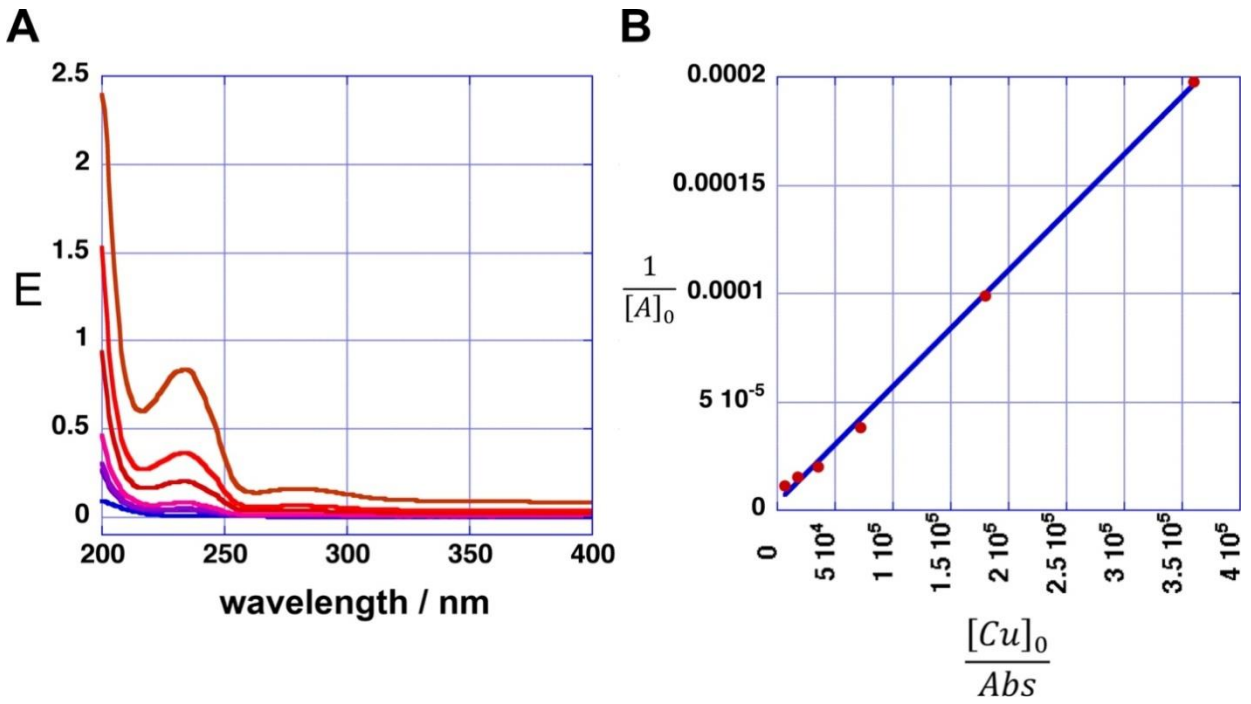

Figure 4.7: APT-6i forms a unique copper complex. (A) UV/Vis absorption spectra of compound APT-6i in the presence of 3.3 mM Cu(I)Br in in Trizma-HCl (pH=7)/methanol (90/10 v/v).

Concentrations of APT-6i were 8.3 nM, 17 nM, 41 nM, 83 nM, 170 nM and 410 nM. (B) Benesi Hildebrand plots for determining the binding constant and molar absorption coefficients of APT-6i with CuBr.

As we were unable to obtain crystal structures of the Cu(I) and APT-6i complex, we relied on 1H-NMR-titration with CuBr in deuterated acetone to discern the structure formed in solution (Figure 4.7C). Intriguingly, the ^{1}H-NMR titration confirmed that the observed 1:1 complexation geometry is clearly different from canonical Cu(I)-thiourea complexes, which usually feature at least two thiourea ligands per metal cation. It is especially noteworthy that both thioamide groups, but not the thiocarbonyl group, take part in the observed complexation. Following the shift of peak position 4 from d = 5.931 to 5.984 ppm with increasing CuBr concentration (Figure 4.7E), it is apparent that one of the aromatic carbons of the pyrazole unit is in close proximity to Cu(I) in solution, assuming that a CH_3OD molecule (added as internal standard) is also coordinated to Cu(I) in order to obtain a slightly distorted tetrahedral geometry. The solution structure of the APT-6i-Cu(I) complex is the basis for the molecular modeling (Figure 4.8 A–C). From our modeling, it becomes clear that significant conformational changes are required to accommodate the complexation of a central Cu(I) cation (Figure 4.8 B and C).

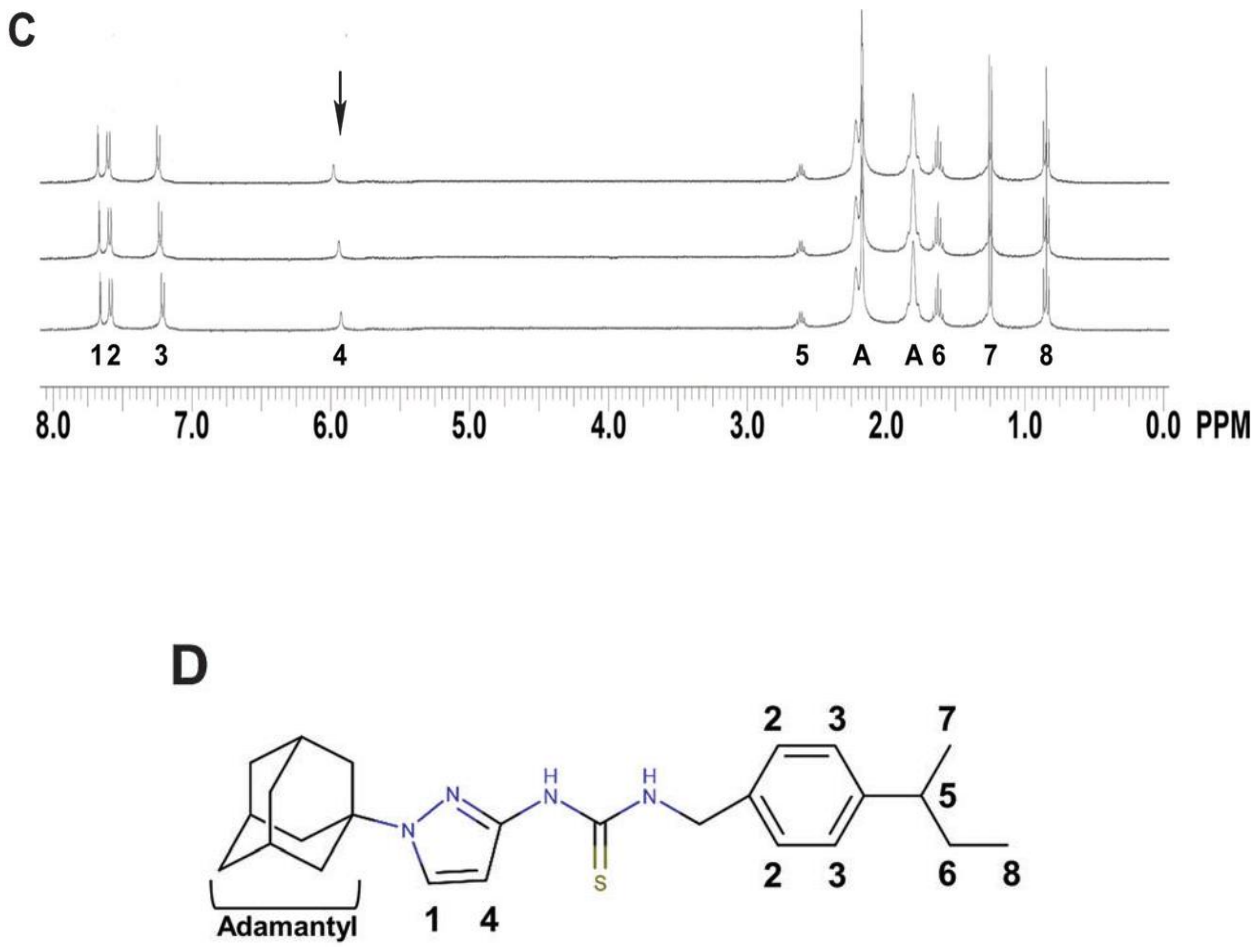

Figure 4.7: (C) Overlay of the 1H-NMR spectra (Bruker Avance III, 600 MHz, 298 K) of compound APT-6i without CuBr (bottom), with 50 mM CuBr (middle), and with 100 mM CuBr (top) in deuterated acetone. Peak assignments correspond to panel D with A = adamantyl. The arrow indicates a copper responsive peak shift.

(D) Structure of APT-6i showing relevant peak assignments and match with panel C.

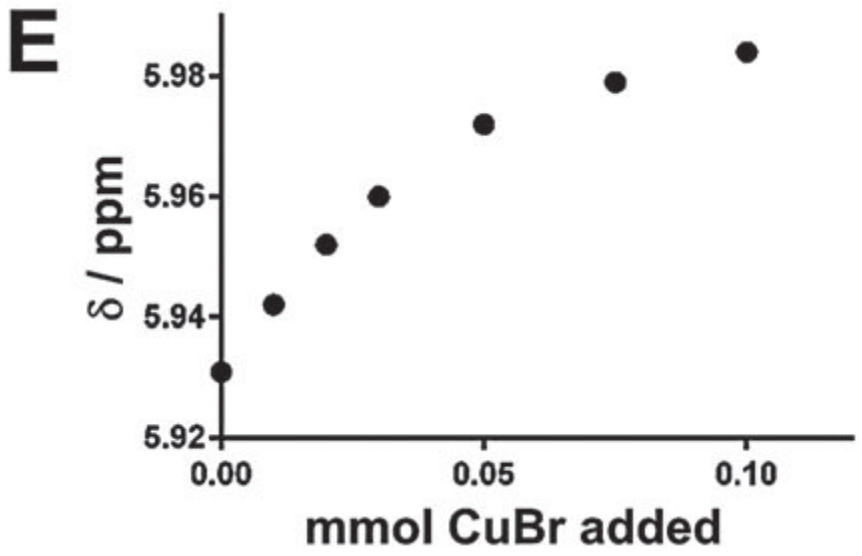

Figure 4.7: (E) Shift of highlighted peak 4 with increasing concentrations of CuBr from panel C, indicating an interaction with copper ions at these sites.

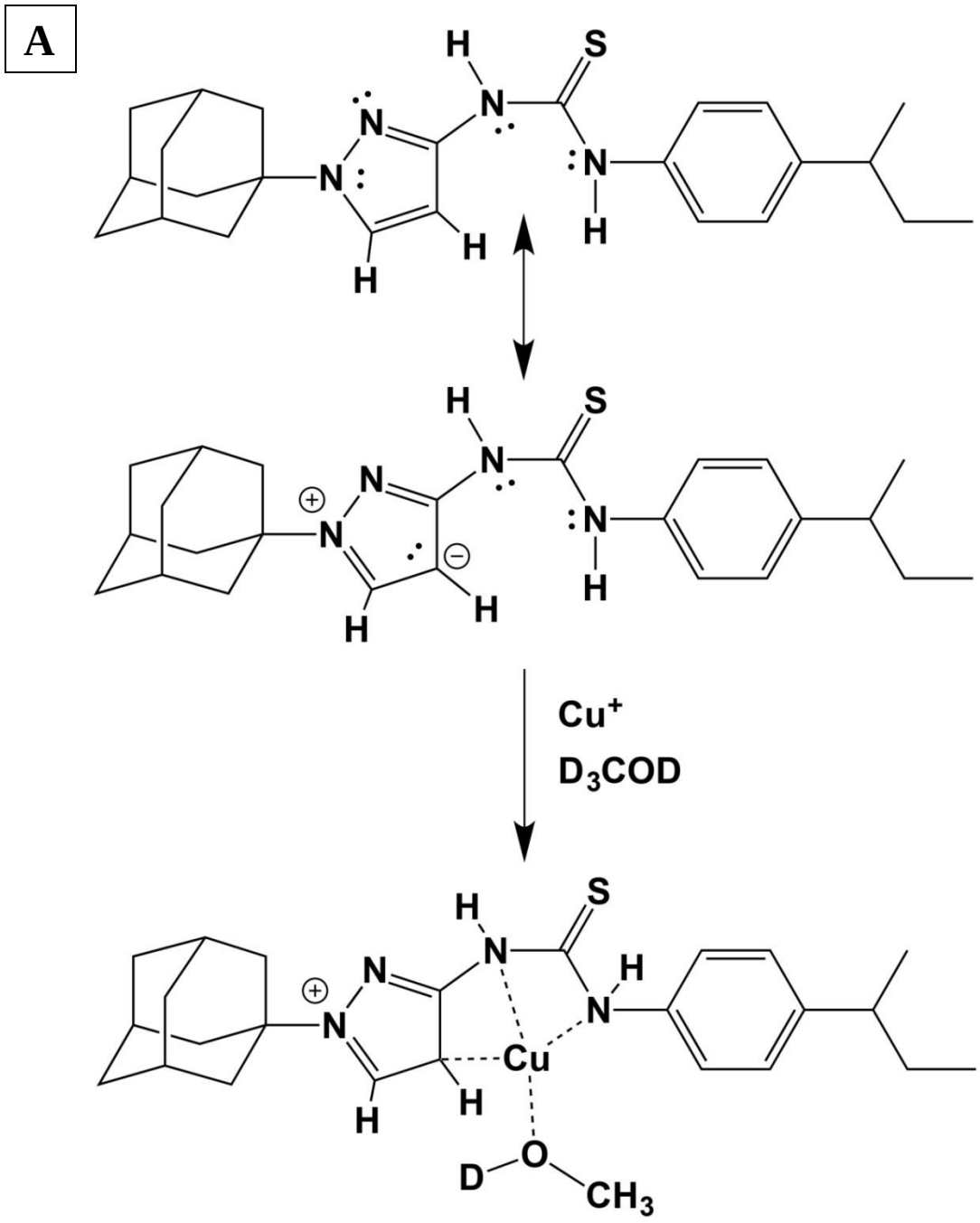

Figure 4.8: The APT-6i and copper complex has unique coordination chemistry. The complex's geometry was determined using UV Vis and ^{1}H-NMR, shown in Figure. 4.7.

(A) The (minor) resonance structure of APT-6i is able to form a complex with Cu(I).

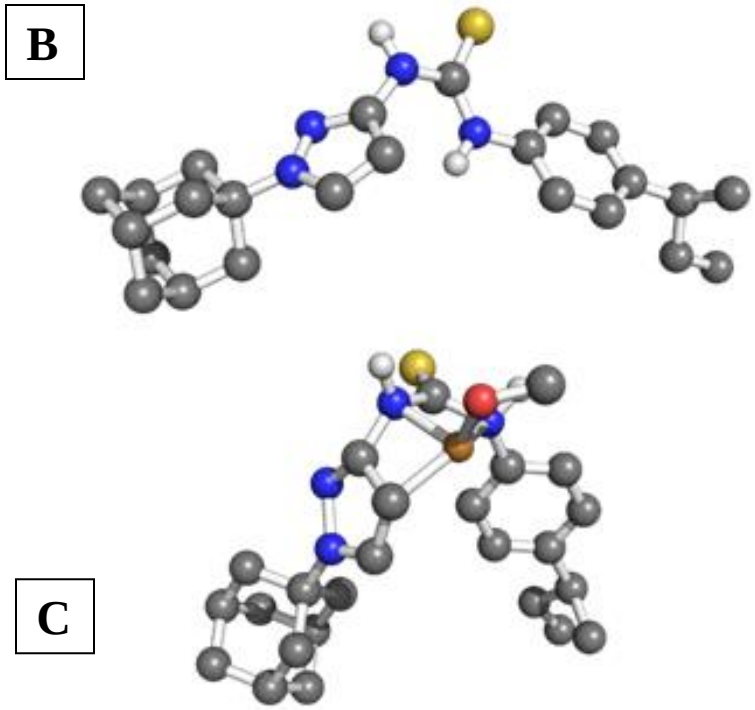

Figure 4.8:

(B) 3D representation of uncomplexed APT-6i using the CHARMM force field, showing a relatively linear structure. Non-polar hydrogens are removed for clarity.

(C) 3D model of the APT-6i/Cu(I)/CH_3OD complex. Coordination twists the molecule from a linear structure to a bent configuration. Copper is represented as the orange sphere, with a D1-methanol added to the coordination complex. Yellow sphere represents sulfur, blue are nitrogen atoms, grey are carbon atoms and white are polar hydrogens.

More importantly to drug discovery efforts, this novel complexation could potentially reopen the door to a wide array of otherwise unattractive compounds. Although thioureas readily complexes metal ions, and are thus logical candidates for discovery by the paradigm detailed here, they are often regarded as undesirable due to common hepatotoxicity and thyroid peroxidase inhibition [37]. Sulfur's lack of participation in the complex suggests the possibility of bioisoteric substitution of other functional groups or atoms, negating toxicity while retaining complexation ability and antibacterial activity. Previous reports offer precedent, though results are expectedly mixed: some substitutions, such as cyanoguanidines, retained activity or increased therapeutic indices,38 while others lost biological activity [39]. A concerted SAR effort would likely produce new metal-complexing non-thioureas.

4.4.4. Meta-analysis reveals NNSNs as previously unrecognized antistaphylococcal agents

Having identified the NNSN motif as a promising and novel copper-dependent antibacterial structure, we examined whether this motif had previously been recognized for its therapeutic potential. We conducted a meta-analysis of published activities using the ChEMBL database, a publically available relational database containing over 13million activity records of 1.4million compounds, taken from multiple sources including 2700 PubChem BioAssays and tens of thousands of primary literature reports [30]. The database facilitates tracking individual compounds through a large number of systems, such as biochemical assays, whole cell screens, and in vivo data, against prokaryotic and eukaryotic targets. Although ChEMBL does not generally include inactive hits, it is a rich repository of bioactive compounds in a variety of contexts.

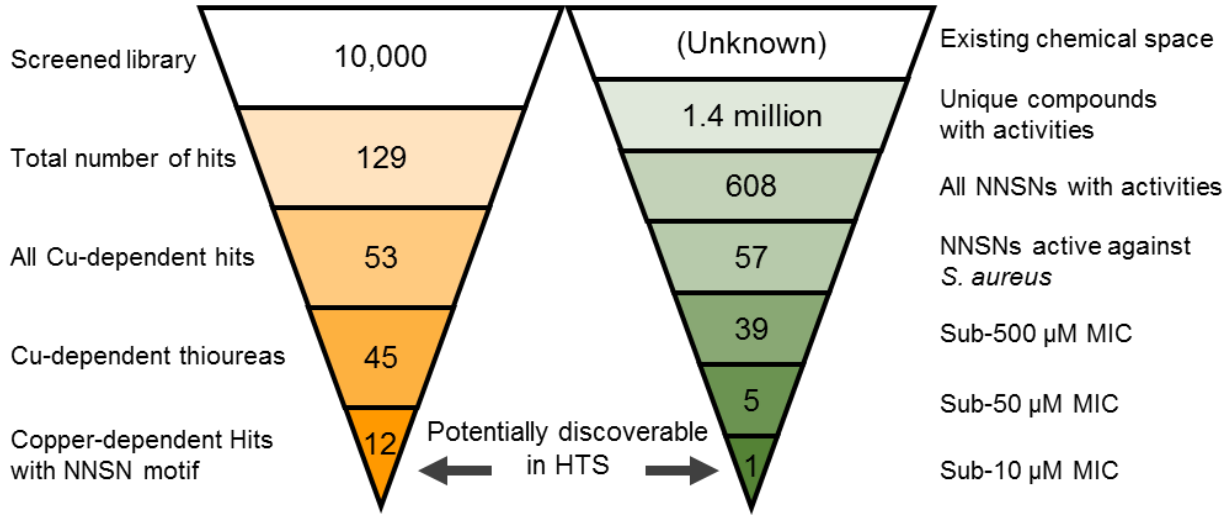

Figure 4.9: Chemoinformatic search of the ChEMBL database. The ChEMBL chemoinformatic database was queried with the NNSN motif for similar molecules. Though the limited screen described here revealed 12 NNSNs with significant antibacterial effects, only a single NNSN with activity against *S. aureus* below 10 μM was found within the database.

Querying the NNSN motif against the database returned 608 hits with recorded activity (Figure 4.9). Narrowing the search to only whole-cell activities against *S. aureus* returned only 57 hits. Most of these activities, however, were pulled from batch synthesis efforts reported in the literature, rather than from a directed screening campaign. Of the entire set, 39 had reported MICs below 500 mM, and only 5 had MICs below 50 mM; of these, only a single compound had a MIC below 10 mM.40 Given that HTS are limited to testing only one concentration, often at 10 mM, it is likely none of these compounds would have been found individually in a screening campaign, and, hence, would not have been identified as a hit series.

4.5. Discussion

In this study, we report the results of the first high throughput screening (HTS) campaign for the discovery of copper-dependent antibacterial inhibitors. This strategy not only resulted in a much greater number of promising hit molecules than traditional screening methods, but also specifically revealed a previously unknown hit series, whose anti-staphylococcal activity escaped previous detection despite being present in many screening libraries.

Though metal complexation screens could hypothetically proceed using any of the first row transition metals (Mn, Fe, Co, Ni, Cu, and Zn), copper offers the most attractive and most viable vehicle for synergistic inhibition. Copper's antimicrobial properties are multifaceted, but ultimately stem from its relative proclivity toward stable ligand complexation when compared to other transition metal ions. This phenomenon is described by the Irving–Williams series, where complex stabilities are their lowest with manganese, increase in periodic fashion until maximum stability at copper, and finally decline at zinc [41]. Functionally, this gives copper a higher affinity for sulfur, oxygen, and nitrogen than any other physiologically relevant transition metal [42]. This affinity, combined with copper's high redox potential, is often exploited in metallo-proteins such as superoxide dismutases or cytochrome c oxidases, and as such is key to the normal function of both prokaryotic and eukaryotic cells. However, copper ions in excess readily displace or replace crucial metalloenzyme cofactors, attack vulnerable iron–sulfur clusters, and directly damage accessible amino acid residues [15]. Cumulatively, these effects heavily interfere with cellular function; as a result, all sequenced bacteria possess at least some level of copper resistance [12].

As an antimicrobial, copper assaults numerous sites within the cell. Many bacteria have had specific targets identified (e.g., dehydratases in E. coli [43], aerobic nucleotide

synthesis in *Streptococcus pneumonia* [44], and heme biosynthesis in *Neisseria gonorrhoeae* [45], but outside of general mechanisms such as attacking iron–sulfur clusters in proteins, specific points of failure vary widely from organism to organism. The detected source of toxicity is simply the ‘‘weakest link,’’ or first component to fail. It is very likely some copper-dependent inhibitors feature a similar variety of mechanisms, especially if acting through general copper overload (as in the case of 8-hydroxyquinoline [20]. More targeted compounds may be capable of additional mechanisms as well. GTSM, for example, acts upon the electron transport chain of N. *gonorrhoeae*, with its spectrum of activity hypothesized to be explained through a particular bacterium’s reliance on aerobic respiration [17,25]. Yet, GTSM is also a potent copper-dependent inhibitor of *S. pneumoniae* (ref. 25; unpublished observations), a facultative anaerobe lacking an electron transport chain. Thus, additional modes of action must be at play, indicating a multi-faceted mechanism of activity. Though the ‘‘magic bullet’’ paradigm of one drug-one target has dominated since its proposal by Paul Ehrlich a century ago,46 copper-dependent inhibitors may offer an alternative: since multiple individual targets could be vulnerable, development of resistance would be much more difficult than against traditional, single target antibiotics.

The allure of copper’s anti-bacterial properties has not gone unnoticed [17–20,25,47–49]. Unfortunately, free copper ions have little therapeutic value due to their erratic reactivity [50–53]. To pharmacologically control the activity of copper ions and direct them to a specific target, numerous chemosynthetic efforts have synthesized copper complexes with greatly enhanced antibacterial activities [47,54–58]. However, many of these rely on metal binding motifs that had analytical and technical purposes, rather than medicinal applications. Subsequent synthesis

efforts often prioritize advancing the frontiers of organo-metallo-chemistry (e.g. mixed ligand complexes), leaving biological considerations as a secondary focus. Consequently, structure activity relationship studies, such as exemplified by the clinically used metalloantibiotic bacitracin [59], are extremely rare. While powerful in its own right, the agnosticism of this chemosynthetic strategy toward biological considerations impedes its applicability to HTS discovery. Though we have begun exploring how to harness the potential of copper in chelate based metalloantibiotics, we still need HTS solutions to probe the existing chemical space for novel metal-related activities to facilitate discovery and development of innovative metal-oriented therapeutics.

4.6. Conclusion

In summation, our work details the first concerted antibiotic HTS discovery effort to harness the activity of an unconventional antimicrobial, copper. These unique inhibitors have, until now, largely gone unnoticed within conventional screening libraries, offering a way to repurpose and reprobe existing chemical collections. Though therapeutically infeasible on its own, copper's potential can be readily exploited through combination with small organic molecules, offering a promising new approach in the battle for novel antibacterials.

References

1. K. Lewis, Nat. Rev. Drug Discovery, 2013, 12, 371–387.
2. T. W. House, http://www.whitehouse.gov/the-press-office/ 2014/09/18/executive-order-combating-antibiotic-resistantbacteria, 2014.
3. CDC, http://www.cdc.gov/drugresistance/pdf/ar-threats-2013-508.pdf, 2013.
4. M. A. Fischbach and C. T. Walsh, Science, 2009, 325,1089–1093.
5. J. Clardy, M. A. Fischbach and C. T. Walsh, Nat. Biotechnol., 2006, 24, 1541–1550.
6. A. L. Demain, Nat. Biotechnol., 2002, 20, 331.
7. M. I. Hood and E. P. Skaar, Nat. Rev. Microbiol., 2012, 10, 525–537.
8. Y. Fu, F. M. Chang and D. P. Giedroc, Acc. Chem. Res., 2014, 47, 3605–3613.
9. V. Hodgkinson and M. J. Petris, J. Biol. Chem., 2012, 287, 13549–13555.
10. C. White, T. Kambe, Y. G. Fulcher, S. W. Sachdev, A. I. Bush, K. Fritsche, J. Lee, T. P. Quinn and M. J. Petris, J. Cell Sci., 2009, 122, 1315–1321.
11. M. D. Johnson, T. E. Kehl-Fie, R. Klein, J. Kelly, C. Burnham, B. Mann and J. W. Rosch, Infect. Immun., 2015, 83,1684–1694.
12. M. Solioz, H. K. Abicht, M. Mermod and S. Mancini, JBIC, J. Biol. Inorg. Chem., 2010, 15, 3–14.
13. K. Y. Djoko, J. A. Franiek, J. L. Edwards, M. L. Falsetta, S. P. Kidd, A. J. Potter, N. H. Chen, M. A. Apicella, M. P. Jennings and A. G. McEwan, Infect. Immun., 2012, 80, 1065–1071.
14. X. Shi and K. H. Darwin, Metallomics, 2015, 7, 929–934.
15. A. W. Foster, D. Osman and N. J. Robinson, J. Biol. Chem., 2014, 289, 28095–28103.

16. T. D. Rae, P. J. Schmidt, R. A. Pufahl, V. C. Culotta and T. V. O'Halloran, Science, 1999, 284, 805–808.
17. K. Y. Djoko, B. M. Paterson, P. S. Donnelly and A. G. McEwan, Metallomics, 2014, 6, 854–863.
18. M. Haeili, C. Moore, C. J. C. Davis, J. B. Cochran, S. Shah,T. B. Shrestha, Y. Zhang, S. H. Bossmann, W. H. Benjamin, O. Kutsch and F. Wolschendorf, Antimicrob. Agents Chemother., 2014, 58, 3727–3736.
19. A. G. Dalecki, M. Haeili, S. Shah, A. Speer, M. Niederweis, O. Kutsch and F. Wolschendorf, Antimicrob. Agents Chemother., 2015, 59, 4835–4844.
20. R. A. Festa, M. E. Helsel, K. J. Franz and D. J. Thiele, Chem. Biol., 2014, 21, 977–987.
21. S. M. Hadi, M. F. Ullah, A. S. Azmi, A. Ahmad, U. Shamim, H. Zubair and H. Y. Khan, Pharm. Res., 2010, 27, 979–988.
22. S. M. Schmitt, M. Frezza and Q. P. Dou, Front. Biosci., 2012, 4, 375–391.
23. M. A. Cater, H. B. Pearson, K. Wolyniec, P. Klaver, M. Bilandzic, B.M. Paterson, A. I. Bush, P.O.Humbert, S. La Fontaine, P. S. Donnelly and Y. Haupt, ACS Chem. Biol., 2013, 8, 1621–1631.
24. O. Neyrolles, F. Wolschendorf, A. Mitra and M. Niederweis, Immunol. Rev., 2015, 264, 249–263.
25. K. Y. Djoko, M. M. Goytia, P. S. Donnelly, M. A. Schembri, W.M. Shafer and A. G. McEwan, Antimicrob. Agents Chemother., 2015, 59, 6444–6453.
26. N. M. O'Boyle, M. Banck, C. A. James, C. Morley, T. Vandermeersch and G. R. Hutchison, J. Cheminf., 2011, 3, 33.

27. A. Speer, T. B. Shrestha, S. H. Bossmann, R. J. Basaraba, G. J. Harber, S. M. Michalek, M. Niederweis, O. Kutsch and F. Wolschendorf, Antimicrob. Agents Chemother., 2013, 57, 1089–1091.

28. T. Lech and J. K. Sadlik, Biol. Trace Elem. Res., 2007, 118, 16–20.

29. H. A. Benesi and J. H. Hildebrand, J. Am. Chem. Soc., 1949, 71, 2703–2707.

30. A. P. Bento, A. Gaulton, A. Hersey, L. J. Bellis, J. Chambers, M. Davies, F. A. Kru¨ger, Y. Light, L. Mak, S. McGlinchey, M. Nowotka, G. Papadatos, R. Santos and J. P. Overington, Nucleic Acids Res., 2014, 42, D1083–1090.

31. M. Davies, M. Nowotka, G. Papadatos, F. Atkinson, G. van Westen, N. Dedman, R. Ochoa and J. Overington, Challenges, 2014, 5, 334.

32. J. P. Lisher and D. P. Giedroc, Front. Cell. Infect. Microbiol., 2013, 3, 91.

33. O. M. Goudouri, E. Kontonasaki, U. Lohbauer and A. R. Boccaccini, Acta Biomater., 2014, 10, 3795–3810.

34. C. A. Lipinski, Drug Discovery Today: Technol., 2004, 1, 337–341.

35. T. H. Keller, A. Pichota and Z. Yin, Curr. Opin. Chem. Biol., 2006, 10, 357–361.

36. J. Liu, D. Obando, V. Liao, T. Lifa and R. Codd, Eur. J. Med.Chem., 2011, 46, 1949–1963.

37. G. F. Smith, in Progress in Medicinal Chemistry, ed.G. Lawton and D. R. Witty, Elsevier, 2011, vol. 50, pp. 1–47.

38. H. J. Petersen, C. K. Nielsen and E. Arrigoni-Martelli, J. Med.Chem., 1978, 21, 773–781.

39. M. Ho¨gberg, P. Engelhardt, L. Vrang and H. Zhang, Bioorg.Med. Chem. Lett., 2000, 10, 265–268.

40. G. S. Hassan, S. M. El-Messery, F. A. M. Al-Omary, S. T. Al-Rashood, M. I. Shabayek, Y. S. Abulfadl, E.-S. E. Habib, S. M. El-Hallouty, W. Fayad, K. M. Mohamed, B. S. El-Menshawi and H. I. El-Subbagh, Eur. J. Med. Chem., 2013, 66, 135–145.
41. H. Irving and R. J. P. Williams, J. Chem. Soc., 1953, 3192–3210, DOI: 10.1039/JR9530003192.
42. D. Nies, in Molecular Microbiology of Heavy Metals,ed. D. Nies and S. Silver, Springer Berlin Heidelberg, 2007, ch. 75, vol. 6, pp. 117–142.
43. L. Macomber and J. A. Imlay, Proc. Natl. Acad. Sci. U. S. A.,2009, 106, 8344–8349.
44. M. D. Johnson, T. E. Kehl-Fie and J. W. Rosch, Metallomics,2015, 7, 786–794.
45. K. Y. Djoko and A. G. McEwan, ACS Chem. Biol., 2013, 8,2217–2223.
46. K. Strebhardt and A. Ullrich, Nat. Rev. Cancer, 2008, 8,473–480.
47. K. Y. Djoko, M. M. Goytia, P. S. Donnelly, M. A. Schembri,W.M. Shafer and A. G. McEwan, Antimicrob. Agents Chemother.,2015, 59, 6444–6453.
48. G. Grass, C. Rensing and M. Solioz, Appl. Environ. Microbiol.,2011, 77, 1541–1547.
49. X. Liu, X. Li, Z. Zhang, Y. Dong, P. Liu and C. Zhang, Biol.Trace Elem. Res., 2013, 154, 150–155.
50. G. J. Cooper, Drugs, 2011, 71, 1281–1320.
51. L. Macomber, C. Rensing and J. A. Imlay, J. Bacteriol., 2007,189, 1616–1626.
52. C. Rensing and G. Grass, FEMS Microbiol. Rev., 2003, 27,197–213.
53. P. Szymanski, T. Fraczek, M. Markowicz and E. Mikiciuk-Olasik, BioMetals, 2012, 25, 1089–1112.
54. M. L. Beeton, J. R. Aldrich-Wright and A. Bolhuis, J. Inorg.Biochem., 2014, 140, 167–172.

55. B. Bottari, R. Maccari, F. Monforte, R. Ottana, E. Rotondo and M. G. Vigorita, Bioorg. Med. Chem. Lett., 2000, 10, 657–660.

56. Z. H. Chohan, M. Arif, Z. Shafiq, M. Yaqub and C. T. Supuran, J. Enzyme Inhib. Med. Chem., 2006, 21, 95–103.

57. Z. H. Chohan, H. Pervez, A. Rauf, A. Scozzafava and C. T. Supuran, J. Enzyme Inhib. Med. Chem., 2002, 17, 117–122.

58. H. Gershon, R. Parmegianir and W. J. Nickerson, Appl. Microbiol., 1962, 10, 556–560.

59. L. J. Ming and J. D. Epperson, J. Inorg. Biochem., 2002, 91,46–58.

Appendix A - Spectral Analysis (Chapter 2)

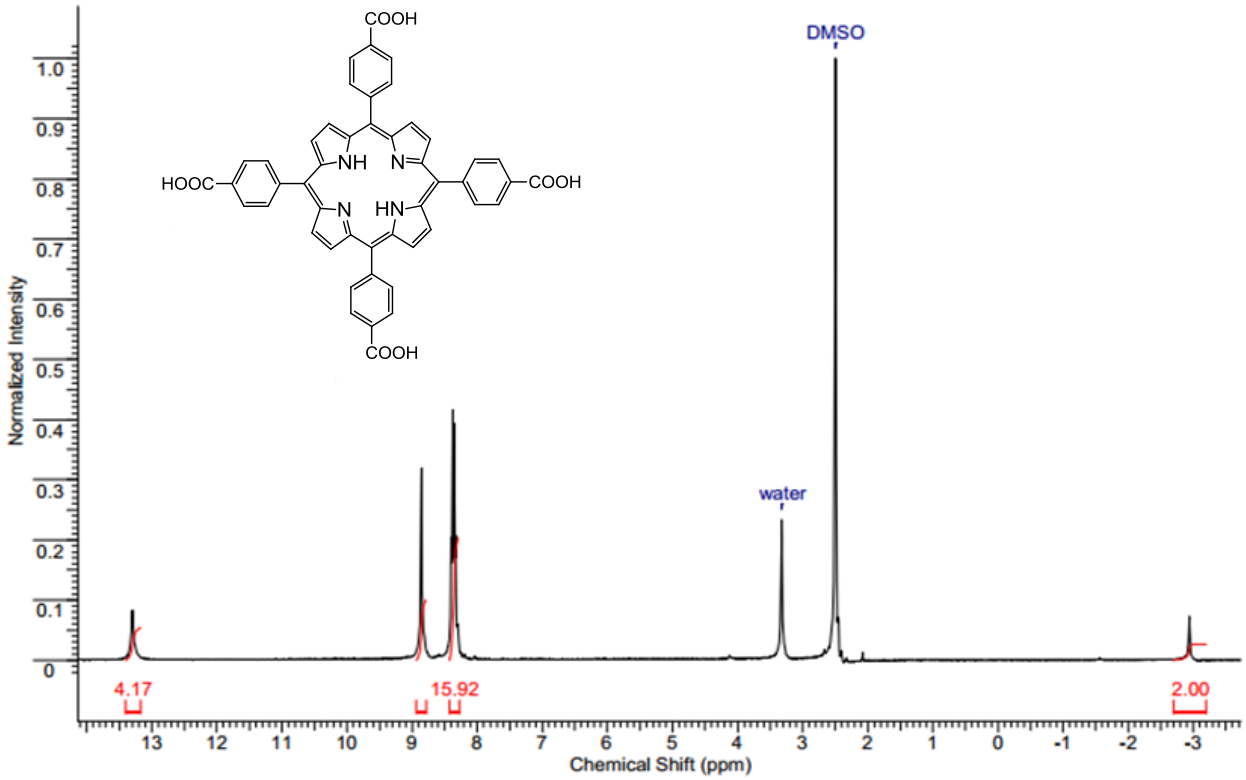

Figure A1: 1H-NMR of (4-carboxyphenyl)porphyrin (TCPP) (Varian, 400 MHz).

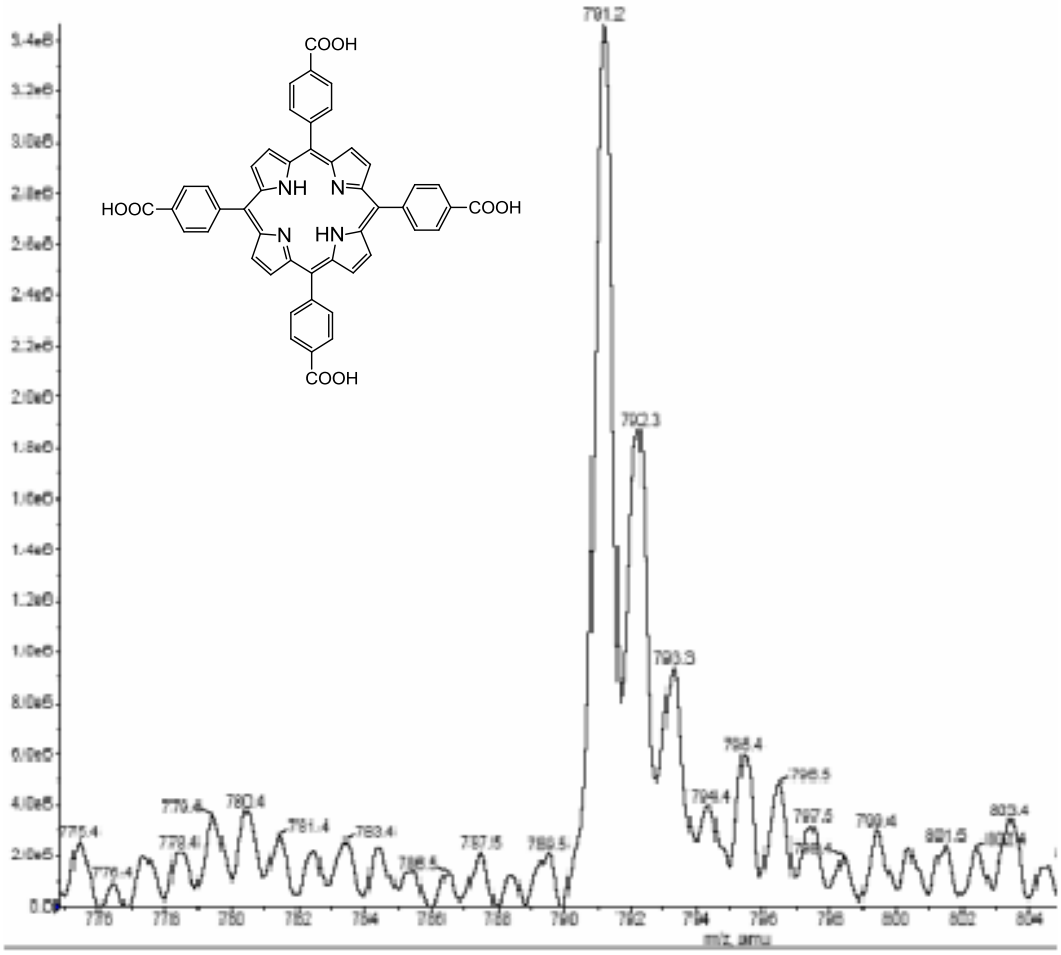

Figure A2: Mass spectrum of (4-carboxyphenyl)porphyrin (TCPP)

$C_{48}H_{30}N_4O_8$

Exact Mass: 790.21

m/e: $(M+H)^+$791.21

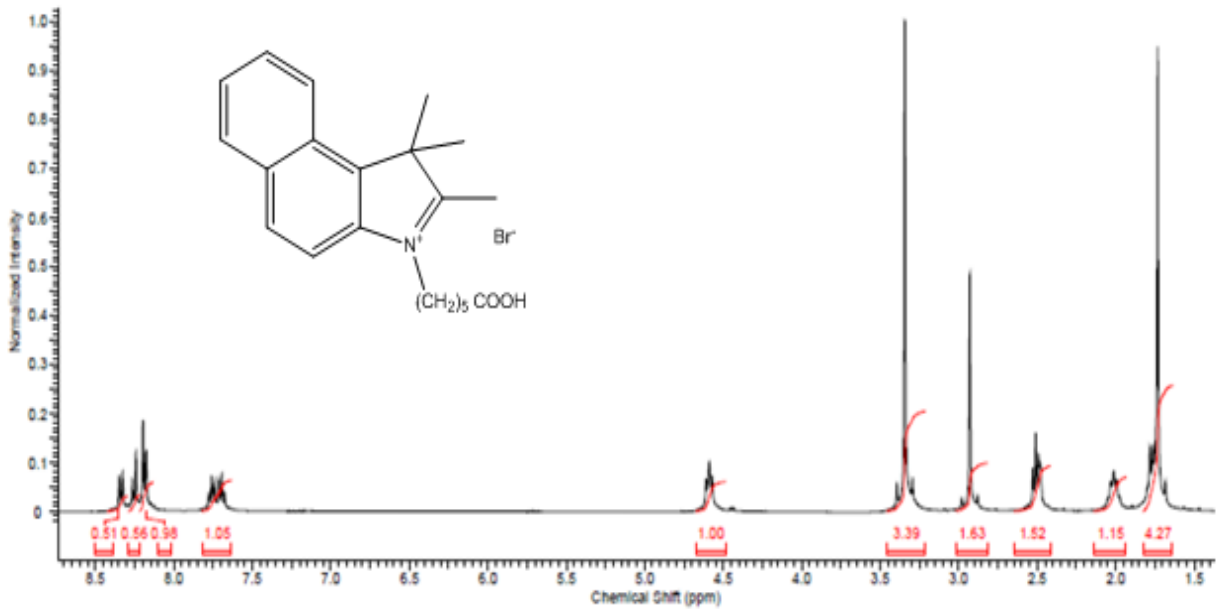

Figure A3: 1H-NMR of 3-(5-carboxypentyl)-1,1,2-trimethyl-1H-benzo[e]indol-3-ium (Varian, 400 MHz).

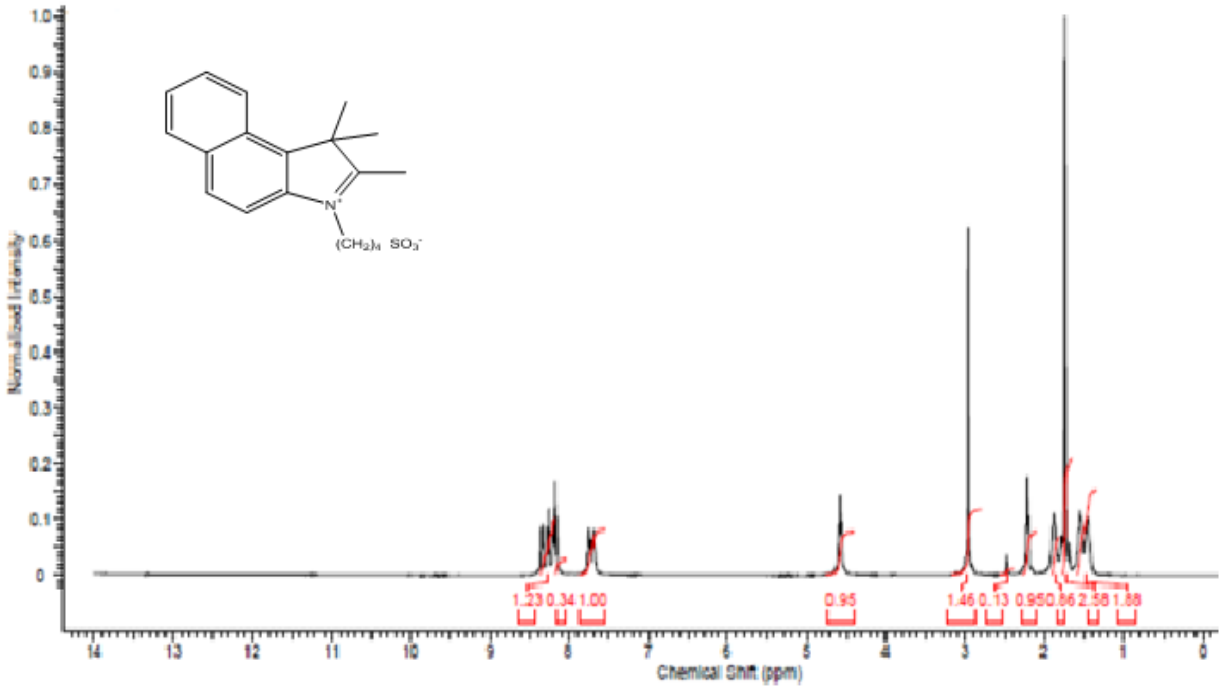

Figure A4: 1H-NMR of 4-(1,1,2-trimethyl-1H-benzo[e]indol-3-ium-3-yl)butane-1-sulfonate (Varian, 400 MHz).

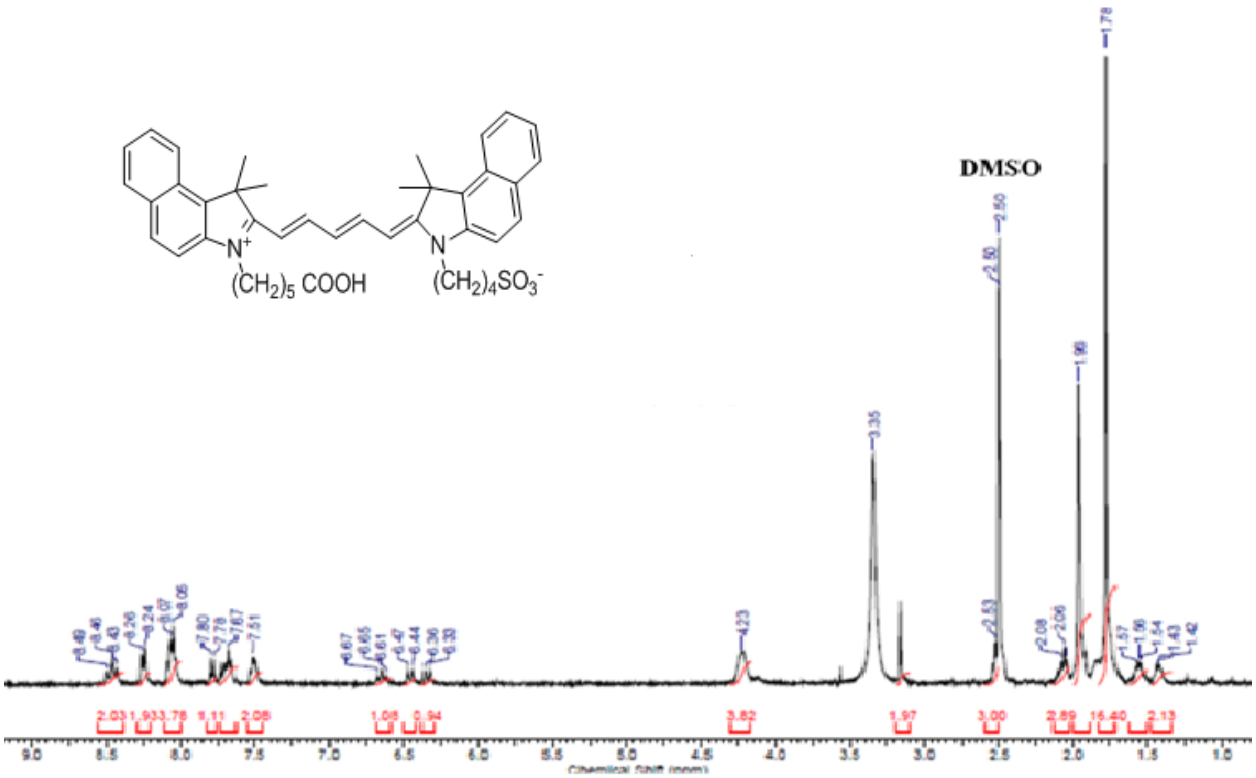

Figure A5: 1H-NMR of Cyanine 5.5(Varian, 400 MHz).

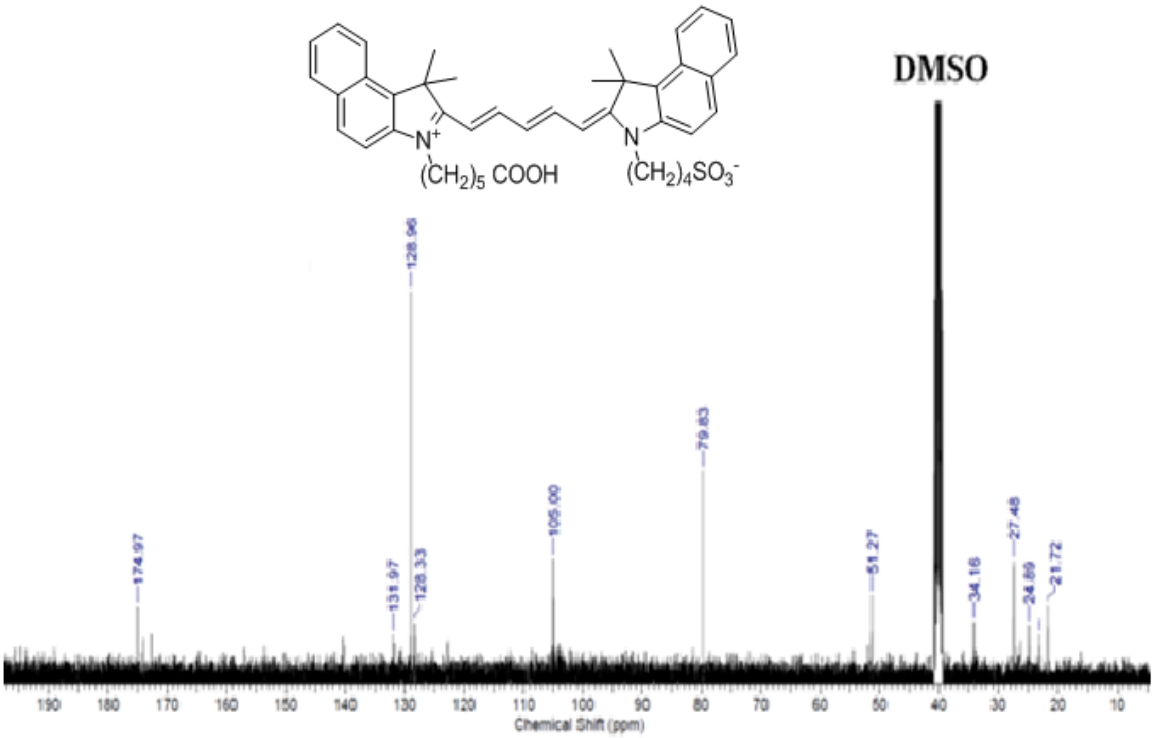

Figure A6: ^{13}C-NMR of Cyanine 5.5(Varian, 400 MHz).

Appendix B - Mass spectral Predictions (Chapter 4)

Calculated molar peaks for $C_{21}H_{25}ClN_4S$		Found (M-1) peaks for $C_{21}H_{24}ClN_4S$	
400.148845223	100.0	399.14027	100.0
401.151814098	25.247685799	400.11207	32.443
402.14644539	39.482274778	401.12801	43.180
403.148865348	9.42133780043	402.09933	13.601
404.145929417	2.58031685727	403.07903	4.7281
405.146631923	0.443145002843		

(1)

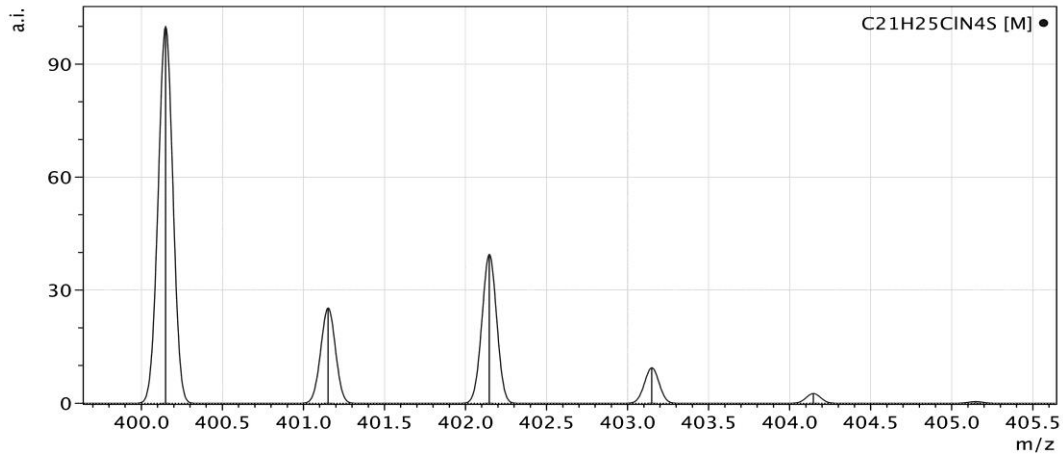

(2)

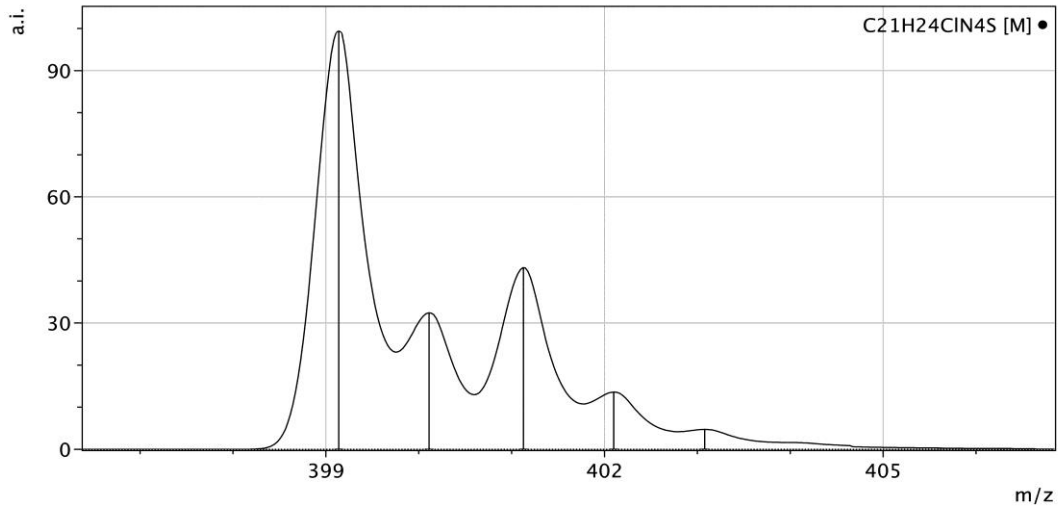

Figure B (1) (2): Mass spectrum of $C_{21}H_{25}ClN_4S$

(3)

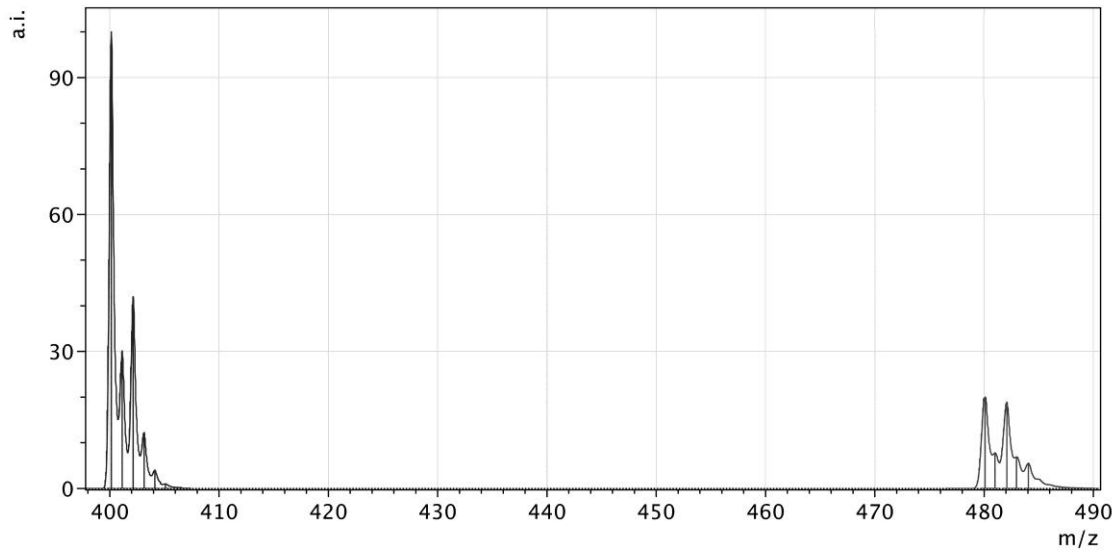

(4)

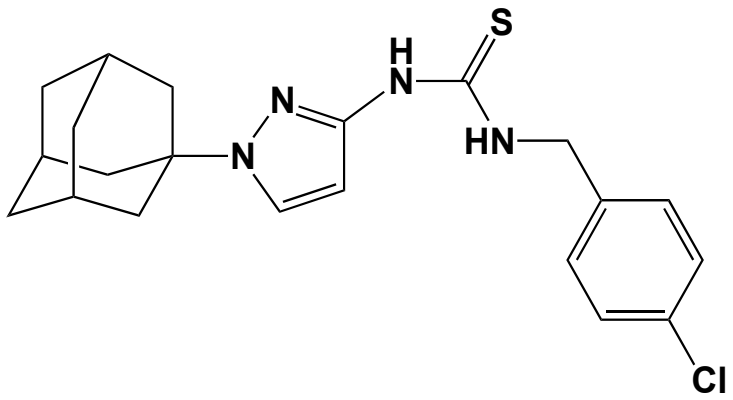

Figure B:

(3) Mass spectrum of $C_{21}H_{25}ClN_4S$ and Cu(I) complex formed at micromolar concentration range: (1:1 ratio)

(4) The structure consistent with the complex formed at micromolar concentration range: (1:1 ratio)

Calculated peaks for $C_{21}H_{26}N_4OClS$

480.079084384	100.0
480.998798585	37.0905660322
482.071687129	90.1116654203
482.968631521	32.9262775276
484.043056234	26.3941213765

Found peaks for $C_{21}H_{26}N_4OClS$

480.07907	21.201
480.99879	7.790
482.07171	18.922
482.96862	6.916
484.04306	5.542

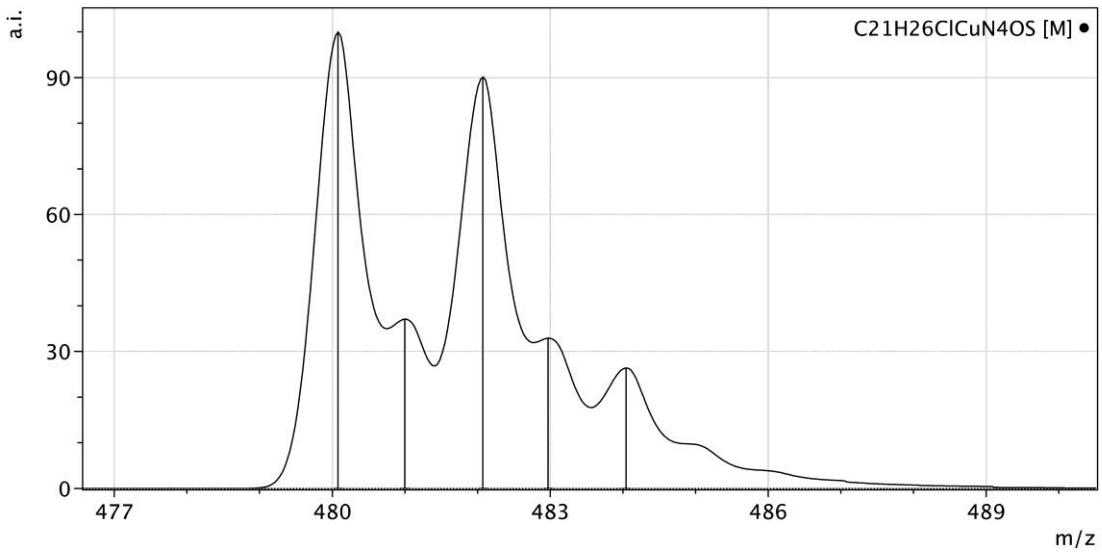

Figure B5: Mass spectrum of $C_{21}H_{26}ClCuN_4OS$

Calculated peaks for $C_{42}H_{50}Cl_2CuN_8S_2$		Found peaks for $C_{42}H_{50}Cl_2CuN_8S_2$	
831.258680937	6.69308335001	831.25868	6.691
832.222866887	4.37557054894	832.22293	4.380
833.241333065	9.10552480002	833.24133	9.106
834.180127148	5.39869010354	834.18021	5.399
835.209772629	4.86998701706	835.20980	4.868
836.118434462	2.57582364786	836.11844	2.577
837.101586016	1.40926624196	837.10156	1.410

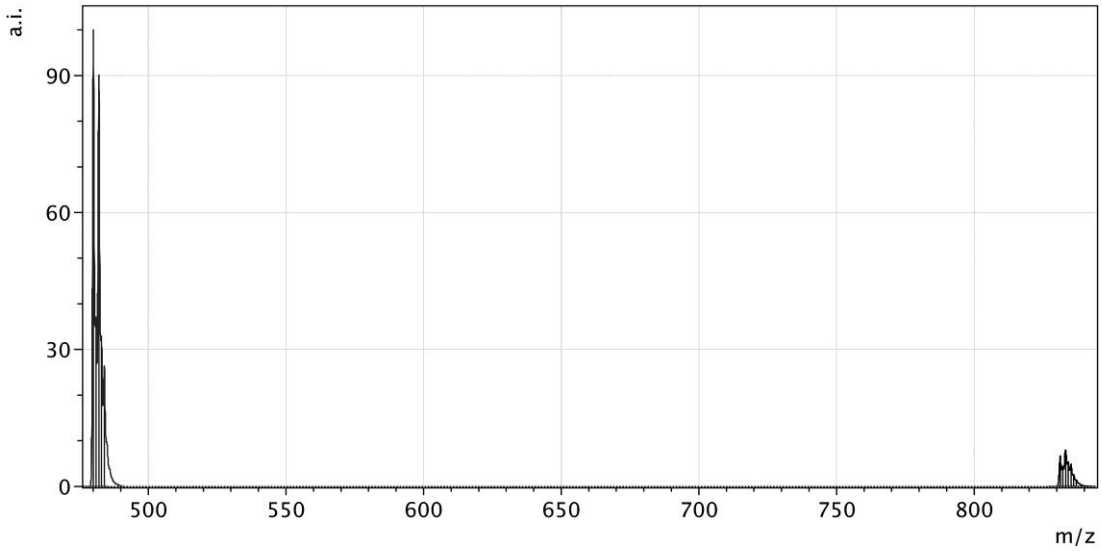

Figure B6: Mass spectrum of $C_{42}H_{50}Cl_2CuN_8S_2$ complex

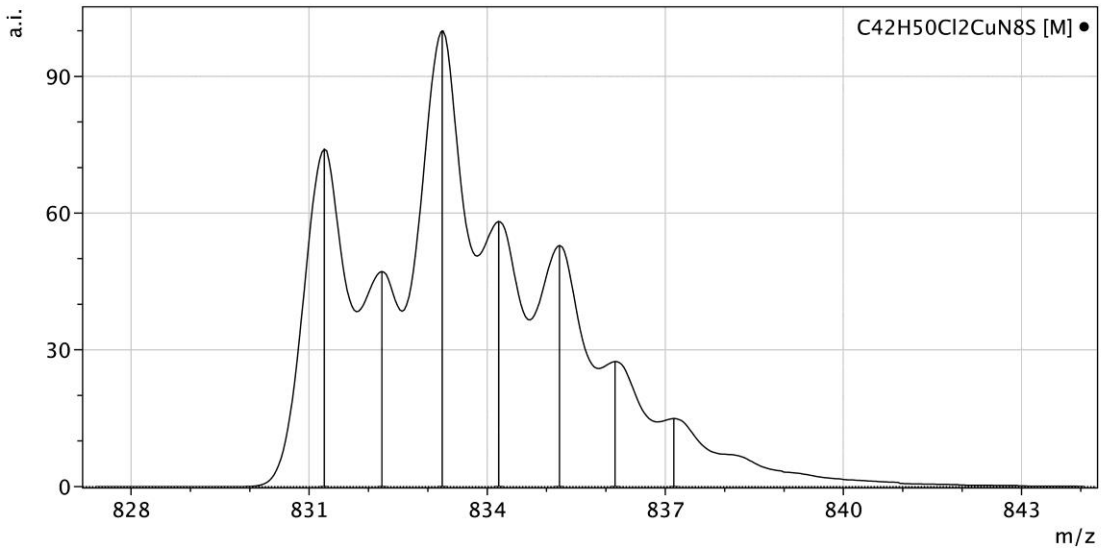

Figure B7: Mass spectrum of $C_{42}H_{50}Cl_2CuN_8S_2$ complex

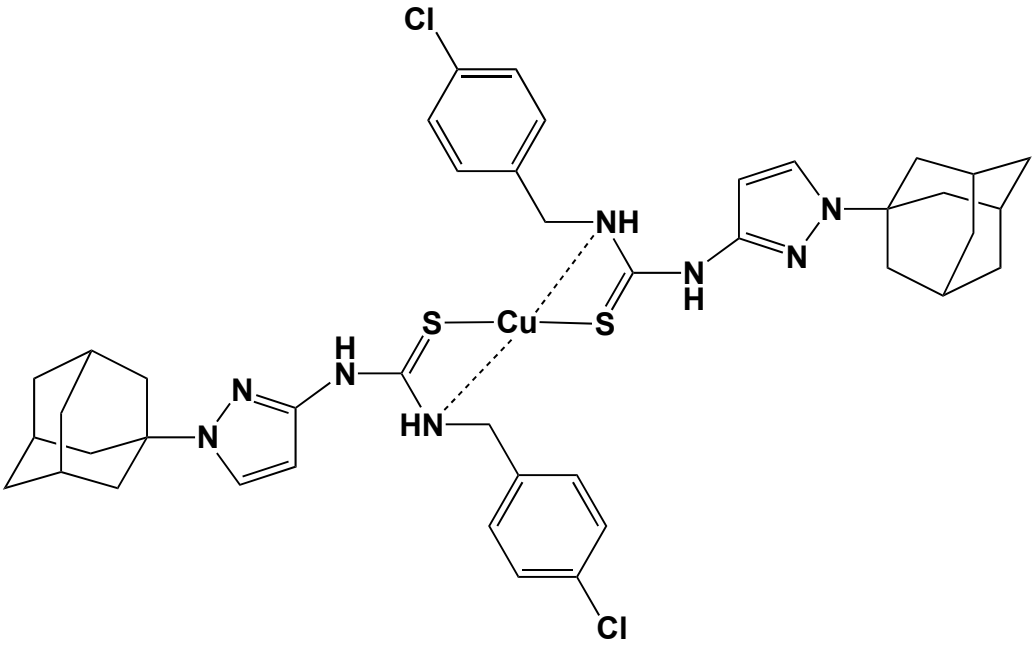

Figure B8: Complex structure of $C_{42}H_{50}Cl_2CuN_8S_2$ consistent with the mass spectrum

Calculated peaks for $C_{24}H_{32}N_4S$		Found peaks for $C_{24}H_{32}N_4S$	
408.234767738	100.0	409.24199	100.0 0
409.237808811	28.5708719491	410.23315	33.255
410.235157672	8.46243683171	411.22534	11.015
411.235562523	1.60335922847	412.20772	2.898
412.236657927	0.206573945737	413.11461	0.863

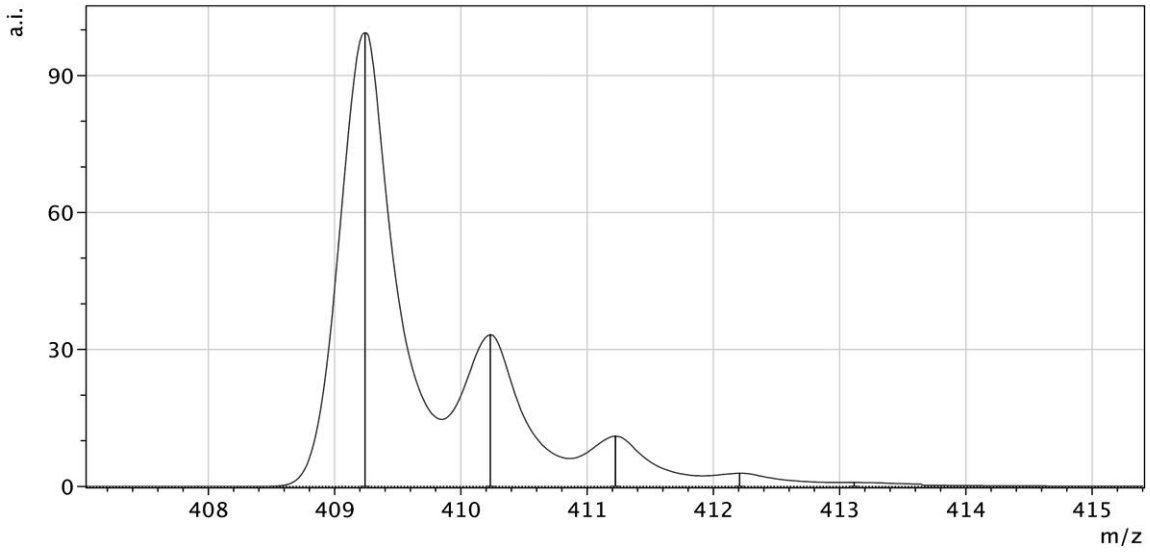

Figure B9: Mass spectrum of $C_{24}H_{32}N_4S$

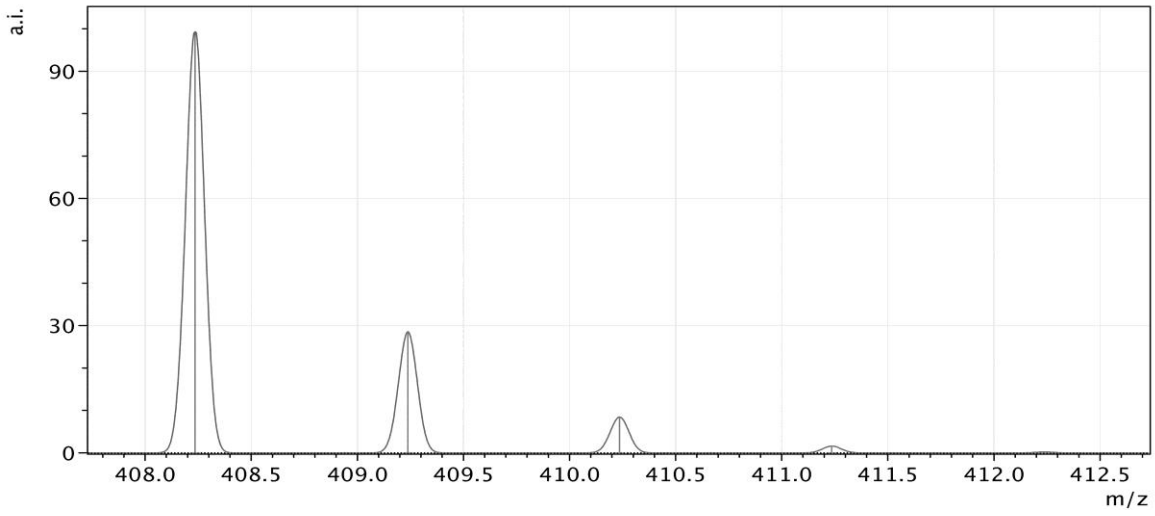

Figure B10: Mass spectrum of $C_{24}H_{32}N_4S$

Peaks found for $C_{24}H_{34}CuN_4OS$ complex formed at micromolar range

489.17425	7.155
490.12755	2.745
491.16090	4.1840
492.10877	1.5401
493.06142	0.5680

Peaks calculated for $C_{24}H_{34}CuN_4OS$ complex formed at micromolar range

489.174254513	100.0
490.127536823	38.3361417666
491.160909315	58.4683003114
492.108754866	21.5264145111
493.061392146	7.93871550432

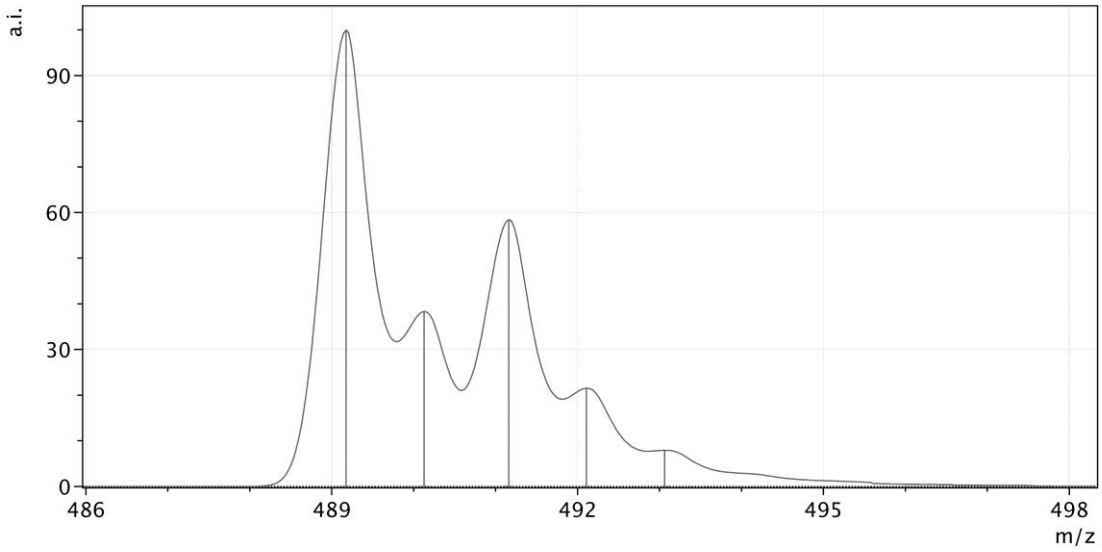

Figure B11: Mass spectrum of $C_{24}H_{34}CuN_4OS$ complex formed at micromolar range

Peaks calculated for $C_{24}H_{34}CuN_4OS$ complex formed at millimolar range:

879.428774413 100.0

880.345468124 78.881

881.351093445 86.012

Peaks found for $C_{24}H_{34}CuN_4OS$ complex formed at millimolar range:

879.42878 100.0

880.34551 78.6593452815

881.35110 85.9995952992

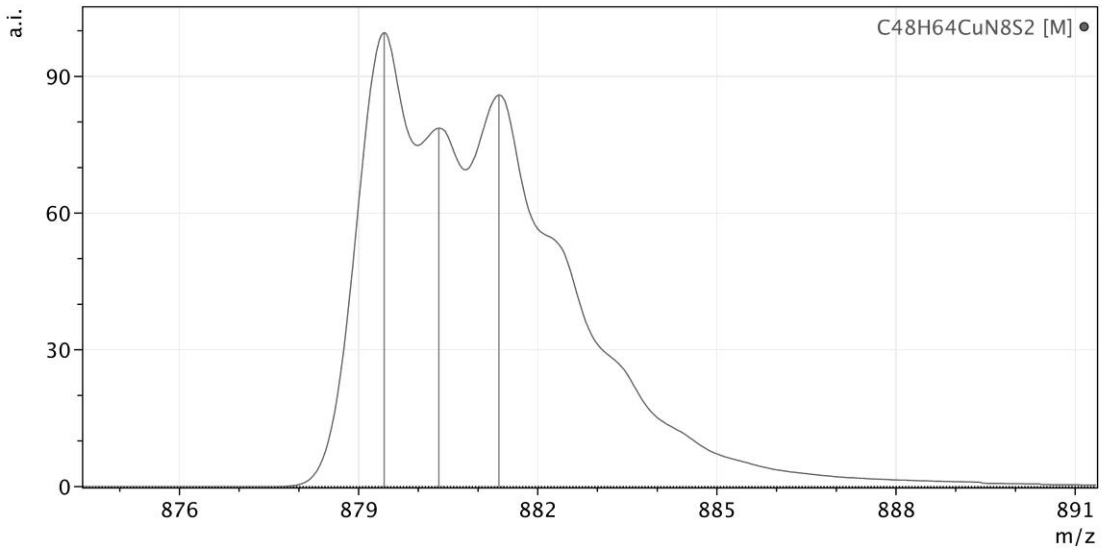

Figure B12: Mass spectrum of $C_{24}H_{34}CuN_4OS$ complex formed at millimolar range